Femtosecond laser ablation of metals

Gearoid O'Connell

A thesis presented for the degree of
Doctor of Philosophy

School of Physics
Trinity College Dublin
Ireland

March 2015

Declaration

I declare that this dissertation is entirely my own work, carried out at the Trinity College Dublin, and has not been submitted for a degree to this or any other University and that the contents are original unless otherwise stated.

I agree to allow the library of Trinity College Dublin to copy or lend a section or this entire thesis on request.

Signed,

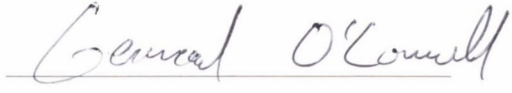

Gearoid O'Connell

Summary

Femtosecond laser ablation of metals and dielectrics is currently very topical due to its new and distinctive ablation process and the growing number of applications. The ablation process is rather complex and results in the formation of two distinct plumes, a fast, atomic component, and a slow component comprised mainly of nanoparticles. This thesis describes the results of an investigation into the femtosecond laser ablation of some metals. The experiments were performed for gold, silver, aluminium and tin to compare the differences in their ablation behaviour.

We studied the atomic plume spectral and spatial emission and found that it is a low temperature plasma with a supersonic velocity. To characterise the nanoparticle plume we performed *in situ*, time-dependent optical emission and absorption measurements. We aimed to extend current analysis methods by taking into account the wavelength dependence of the nanoparticle optical properties. From our results, we inferred the temperature and the amount of material in the nanoparticle plume. We found the nanoparticle plume temperatures varied from about 1700-3000 K depending on material and the time the measurement was taken with respect to the laser pulse. In this range, the nanoparticles were found to cool primarily by evaporation. From our study we noticed significant differences in the plume characteristics of each material. Finally, we studied the behaviour of each plume component in a background gas environment of argon and helium up to atmospheric pressure.

Keywords: Femtosecond laser ablation, optical emission spectroscopy, plume confinement in background gas, Langmuir ion probe, gold, silver, aluminium, tin.

Acknowledgements

I would like to express my gratitude to Prof. James Lunney for giving me this opportunity and for his support and advise throughout the project.

I would like to thank my parents for their support throughout my career and belief that I would eventually finish college. I am also grateful for the support my siblings, Eamonn, Eilis and Ian.

I would like to thank all current and past group members including Isaac, Inam, Clelia, Enrique and James. Most notable of which, Tony Donnelly who has been extremely helpful since my undergraduate final year project.

The staff of the school of physics deserve particular mention. To Nigel, Chris, Jing Jing, Dave, and Pat; thanks for the help in (and outside) the lab.

I also would like to thank David McCloskey for always being available for helpful discussions, usually over a coffee or a pint.

I would like to thank Science Foundation Ireland for funding this project.

Contents

Declaration iii

Summary v

Acknowledgements vii

1 Introduction 1

1.1 Objectives 4

2 Theory 7

2.1 Femtosecond laser ablation 8

2.1.1 Laser absorption 8

2.1.2 Ablation mechanisms 10

2.1.3 Ablation in the thermal regime 13

2.2 Plume expansion 15

2.3 Optical emission spectroscopy 19

2.3.1 PrismSPECT 23

2.4 Interaction of light with small metallic particles 24

2.5 Nanoparticle cooling mechanisms 27

3 Experimental methods 33

3.1 Experiment setup 33

3.1.1 Laser systems 34

3.2 Spectrometer calibration 36

3.3 Langmuir probe 41

3.4 Nanoparticle optical absorption 44
3.5 Film thickness estimation 48
3.6 White light interferometry 50

4 Femtosecond laser ablation and deposition 53

4.1 Crater analysis 56
4.2 STEM depositions 58
4.3 Angular distribution of deposition 60
4.4 Conclusions 61

5 Femtosecond atomic plume 63

5.1 Langmuir ion probe 64
5.2 ICCD imaging 69
5.3 Spectroscopy 74
5.3.1 Gold 75
5.3.2 Silver 77
5.3.3 Aluminium 86
5.4 Conclusions 87

6 Nanoparticle plume dynamics 89

6.1 ICCD imaging 90
6.2 Nanoparticle plume spectroscopy 92
6.3 Single wavelength absorption 99
6.4 Other materials 103
6.5 Conclusions 107

7 Femtosecond ablation plume dynamics in background gas 109

7.1 Conclusions 123

8 Conclusions and future work **125**

8.1 Conclusions 125

8.1.1 Future work 126

A Appendix **129**

A.1 Early stage optical emission in nanosecond laser ablation 129

A.1.1 Conclusions 135

A.2 Material optical properties 136

A.3 Computational model of atomic plume expansion in femtosecond laser ablation 138

Chapter 1

Introduction

Since the invention of the ruby laser in 1960, there has been extensive investigations of the interaction of laser radiation with all forms of matter [1]. Initially, the laser was described as "a solution looking for a problem". Today, lasers are everywhere, from optical fibers, transmitting signals at much higher transfer rates than metallic cables, to the scanner in a supermarket checkout. The main advantages of lasers are its narrow spectral line width, long temporal coherence and high intensity.

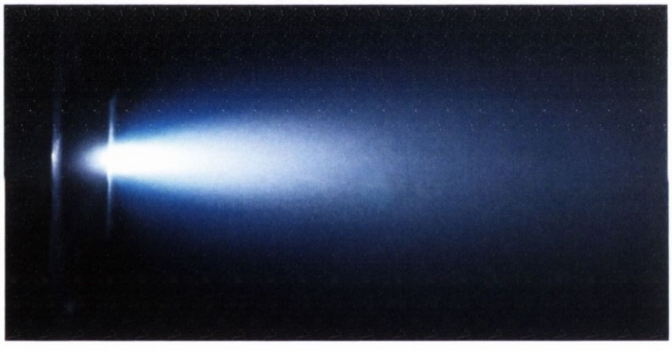

Figure 1.1: Time integrated image of a zinc plasma plume produced by a 1064 nm Nd:YAG nanosecond laser with an average fluence of $4\,\mathrm{J\,cm^{-2}}$.

Intense laser irradiation of materials has been an active area of study since 1962 when Breech and Cross published their study on the vaporisation and excitation of the surface of a solid target by laser irradiation [2]. A laser can be continuous wave (CW) or pulsed. Pulsed operation of lasers result in a much higher achievable peak power since the energy stored in the laser gain medium is released in a short pulse. Laser ablation is the removal of material from a surface by laser beam irradiation, typically carried out by a pulsed laser. Pulsed laser ablation has numerous advantages, for example; a smaller heat effected region and a higher ablation efficiency than with CW ablation. This is due to fact that the energy absorbed by the target does not have time to conduct away from the laser irradiated region and therefore, more of the energy contributes to the material removal process.

Pulsed laser ablation has many applications in material science including thin film deposition, nanoparticle production, material identification, novel light sources .etc. It also has applications in a number of other fields such as laser based surgery and in industrial engineering for precision machining or patterning [3]. Laser-matter interaction involves a number of complex processes; heating, melting, vaporization, ionization, plasma formation and expansion. Figure 1.1 shows the light emission from a typical plasma plume generated with an 8 ns, 1064 nm Nd:YAG irradiating a solid zinc target with a fluence of $4\,\mathrm{J\,cm^{-2}}$ and recorded with a time integrating RGB camera. The laser-matter interaction leads to vaporisation of a small amount of material from the target surface. The vapour is hot, $\approx 1\,\mathrm{eV}$, in this case is nearly fully ionized and emits intense optical radiation. The ablated material, initially present as a hot layer on the target surface, undergoes a 3-dimensional expansion. These are the main features of laser ablation and will be discussed in more detail throughout this thesis.

Laser absorption occurs in a thin layer of target material at the surface, described by the optical absorption coefficient, α

$$\alpha = \frac{4\pi k}{\lambda} \tag{1.1}$$

where k is the extinction coefficient of the target material and λ is the laser wavelength. The optical absorption depth, $d = \alpha^{-1}$, is on the order of tens of nanometers for most metals. Laser wavelength plays an important role in the choice of irradiating laser, fig. 1.2 shows the variation of optical absorption depth for gold. At lower wavelengths, there is a much shorter absorption depth, resulting in most of the laser energy delivered within the first few nm of the material. This is an ideal choice for laser patterning and precise micro-machining. In fig. 1.2, we observe two peaks in absorption depth at 330 and 470 nm which are due to interband transitions in gold [4, 5].

Recent developments have lead to the availability of commercial, high peak power, ultra short pulsed lasers, i.e. lasers that have a pulse length of less then a few picoseconds, but with a large enough pulse energy to achieve ablation. For femtosecond ablation of metals, a fluence of $\approx 0.1\,\mathrm{J\,cm^{-2}}$ is required to achieve ablation, whereas for nanosecond ablation, the threshold is $\approx 0.6\,\mathrm{J\,cm^{-2}}$. For femtosecond ablation, the energy is delivered in a much shorter time scale than for nanosecond laser ablation which results in a much smaller heat-affected zone. This is advantageous for material processing, the ablation process is more efficient and it reduces the melting and re-solidification of the remaining material which could be detrimental to thermally sensitive devices. Ultra-short pulse

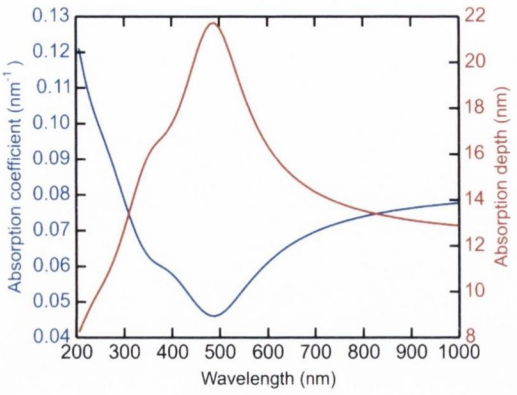

Figure 1.2: Calculated optical absorption coefficient and corresponding absorption depth for bulk gold.

laser ablation has been an active area of research for several decades. However, the interaction between metals and ultra short laser pulses is still not fully understood. The main objective of this research is to further the understanding of femtosecond laser ablation of metals.

As is described in more detail in chapter 2, the laser pulse length strongly influences the ablation plume formation mechanisms. For femtosecond ablation, two plume components are formed, a fast atomic/ionic plume and a slower nanoparticle plume. The nanoparticles are formed within the target before it unloads to form a nanoparticle plume which can then be deposited on a substrate to form a nanostructured film. Nanosecond ablation proceeds by thermal evaporation of the material from the target which normally consists of a single plasma plume. The plasma can be deposited on a substrate to form uniform or nanostructured thin films. With each successive laser pulse the nanoparticles increase in size, eventually coalesce and begin to form a continuous thin film. Recently there has been a significant number of papers published in the area of femtosecond laser ablation of metals and other materials [6–9]. However, there are some aspects still not well characterised. The partition of material between the atomic and nanoparticle plumes is currently not well understood. This work aims to address this issue by studying laser ablated material by using multiple diagnostic mechanisms to study multiple metals. Gold and silver were chosen as their nanoparticles are of interest for a number of applications such as surface enhanced Raman spectroscopy [10, 11]. Tin was chosen as it is currently of interest as an extreme ultraviolet source for lithographic applications [12]. Aluminium was chosen due to its low atomic weight in contrast to the other, relatively heavy materials. The analysis of the nanoparticle plume is of particular interest in this work. By taking into account the wavelength dependent emissivity we have improved current methods to estimate the plume temperature and to perform an *insitu*

measurement of the amount of material in the plume [8].

It is also possible to slow and confine the plume using a background gas to cause nanoparticle formation during the plume expansion and before reaching a substrate. In this thesis we will aim to experimentally study the femtosecond laser ablation process for different metals by comparing a number of characterisation techniques to build up a comprehensive description of the process.

1.1 Objectives

This work can be divided into two main parts:

1. The study of the femtosecond plume expansion in vacuum. To develop new techniques and to expand existing analysis methods and techniques to further the understanding of the ablation process.

2. To utilise these techniques to further study the influence of background gas on plume propagation for femtosecond ablation of different metals.

Chapter 2 describes the theory relevant to the ablation process. Femtosecond and nanosecond ablation regimes will be described. Also discussed in this chapter is the fundamentals of optical emission spectroscopy from a plasma. To characterise the nanoparticle plume, we will also discuss the nanoparticle optical properties and how this influences their emission, absorption and cooling rates.

Chapter 3 describes in detail the laser systems and main experimental procedures. A wide range of techniques are used in this thesis to study different properties of ablation such as plume optical emission by using iCCD photography and time and space resolved emission spectroscopy. Absolute intensity calibration of the spectroscopic measurements can be used to quantify the amount of material in the plume. Ion time of flight is studied using a Langmuir ion probe. The techniques that are utilised to study the plume optical absorption, material removed and material deposited are described.

Chapter 4 introduces the experimental setup used for studying the femtosecond ablation plumes, describing the orientation and setup of each diagnostic technique. The ablation crater and material deposited will also be discussed in this section.

Chapter 5 discusses the results of a study of the fast, atomic plume produced by femtosecond laser ablation in vacuum. Langmuir ion probe measurements, iCCD imaging

and time- and space- resolved emission spectroscopy will be utilised to characterise the plume characteristics. The study will include gold, silver, aluminium and tin. Silver was chosen for an in-depth study of its atomic plume emission due to readily available atomic data.

Chapter 6 focuses on the slow, nanoparticle plume produced by femtosecond laser ablation. Initially, the study will focus on gold, showing in detail the results of various experimental techniques and a discussion based on how the optical properties of a material allows us to relate the observed intensity of the nanoparticle plume to the amount of material and the plume temperature. This analysis will then be applied to silver, aluminium and tin to study the variation in plume properties for each material.

Chapter 7 we will broaden our study to look at the effect of background gas confinement on plume propagation. In order to form a complete picture a light (helium) and relatively heavy (argon) gas were chosen to study the effect of the molecular weight of background gas on the ablation plume expansion. A wide pressure range was used to study the effect of background gas pressure on plume characteristics (10, 100 and 1000 mbar).

Chapter 2

Theory

In this chapter, the relevant theory for laser ablation is introduced. We will initially discuss the main mechanisms responsible for femtosecond laser ablation. While there has been many theoretical and experimental studies there is still some debate on the main formation mechanisms [13, 14]. Femtosecond laser ablation and plume formation is a combination of a number of complex processes; laser-material interaction and the coupling of energy to the lattice, vaporization, material fragmentation and phase explosion [15–17]. Femtosecond laser ablation results in the formation of two plumes, a fast atomic plume and a slower component comprised mainly of nanoparticles [18, 19]. As this work will mainly deal with experimental measurements of the ablated material the generally accepted mechanisms will be discussed. Next we will describe the Anisimov expansion model [20, 21]. This model describes an adiabatic, isentropic, self similar gas expansion. This model has previously been shown to be successful in describing a nanosecond laser produced plume expansion. The model can be used to describe the plume shape along with the pressure and density profiles within the plume.

The second part of this chapter will focus on the interaction of light with small spherical nanoparticles that can be described by the Rayleigh approximation. Finally, we will discuss the thermal properties of the nanoparticles. Typically, femtosecond laser ablation of metals results in the formation of hot nanoparticles which expand away from the target surface. A number of possible cooling mechanisms will be considered. In chapters 6 and 7, we will characterise the nanoparticle plume by measuring its light emission using optical emission spectroscopy, from which, we aim to deduce the dominant cooling mechanisms.

2.1 Femtosecond laser ablation

This section will explore the main formation processes involved in femtosecond laser ablation. A femtosecond laser produces laser pulses with duration on the order of 1 to a few hundred femtoseconds (10^{-15} s). At this short time scale, during the laser pulse, heat conduction into the target can be neglected. Femtosecond laser ablation can be described by three main processes; deposition of laser energy into the target, phase transformation of the irradiated region and expansion of the plume components. While there is currently not complete agreement in the scientific community on underlying processes of femtosecond laser ablation, we will discuss the generally accepted formation mechanisms and where possible make reference to areas of disagreement.

2.1.1 Laser absorption

For metals, the absorption of a femtosecond laser pulse is similar to that of nanosecond. The free electrons absorb the laser energy in a thin layer near the target surface determined by the optical absorption coefficient, described by equation 1.1. However, due to the short pulse length, the electrons are driven into an excited state compared to the lattice. The free electrons are in thermodynamic equilibrium with each other due to electron-electron collisional processes which occur on time scales on the order of 10 fs. The hot electron gas, due to electron-phonon interactions, transfers energy to the lattice on the order of the electron phonon coupling time of the target material, $\tau_e \approx 10$ ps for metals [22, 23]. Therefore, the temperatures of the electrons and lattice cannot be assumed to always be in equilibrium. In this case, the temporal and spatial evolution of the electron and the lattice temperatures, T_e and T_i, can be described by a one dimensional two temperature heat diffusion model [7, 17, 24–26]

$$C_e \frac{\partial T_e}{\partial t} = -\partial Q(z) \partial z - G(T_e - T_i) + S, \tag{2.1}$$

$$C_i \frac{\partial T_i}{\partial t} = G(T_e - T_i), \tag{2.2}$$

$$Q(z) = -k_e \frac{\partial T_e}{\partial z}, \qquad S = I(t) A \alpha e^{-\alpha z}, \tag{2.3}$$

where z is the direction perpendicular to the target surface, $Q(z)$ is the heat flux, S is the laser heating-source term, $I(t)$ is the laser intensity, A and α are the surface absorptivity and the material absorption coefficient, C_e and C_i are the heat capacities (per unit volume of the electron and lattice subsystems), G is the parameter characterising the electron-phonon coupling strength, and k_e is the electron thermal conductivity. The above equations can be solved by neglecting the lattice thermal conductivity since heat moves much faster through the electron sub system, and therefore get a numerical solution for T_i and T_e.

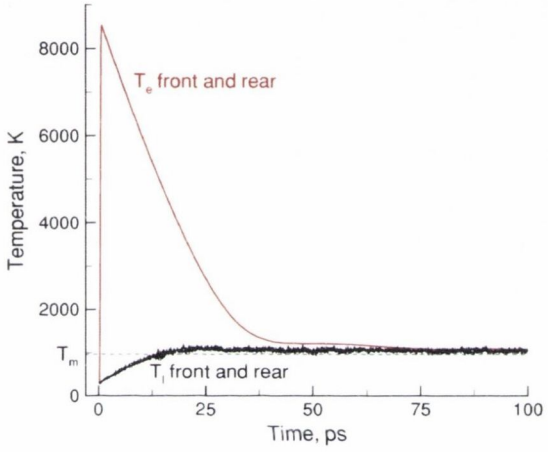

Figure 2.1: Simulation of femtosecond laser irradiation of a 50 nm thick gold target with a pulse length of 200 fs and an absorbed fluence of 1.3×10^{-2} J cm^{-2} showing the time dependence of electron and lattice temperatures at the front and back surfaces of the target. Reproduced from ref [17].

Ivanov et. al. modelled the femtosecond ablation of gold using a combined two temperature model and molecular dynamic simulation (TTM-MD) [17]. They studied the irradiation of a thin 50 nm gold target with a 200 fs laser pulse and an absorbed fluence of 1.3×10^{-2} J cm^{-2}. Figure 2.1 shows the variation of electron and ion temperatures at the front and rear of the 50 nm gold film. In this example, weak electron-phonon coupling and ballistic energy transport by excited electrons leads to homogeneous heating of the film. Initially, the electrons are excited and undergo isochoric heating such that the material density remains unchanged and reaches a temperature of > 8000 K. As the electron-phonon coupling time is on the order of picoseconds for metals, the lattice remains cold. The electrons transfer energy to the colder lattice by electron-phonon scattering. At ≈ 50 ps after the laser pulse the lattice and electrons reach equilibrium.

2.1.2 Ablation mechanisms

At higher fluences, femtosecond laser irradiation of the target leads to decomposition of material in a thin layer near the target surface. Wu et al. have applied a similar TTM-MD model to describe femtosecond laser irradiation of aluminium by a 100 fs pulse with an absorbed fluence of $0.2\,\mathrm{J\,cm^{-2}}$. Snapshots shown in fig. 2.2 visualise the ejection of material from the target from 50 - 450 ps after the laser pulse [27].

At 50 ps after the laser pulse, material at the target surface has vaporised and a fast, atomic plume is observed leaving the target. Within the target, void formation occurs. The growth and coalescence of multiple voids results in the formation of complex structures of interconnected liquid. At later times, the size of the voids is increased, the material is seen expanding away from the target but the interconnected liquid regions remain connected. To provide a broader look, fig. 2.3 shows a snapshot at 630 ps covering a greater distance from the target surface. A prominent feature of the plume, observed from fig. 2.3 is that clusters of different sizes originate from different depths within the target, this results in the front of the plume been predominately made up of vapour and small clusters. The larger clusters observed at the back of the plume are formed deeper within the target.

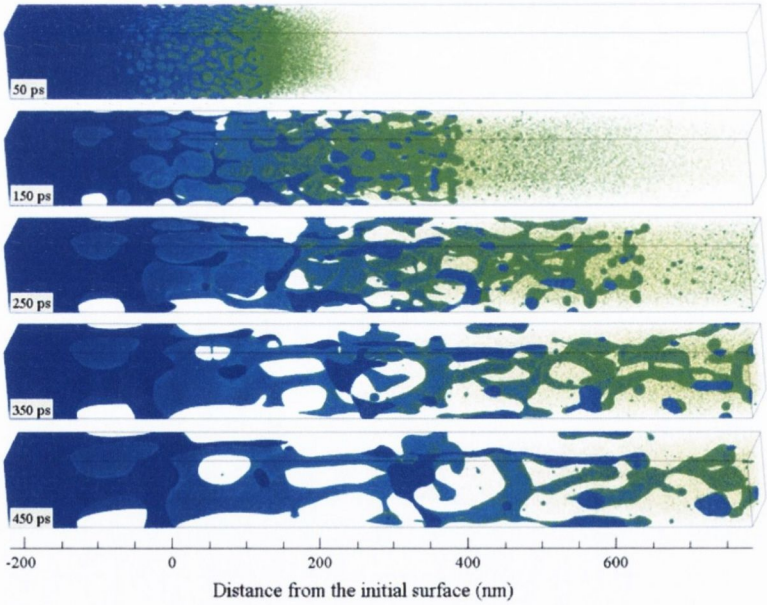

Figure 2.2: Snapshot of the atomic configurations predicted by a hybrid TTM-MD model of femtosecond ablation of aluminium with an absorbed fluence of $0.2\,\mathrm{J\,cm^{-2}}$. Reproduced from ref. [27].

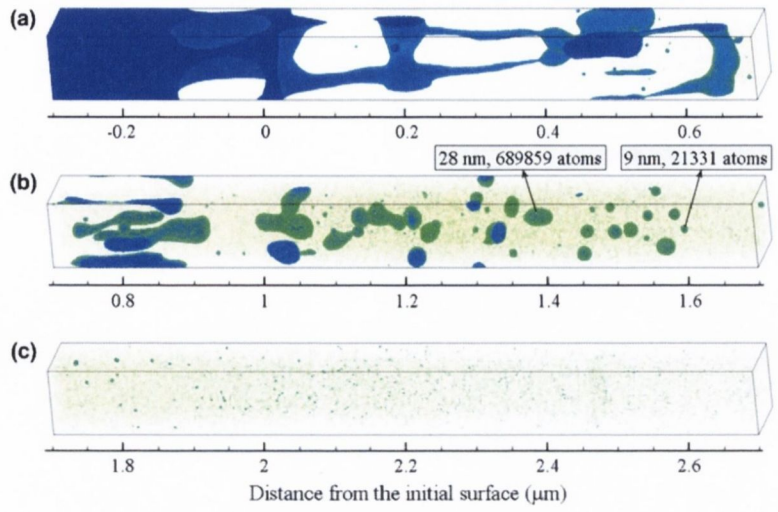

Figure 2.3: Snapshot of the atomic configurations 650 ps after the laser pulse predicted by a hybrid TTM-MD model of femtosecond ablation of aluminium with an absorbed fluence of 0.2 J cm^{-2}. (a)-(c) show an extended distance range from the target. Reproduced from ref. [27].

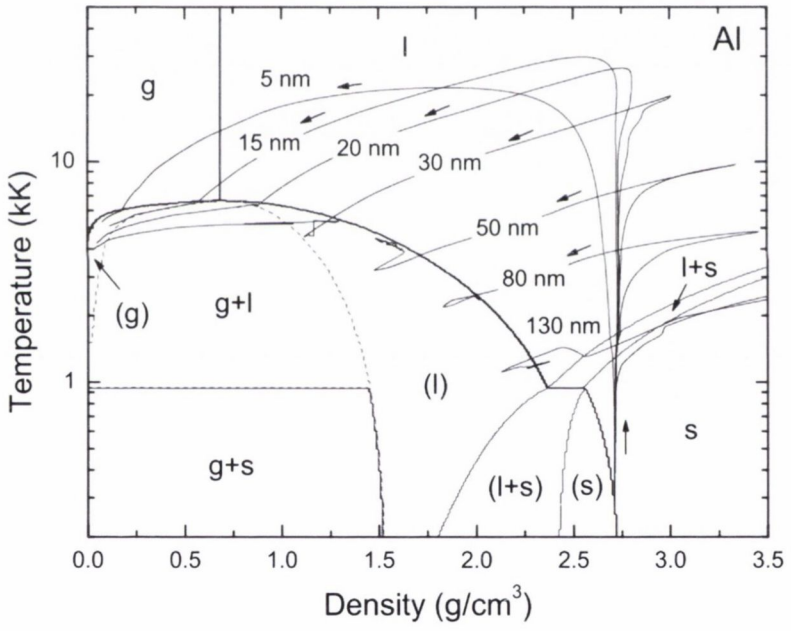

Figure 2.4: Phase diagram of aluminium showing the time evolution of density and temperature at different depths within the target. Dashed curve, the spinodal; g, stable gas; l, stable liquid; s, stable solid; l+s, stable melting; g+l, liquid-gas mixture; g+s, solid-gas mixture; (g) metastable gas; (l), metastable liquid; (l+s), metastable melting; (s), metastable solid. The phase trajectories correspond to depths of 5, 15, 20, 30, 50, 80 and 130 nm from the target surface. The laser pulse parameters are τ_l = 100 fs, λ = 800 nm, F = 5 J cm^{-2}. Reproduced from Povarnitsyn et al. ref [15].

For the discussion on the material relaxation methods we will focus on the numerical hydrodynamic study by Povarnitsyn et al. on the femtosecond ablation of aluminium [15]. Hydrodynamic calculations have the ability to model much larger systems as it is less

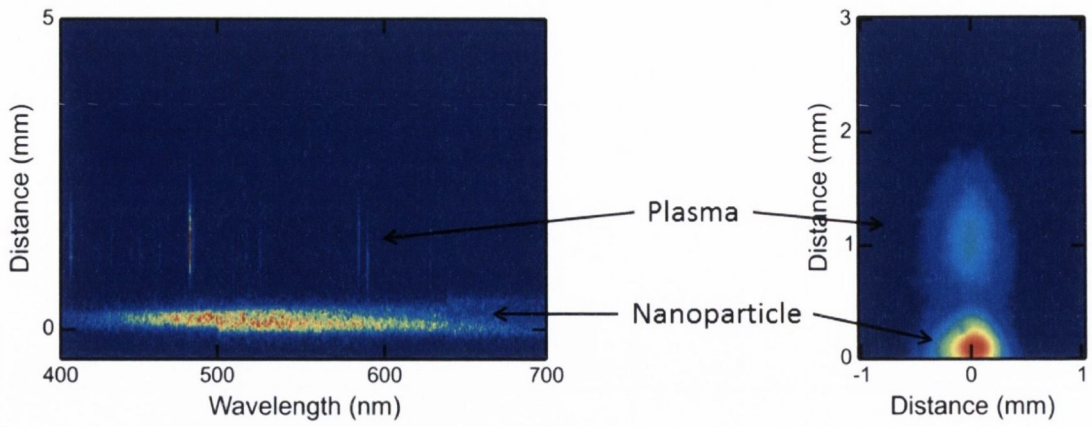

Figure 2.5: Time- and space- resolved spectroscopy and iCCD imaging recorded 200 ns after the laser pulse showing the atomic and nanoparticle plume components.

computationally expensive compared with MD simulations. Figure 2.4 is the calculated density-phase diagram for an aluminium target undergoing femtosecond ablation by a 800 nm, 100 fs laser pulse with a fluence of 5 J cm^{-2}. This figure shows how the material properties evolve at different depths within the target, dependent on the laser energy absorbed at that depth. As the thermal energy is transferred from the electrons the lattice undergoes rapid heating. The top-layer of the target reaches the highest temperature and undergoes atomisation. It proceeds above the critical temperature, T_c, and is directly transformed into the gas phase. The region close to the target surface, $\leq$ 15 nm reaches a temperature above the critical temperature, the target material is transformed into the gas phase, eventually this material cools, crosses the binodal line and a liquid-gas mixture forms. This regime is called critical point phase separation. Phase explosion occurs between approximately 20 - 30 nm. This layer crosses the binodal near the critical point, initially it forms a metastable liquid state which leads to rapid decomposition into a liquid-gas mixture. It has also been proposed by Perez et. al. that the mechanism responsible for matter that proceeds along this trajectory is in fact fragmentation [13, 14, 18]. Deeper layers enter the metastable region at $T \ll T_c$. In this case, the matter can have a much longer life time in the metastable state. Mechanical stress dominates over thermal effects and material fragmentation occurs resulting in the material decomposing into liquid droplets. However, Perez et. al. describes the ablation mechanism of deeper layers of the target as phase explosion [13, 14, 18]. As seen in fig. 2.3, as a result of multiple decomposition mechanisms the ablated material is segregated into distinct components.

After the decomposition of the target into its various components, the material is driven in a forward directed expansion away from the target due to the pressure gradient. As the material expands, it is observed to compose of two main, distinct components: (a) a

cloud of fast atomic species (neutrals and ions) which leaves the target surface at a high velocity and (b) a slower plume composed of nanoparticles shown in fig. 2.5 which are a result of complex material decomposition mechanisms previously discussed.

2.1.3 Ablation in the thermal regime

In the thermal regime, the laser pulse length is much longer than the electron-phonon coupling time, τ_{ep}. For metals, τ_{ep} is on the order of picoseconds. Therefore, for nanosecond laser ablation, the temperature of the electron and lattice subsystems are always in equilibrium.

The nanosecond ablation process can be described by three distinct steps; Laser absorption and heating of the target material, vapour and plasma formation, and plume expansion [28–30]. Figure 2.6 shows a simplified illustration showing the main processes involved in nanosecond laser ablation and their relative timings. 1. As the initial part of the laser pulse is absorbed, the target heats and a melt layer is formed which propagates into the target. 2. At sufficiently high laser intensities, a vapour layer forms. During the laser pulse the vapour layer can be further heated by inverse bremsstrahlung (section 2.3). At sufficiently high energy densities, this process can result in plasma formation [31]. Laser absorption by the vapour/plasma can shield the target from the laser pulse and result in the melt layer receding before the end of the pulse. 3. After the laser pulse the plume then undergoes a 3-dimensional semi-ellipsoidal expansion.

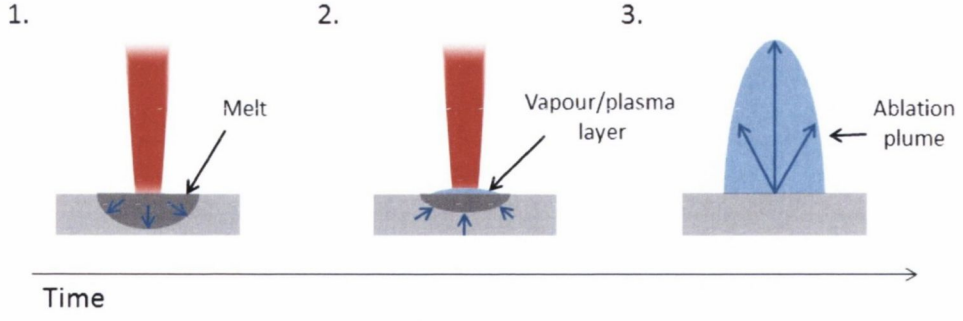

Figure 2.6: Schematic showing the main processes involved in nanosecond pulsed laser ablation; 1. laser absorption and melt layer formation, 2. plasma formation and absorption of the laser pulse and 3. plume expansion.

The laser pulse is absorbed in a thin layer of target material at the surface, described by the optical absorption coefficient, α and the ablation process can be described by a one dimensional heat flow equation [29, 32–34].

$$c_p\rho\left[\frac{\partial T(t,z)}{\partial t} - u(t)\frac{\partial T(t,z)}{\partial z}\right] = \frac{\partial}{\partial z}\left(k\frac{\partial T(t,z)}{\partial z}\right) + (1 - R_f(T))\alpha(t)I(t)exp(-\alpha(T)z) \tag{2.4}$$

where c_p, ρ, k, and α are the heat capacity, mass density, thermal conductivity and absorption coefficient of the target material respectively. R_f, z, and $I(t)$ are the target reflection coefficient, depth within the target and incident laser intensity respectively. $u(t)$ is the velocity of surface recession. This model can be solved numerically under certain assumptions of the initial conditions, $T(0, z)$, $T(0, \infty) = T_{initial}$ and has shown to give good agreement with experiment [35]. Equation 2.4 is difficult to solve because of the temperature dependent material properties and the moving solid-liquid interface. A detailed discussion on the temperature dependence of the absorption and reflection coefficients and their influence on ablation is given in refs. [36,37]. Once the target surface reaches the melting temperature, T_m, a melt layer forms and starts to evaporate forming a thin vapour layer on the target surface. The vaporisation flux can be obtained from the Hertz-Knudsen equation [33] and therefore, derive the surface recession velocity, u(t) as

$$u(t) = 0.82\frac{p_s}{\rho}\left(\frac{m}{2\pi k_b T(0,t)}\right)^{1/2} \tag{2.5}$$

where k_b, m, ρ, and p_s are the Boltzmann constant, average particle mass, density and gas/vapor pressure. The gas pressure, i.e. the pressure of this thin vapor layer can be estimated from the Clausius-Clapeyron equation [38]. This thin vapour layer attenuates the power of the incident laser beam reducing the intensity coupled to the target and further heats and ionizes the vapour plume. This shielding effect is a result of reflections from the vacuum-plume and plume-target interfaces, inverse bremsstrahlung absorption and photoionization within the vapour [33, 37, 39].

2.2 Plume expansion

After plume formation, the thin layer of plasma expands from the target surface in a forward directed expansion due to the pressure gradients perpendicular and parallel to the target. The expansion dynamics are strongly influenced by the initial plasma properties; initial dimensions, internal energy and the ambient conditions. There are a number of models available to describe this expansion depending on whether the plasma is allowed to expand freely (in vacuum) [20, 21, 40], or inhibited by a background gas [41–44]. For vacuum, most models use hydrodynamic methods to characterise the plume expansion [20, 45]. The plume expansion is described by the gas dynamic equations, expressing the conservation of mass and momentum as

$$\frac{\partial \rho}{\partial t} + \nabla \cdot (\rho v) = 0 \tag{2.6}$$

$$\frac{\partial v}{\partial t} + (v \cdot \nabla)v + \frac{1}{\rho}\nabla p = 0 \tag{2.7}$$

$$\frac{\partial S}{\partial t} + (v \cdot \nabla)S = 0 \tag{2.8}$$

where ρ, v, p, S are the plume density, velocity, pressure and entropy respectively. We will focus on the commonly used Anisimov model [20, 21], which has been shown to give good agreement with experimental data [46–48]. This model is based on the assumption that the expansion is adiabatic and isentropic. The solution to this model considers the plume parameters to be constant along ellipsoidal surfaces. This leads to expressions for the density and pressure profiles in the plume.

$$\rho(x, y, z, t) = \frac{M}{I_1(\gamma)XYZ}\left(1 - \frac{x^2}{X^2} - \frac{y^2}{Y^2} - \frac{z^2}{Z^2}\right)^{1/(\gamma-1)} \tag{2.9}$$

$$p(x, y, z, t) = \frac{E}{I_2(\gamma)XYZ}\left(1 - \frac{x^2}{X^2} - \frac{y^2}{Y^2} - \frac{z^2}{Z^2}\right)^{1/(\gamma-1)} \tag{2.10}$$

The variables, $I_1(\gamma)$, $I_2(\gamma)$, described in Ref. [20] are integrals involving γ and S. M and E are the mass and initial energy of the vapour plume. As shown in fig. 2.7, X_0, Y_0, Z_0 are the initial plume dimensions, $X(t)$, $Y(t)$, $Z(t)$ are the plume dimensions at time t.

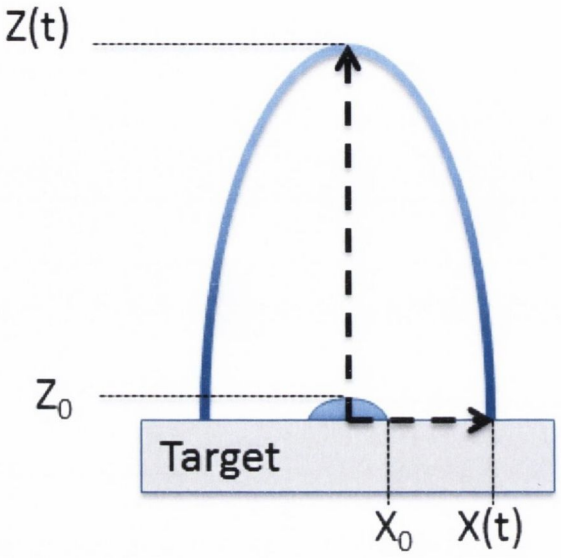

Figure 2.7: Schematic diagram depicting the evolution of plasma dimensions during expansion as described by the Anisimov model.

The gas dynamic equations, 2.6-2.8 can be reduced to ordinary differential equations

$$X\frac{\partial^2 X}{\partial t^2} = Y\frac{\partial^2 Y}{\partial t^2} = Z\frac{\partial^2 Z}{\partial t^2} = (5\gamma - 3)\frac{E}{M}\left[\frac{X_0 Y_0 Z_0}{XYZ}\right]^{(\gamma-1)} \tag{2.11}$$

with initial conditions of

$$X(0) = X_0, Y(0) = Y_0, Z(0) = Z_0, \frac{\partial X}{\partial t} = \frac{\partial Y}{\partial t} = \frac{\partial Z}{\partial t} = 0 \tag{2.12}$$

from this, the velocity is initially zero, the plume undergoes an acceleration phase, after which it expands at constant velocity. Numerically solving equation 2.11 provides the temporal variation of plume shape, often referred to in terms of the aspect ratio, k, which characterises the particle flux angular distribution, $k_{zx} = Z/X, k_{zy} = Z/Y, k_{yx} = Y/X$.

Figure 2.8 shows (a) the variation in plume radii and (b) aspect ratios versus time. This simulation was calculated for a nickel plasma with initial plume dimensions of X_0 = 500 μm, Y_0 = 250 μm, Z_0 = 50 μm, and energy per particle, E_p = 50 eV. Initially the

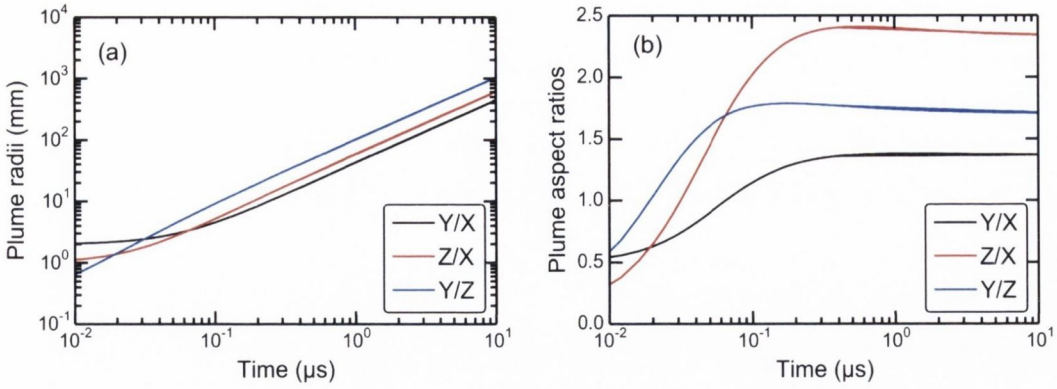

Figure 2.8: Evolution of the (a) plume radii and (b) plume aspect ratios, calculated using the Anisimov model.

plume radii and aspect ratio are equal to that of the initial plume dimensions. The plume accelerates in each dimension depending on the respective pressure gradients. The simulation also shows the expansion velocity is forward directed, this is due to a greater pressure gradient in the z-direction, caused by $Z_0 << X_0, Y_0$. The expression for plume temperature along the z-axis from the model is

$$T(z,t) = E_p \frac{(5\gamma - 3)(\gamma - 1)}{2\gamma} \left(\frac{X_0 Y_0 Z_0}{XYZ}\right)^{(\gamma-1)} \left[1 - \left(\frac{z}{Z}\right)^2\right] \tag{2.13}$$

Figure 2.9 shows the variation in plume temperature along the z-axis. The temperature at the plume boundary is zero which is as a result of the expansion assumed to be isentropic.

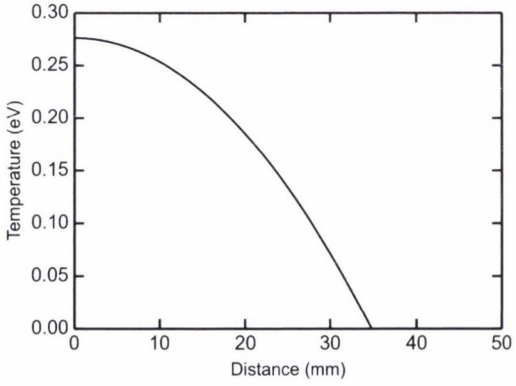

Figure 2.9: Temperature along the plume z-axis for t = 1 μs.

The Anisimov model describes the isentropic expansion of a hot vapour plume. Laser produced plasma plumes consist of an ionized gas. For a vapour plume to be isentropic,

the heat diffusion length s must be smaller than the plasma dimensions. Doggett et. al. showed that for a 1-dimensional plasma of length d, this condition is satisfied if [46]

$$T^2 < 1.05 \times 10^{-14} \gamma^{1/2} Z^{3/2} (Z+1) n_s d m_i^{-1/2} \tag{2.14}$$

where Z, n_s, m_i are the mean ion charge, the target atom density and the atom mass respectively. Taking $\gamma = 5/3$, $Z = 1$, $d = 10^{-6}$ cm for a silver plume, the expansion can be treated as isentropic if $T < 12.4$ eV. For this work, the plumes studied can therefore be assumed to undergo an isentropic expansion.

2.3 Optical emission spectroscopy

Optical emission spectroscopy is one of the most important diagnostic methods for measuring the conditions within a plasma plume. It is non-invasive and does not interfere with the plasma. Optical emission from an atomic plasma plume is as a result of the electrons undergoing radiative transitions. The main electronic processes that govern the optical emission from a plasma, depicted in fig. 2.10, can be divided up into three categories; bound-bound, free-bound and free-free transitions.

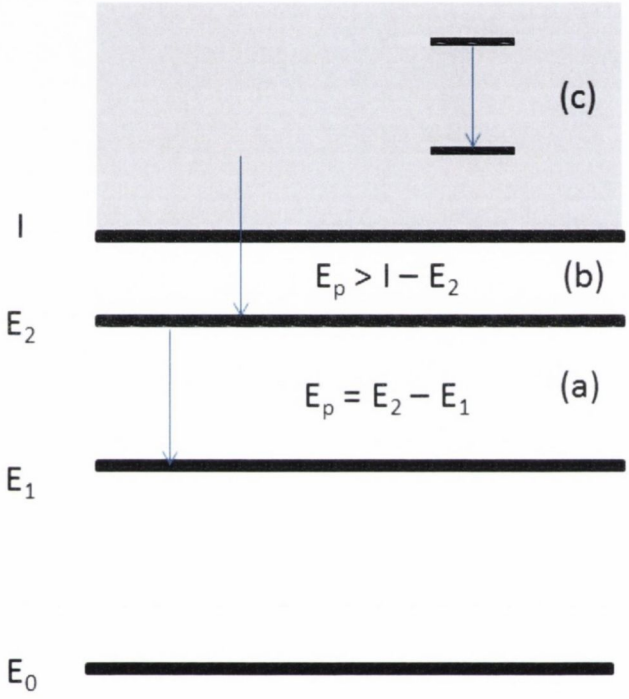

Figure 2.10: Simplified energy level diagram showing the 3 main types of transitions: (a) bound-bound, (b) free-bound, (c) free-free.

Bound-bound transitions occur when an electron moves from one discrete energy level to another, usually by photo-excitation or collisional processes. Free-bound occurs when a free electron loses energy by transitioning to a discrete energy level of an atom. The radiative free-bound transition is known as radiative recombination, the energy of the photon produced is equal to the difference in energy levels and the binding energy. Free-free transitions, also known as bremsstrahlung involve a free electron gaining or losing energy by interacting with other charged particles within the plasma.

Selection rules apply to transitions between radiately linked levels and therefore, transitions are not observed between all pairs of levels. The selection rules for allowed electric dipole transitions as as follows: the total spin cannot change, the change in total

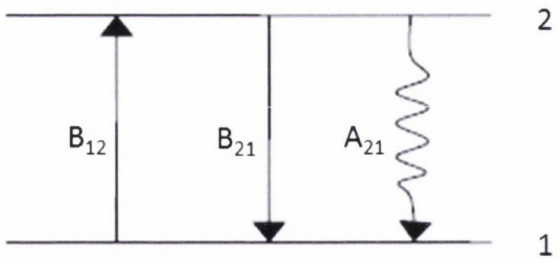

Figure 2.11: Two level system showing spontaneous emission (A_{21}), absorption (B_{21}) and stimulated emission (B_{12}) transitions.

angular momentum can be 0 or 1 but J=0 → J=0 is not allowed, the change in total orbital angular momentum can be 0 or 1 but L=0 → L=0 is not allowed and the initial and final wavefunctions must change in parity [49]. The probability of a transition by spontaneous emission from E_2 to E_1 is given by A_{21}

$$A_{21} = 4.34 \times 10^7 (h\nu)^2 \frac{g_1}{g_2} f_{12} \tag{2.15}$$

where g is the degeneracy of a given energy level, ϵ_0 is the permittivity of vacuum, f_{12} is the transition oscillator strength and ν is the frequency of the emitted photon. The intensity of a spectral line depends on the transition probability, the number density of atoms with an electron in the upper level, n_u and the probability that emitted photons will not be reabsorbed. This can be represented by a two level system.

Stimulated emission and absorption, shown in figure 2.11 can be represented by having transition rates of B_{21}, B_{12} respectively. Assuming the system is in thermodynamic equilibrium with the radiation field the transitions between E_2 and E_1 are equal and given by

$$A_{21} n_2 + B_{21} \rho(\nu_{12}) n_2 = B_{12} \rho(\nu_{12}) n_1 \tag{2.16}$$

where ρ is the radiation density. The Einstein coefficients, A_{21}, B_{21} and B_{12} are fixed probabilities associated with the atom and do not depend on the state of the plasma. From this, it is possible to derive a relationship between the Einstein coefficients assuming thermal equilibrium.

$$\begin{aligned} g_1 B_{12} &= g_2 B_{21} \\ A_{21} &= \frac{8\pi h \nu_{21}^3}{c^3} B_{21} \end{aligned} \tag{2.17}$$

The population distribution of the system can then be described by a Boltzmann distribution at a given temperature, T.

$$\frac{n_2}{n_1} = \frac{g_2}{g_1} e^{-(E_2 - E_1)/kT} \tag{2.18}$$

Therefore the relative line intensities are directly related to the transition probabilities and level populations. If the intensity of a given line follows a Boltzmann distribution then the plasma irradiance is given by

$$I_{21} = \alpha \frac{g_2 A_{21}}{\lambda_{21}} e^{\frac{-E_2}{kT}} \tag{2.19}$$

where α is a constant common to all lines, therefore a Boltzmann plot can be constructed for multiple lines of the same ionization species by graphing $\ln\left(\frac{I\lambda}{g_2 A_{21}}\right)$ versus E_2, the energy of the upper energy level with respect to the ground state. The slope of the resulting line is equal to $1/kT$, and hence one can solve for T. This method assumes that the plasma is optically thin and in local thermodynamic equilibrium (LTE). The A-values can be calculated from the oscillator strength and the level degeneracies, f_{12} by

$$f_{12} = \frac{\epsilon_0 m_e c \lambda_{21}^2}{2\pi e^2} \left(\frac{g_2}{g_1}\right) A_{21} \tag{2.20}$$

where λ_{21}, g_2, g_1, m_e are the wavelength of the emitted photon, degeneracy of the upper and lower levels and the electron mass respectively. There are a number of factors that determine the width of a spectral line such as Doppler, impact, and Stark broadening. Stark broadening comes from the Stark effect, which is caused by an atom or ion perturbed by an electric field resulting in splitting of energy levels, which can be described by

$$\Delta\lambda = \underbrace{2w\left(\frac{n_e}{10^{16}}\right)}_{\text{electron contribution}} + \underbrace{3.5A\left(\frac{n_e}{10^{16}}\right)^{\frac{5}{4}}}_{\text{ion correcton}} \tag{2.21}$$

where w, A, n_e are the Stark width parameter, ion broadening parameter and the electron density. The terms in equation 2.21 are the broadening contributions due to electrons (LHS) and ions (RHS), where the ionic term is generally negligible given the much slower response of ions to perturbations and hence equation 2.21 reduces to the electron contribution.

$$\Delta\lambda = 2w\left(\frac{n_e}{10^{16}}\right) \tag{2.22}$$

This equation can then be used to calculate the electron density of a plasma so long as accurate values of the Stark width parameters are know for a given transition [50].

The contribution of the other radiative mechanisms can also be considered. Free-bound radiative transitions (photo-recombination), shown in fig. 2.10, requires knowledge of the energy level structure of the atom and the transition rates. As a free electrons energy is not quantised it forms a semi continuous emission spectrum. The energy of the emitted photon is equal to the kinetic energy of the electron minus the binding energy. The simplest method of calculation is to assume a hydrogen-like ion or to make use of spectral synthesis codes such as FLYCHK and PrismSPECT [51, 52]. Bremsstrahlung radiation results in a broad continuum being observed as a free electron energy is not quantized and therefore the change of an electrons energy as it interacts with another charged particle does not result in discrete line emission. The spectral emission coefficient due to bremsstrahlung emission is given by

$$J_\nu d\nu = \frac{32\pi}{3}\left(\frac{2\pi}{3kTm}\right)^{1/2}\frac{Z^2e^6}{mc^3}N_I N_e e^{-h\nu/kT}d\nu \quad \mathrm{W\,m^{-3}\,Hz^{-1}} \tag{2.23}$$

where m, N_I, N_e and ν are the mass, ion density, electron density and frequency of the emitted photon.

2.3.1 PrismSPECT

Spectral modelling is a widely used method for determining plasma properties. In this thesis, we employ a commercially available, collisional-radiative spectral synthesis code, PrismSPECT [52]. For a set of input parameters, i.e. the plasma temperature, density and thickness of the plasma, PrismSPECT calculates the ionization, excited level populations, emission and opacity. PrismSPECT can be operated in LTE or non-LTE mode and accounts for opacity and instrumental broadening. An example of a simulated silver plasma emission spectra and its corresponding opacity is shown in fig. 2.12 for the conditions; atom density = $5 \times 10^{17}\,\mathrm{cm}^{-3}$, temperature = 0.8 eV, plasma thickness = 1 mm and mean ionisation, $Z = 0.58$. The mean ionisation is defined as

$$Z = \frac{\Sigma_0^{n_{max}} n_i z_i}{N} \tag{2.24}$$

where N is the total atom/ion density, n_i and z_i are the density and charge of particles of a particular ionisation, i. By comparing simulated plasma spectra with experiment we can deduce the plasma properties.

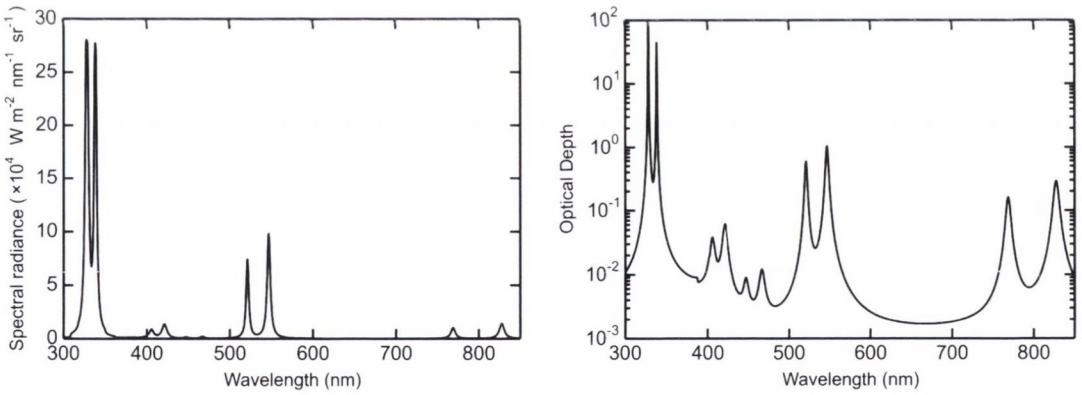

(a) Emission spectrum **(b)** Optical depth

Figure 2.12: Calculated (a) emission spectrum and (b) Optical depth for a silver plasma using PrismSPECT.

Simulating multiple spectra, PrismSPECT can show trends in how the variation of density/temperature can effect the other plasma properties. Figure 2.13a shows the variation of ion fraction with atom density at constant temperature. As the ion density increases the ionisation reduces. In fig. 2.13b, keeping the density fixed at $5 \times 10^{17}\,\mathrm{cm}^{-3}$, the variation of ion fraction of each species is plotted. As the plasma temperature increases, the mean ionisation also increases which will result in an increase in ion lines observed in the emission spectra.

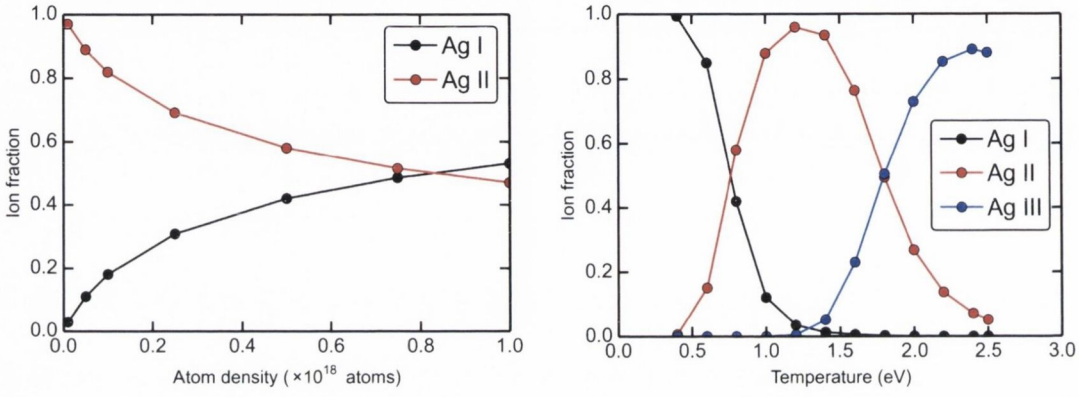

(a) (b)

Figure 2.13: Variation of the fraction of each ion component with (a) density at a fixed temperature of 0.8 eV, and (b) temperature at a fixed density of $5 \times 10^{17}\,\mathrm{cm}^{-3}$.

2.4 Interaction of light with small metallic particles

The interaction of electromagnetic radiation with small systems has been studied since the early 1900s with Gustav Mie's work on the light scattering by a sphere [53]. This work will focus on the interaction of visible light with metallic nanoparticles. Metallic nanoparticles are agglomerations of metal atoms with sizes ranging up to a few 100 nm. There are a growing number of applications of nanoparticles in a wide variety of areas such as drug delivery, electronics, magnetic materials and sensors [54–56]. The study of the optical response of nanoparticles is of particular importance as it is useful for applications, such as near-field enhanced optical microscopy, surface enhanced Raman spectroscopy and material characterisation [10, 57]. When light interacts with matter its electric field interacts with electrons inducing oscillations. These oscillating charges emit radiation in all directions known as the scattered field. The electron oscillations are damped by collisions which results in energy lost i.e. absorption. In 1908, Gustav Mie described how small gold spherical particles interacted with electromagnetic radiation to explain the colour of gold sphere colloids with changing diameters [53]. In this

thesis, we only deal with the Rayleigh approximation of Mie theory. This holds true for particles that satisfy the condition for the size parameter, $x = 2\pi a/\lambda \ll 1$, where a is the particle's radius. Rayleigh scattering is applicable to gas molecules found in the atmosphere and is responsible for the blue colour of the sky. When a particle's radius, a, is of the order of the wavelength of light this approximation is no longer valid and a different approach must be used which involves solving Maxwell's equations with certain boundary conditions. The Rayleigh approximation treats the particle as a single dipole with a polarisability, α, which depends on the size and refractive index

$$\alpha = 4\pi\epsilon_0 a^3 \frac{\epsilon_1 - \epsilon_2}{\epsilon_1 + 2\epsilon_2} \tag{2.25}$$

where ϵ_0, ϵ_1, ϵ_2 are the permittivity of free space, the complex relative permittivity of the nanoparticle and the permittivity of the surrounding medium respectively. For this work, the surrounding medium is assumed to be vacuum and hence $\epsilon_2 = 1$. The resonance occurs when the denominator of the polarisability is at its minimum, such that $\epsilon_1 + 2\epsilon_2 \approx 0$. This is known as a plasmonic resonance and results in a characteristic peak in the absorption, scattering and emissivity of the particles. Particles absorb, scatter, and if their temperature is above 0 K, emit electromagnetic radiation. The absorption cross section, C_{abs}, is defined as the rate the particle absorbs the light divided by the incident optical flux. The scattering cross section, C_{scatt} is defined as the rate the particle scatters the light divided by the incident optical flux. For a nanoparticle of radius a, the absorption and scattering cross sections are

$$C_{abs} = \frac{k}{\epsilon_0} \mathrm{Im}[\alpha] = 4\pi k a^3 \,\mathrm{Im}\left[\frac{\epsilon_1 - \epsilon_2}{\epsilon_1 + 2\epsilon_2}\right] \tag{2.26}$$

$$C_{scatt} = \frac{k^4}{6\pi\epsilon_0}|\alpha|^2 = \frac{8\pi}{3}k^4 a^6 \left|\frac{\epsilon_1 - \epsilon_2}{\epsilon_1 + 2\epsilon_2}\right|^2 \tag{2.27}$$

where $k = 2\pi/\lambda$. These equations can be written in terms of the refractive index since $\epsilon = m^2$, where m is the complex refractive index. Absorption and scattering cross sections for gold nanoparticles, calculated with bulk optical properties are shown in fig. 2.14. As $C_{abs} \propto a^3$ and $C_{abs} \propto a^6$, for small particles, $C_{abs} \gg C_{scatt}$ and hence is the dominant effect of the particle extinction.

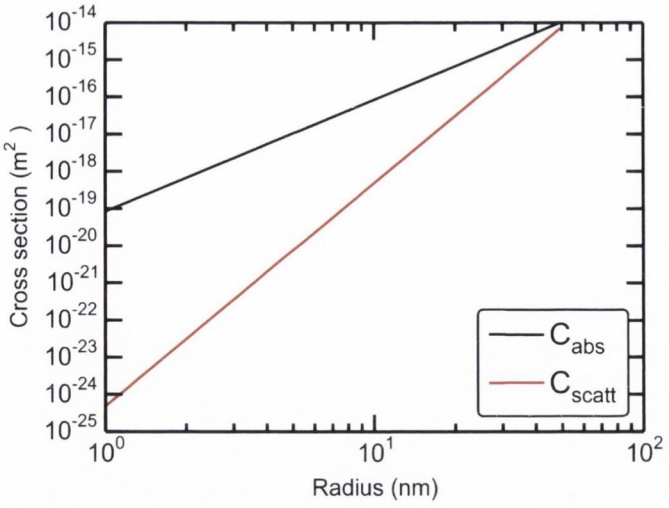

Figure 2.14: Calculated gold nanoparticle scattering and absorption cross sections at 532 nm versus particle radii.

The emissivity of a particle, $\epsilon(\lambda, a)$, is equal to the absorption efficiency of a particle, Q_{abs}, which is the ratio of the absorption cross section to the projected area of the particle, $Q_{abs} = C_{abs}/(\pi a^2)$. The nanoparticle emissivity is given by

$$\epsilon(\lambda, a) = \frac{8\pi a}{\lambda} Im\left[\frac{m^2 - 1}{m^2 + 2}\right] \tag{2.28}$$

where the emissivity is the ratio of the power emitted by the particle to the power emitted by a particle whose emission is described by the Planck function. Therefore, we can calculate the spectral emission from a nanoparticle for a known temperature.

Figure 2.15 shows the emissivity of a nanoparticle of radius 5 nm of various metals. Previously, the emissivity of a nanoparticle has been approximated as proportional to $1/\lambda$. From equation 2.28 this holds true if the optical constants can be assumed to be independent of wavelength. However, for most metals, the real and imaginary components vary over the visible spectral region (Appendix A.2).

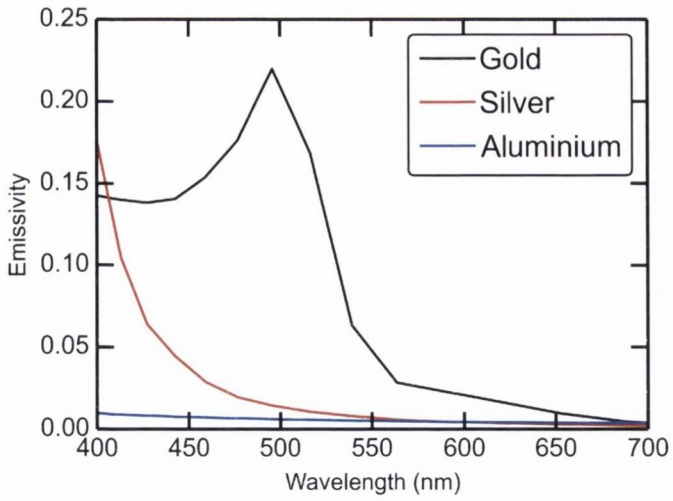

Figure 2.15: Calculated spectral emissivity of a 5 nm radius gold, silver and aluminium nanoparticles.

2.5 Nanoparticle cooling mechanisms

Thus far we have considered the optical properties of a single nanoparticle at room temperature. As part of this work, we studied the nanoparticle plume component of femtosecond laser ablated metals. It has been shown previously that within a few microseconds of the laser pulse hitting the target the nanoparticle temperature will be in the region of 1000-5000 K [58, 59]. Nanoparticles in this temperature range are liquid and emit a blackbody-like radiation in the visible spectral region [19, 58, 59]. It is important to consider the mechanisms by which the particles cool as the temperature of the particles may influence film growth in pulsed laser deposition. There are three cooling mechanisms for nanoparticles in vacuum to consider

1. Thermionic electron emission
2. Evaporation
3. Optical radiation

1. The rate of thermionic (electron) emission is given by the Richardson-Dushman formula modified due to the finite size of nanoparticles [60]. The rate of energy change by thermionic emission is given by

$$C\frac{dT}{dt} = -k(T,a)E_a \tag{2.29}$$

where C, $k(T,a)$, E_a are the heat capacity of the particle, decay rate and activation energy.

$$E_a = I_n = W_f + \frac{1}{2}\frac{n^2e^2}{4\pi\epsilon_0 a} \tag{2.30}$$

I_n is the n-th ionization potential. The activation energy of the first electron from the nanoparticle is equal to the work function, W_f. When considering this process it is important to note that with the liberation of each electron the nanoparticle will become charged. From equation 2.30, the charging of the nanoparticle causes an increase in activation energy and hence lower the decay rate with each successive electron emitted. The decay rate, $k(T,a)$, based on the activation energy is given by ref. [61].

$$k(T,a) = \frac{2k_BT}{h}\frac{Q_{vib}}{Q^0_{vib}}exp\left[-\frac{I_n}{k_BT}\right]\times\left(\frac{2a}{a_0} + \sqrt{\pi Q_{surf}} + Q_{surf}\right) \tag{2.31}$$

a_0 is the Bohr radius.Q^0_{vib}, Q_{vib} are the vibrational partition functions of the particle before and after emission and Q_{surf} is given by

$$Q_{surf} = 2m_e r^2 k_B T/\hbar^2 \tag{2.32}$$

where m_e is the electron mass and $\hbar$ the Dirac constant. It is assumed that there is a negligible change in the vibrational partition function and hence, $Q_{vib}/Q^0_{vib} = 1$.

Figure 2.16 shows the rate of temperature change during the emission of the 1^{st}, 2^{nd} and 3^{rd} electron from a 5 nm gold nanoparticle as a function of temperature. There is a significant reduction in decay rate with each successive emission. Assuming that the majority of energy lost in electron emission is due to to the activation energy and not the kinetic energy of the emitted electron the temperature loss due to the first 4 electrons is $\approx$ 3 K. It has been shown previously that for the cooling of niobium and tungsten nanoparticles thermionic emission only results in a small temperature change, < 5 K [62, 63]. While the change in temperature affects the decay rate, over the temperature range of interest thermionic emission will not result in an appreciable temperature change.

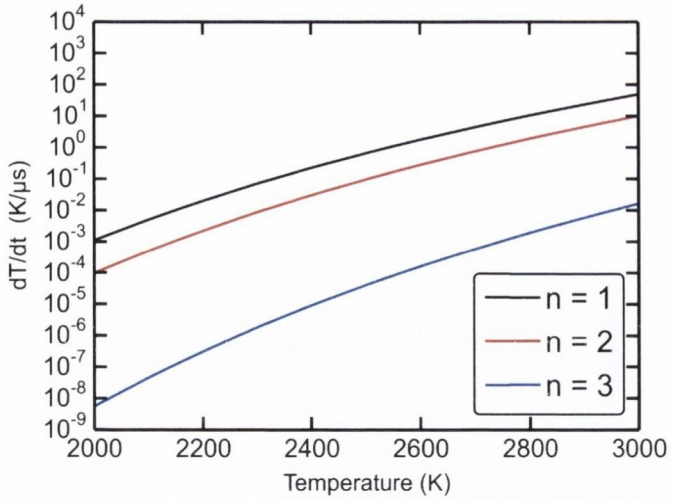

Figure 2.16: Calculated decay rates for thermionic electron emission for a gold nanoparticle of radius 5 nm.

2. The power lost due to evaporation can be calculated as evaporation from a bulk surface or evaporation from a small cluster which are described by the binding energy per atom and the evaporation rate

$$\begin{aligned} P_{ev,bulk} &= \epsilon \nu_{bulk} \\ P_{ev,NP} &= \epsilon \nu_{NP} \end{aligned} \tag{2.33}$$

where P_{ev}, ϵ, ν_{bulk} and ν_{NP} are the power lost due to evaporation, the binding energy per atom and the evaporation rate respectively. The bulk surface evaporation rate, given in ref [35] is defined by

$$\nu_{bulk} = A_s \frac{P_{sat}}{\sqrt{2\pi k_B T_s m}} \tag{2.34}$$

where P_{sat}, T_s, m are the saturation vapour pressure, surface temperature and atomic mass respectively. The evaporation rate from a nanoparticle, given by Smirnov et al. [63, 64].

$$\nu_{NP} = k_0 N_{sat}(T_s) \cdot exp\left(-\frac{2A}{3n^{1/3} T_s}\right) \tag{2.35}$$

where A and n are the specific surface energy of the cluster and number of atoms in the nanoparticle respectively. The reduced rate constant, $k_0 = \pi r_w^2 \sqrt{\frac{8T}{\pi m_a}}$ where r_w is the Wigner-Seitz radius. N_{sat} is the number density at the saturation vapour pressure and can be calculated from the saturation vapour pressure which is given by [35]

$$P_{sat}(T_s) = 1.06 \times 10^5 exp\left(\frac{L_v}{k_b}\left(\frac{1}{T_B} - \frac{1}{T_s}\right)\right) \tag{2.36}$$

where L_v, T_B are the latent heat of vaporisation and the boiling point respectively. For these calculations the bulk values are used. One potential source of error is the use of the bulk value for the material boiling point. It has been reported previously that, for nanoparticles, the melting temperature is lower than the bulk value, however, there is no information on whether this effect is also observed in the boiling point and therefore the bulk value is used [65]. Unlike thermionic emission the rate of evaporation is only weakly dependent on the number of previous events, therefore, even though initially thermionic emission has a faster decay rate, evaporation has a greater influence on the cooling of the nanoparticle. Figure 2.17 shows the rate of temperature change versus temperature calculated for a bulk surface and for a 5 nm radius gold nanoparticle. Both methods agree within 5% and thus a nanoparticle of this size can be approximated as a bulk surface and equation 2.34 is valid.

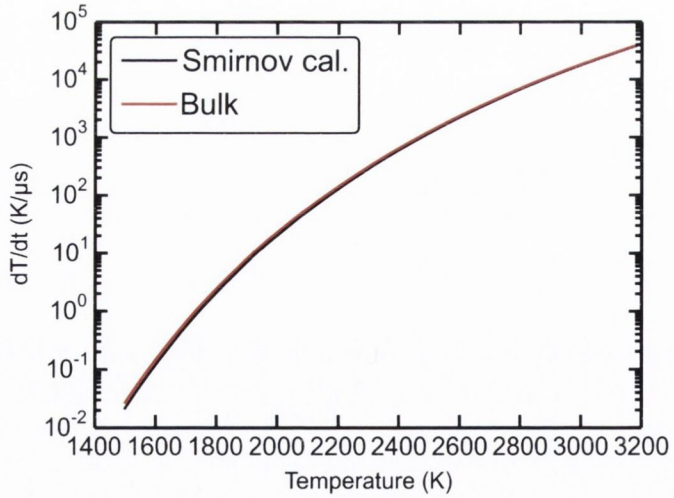

Figure 2.17: The rate of change of temperature due to evaporation from gold is calculated for a bulk surface and for a nanoparticle using formula described by Smirnov et al. [63, 64].

3. The optical power radiated from a blackbody is described by the Stefan-Boltzmann equation. This equation assumes a wavelength-independent, single-valued emissivity. Figure 2.15 shows the emissivity for gold, silver and aluminium nanoparticles and this is clearly not the case. The spectral intensity emitted from a single nanoparticle is given by

$$I(\lambda, a) = \epsilon(\lambda, a) \times \frac{2\pi hc^2}{\lambda^5} \frac{1}{e^{\frac{hc}{\lambda k_B T}} - 1} \qquad \mathrm{W\,m^{-2}\,nm^{-1}\,sr^{-1}} \tag{2.37}$$

where $\epsilon(\lambda, a)$ is the size and wavelength dependent nanoparticle emissivity. The power emitted by a nanoparticle and hence, the rate of temperature change is given by

$$C\frac{dT}{dt} = -4\pi A_s \int_0^\infty J(\lambda, a) d\lambda \qquad \mathrm{W} \tag{2.38}$$

where A_s is the particle surface area. The emissivity, $\epsilon(\lambda, a)$ is given by equation 2.28. Equation 2.38 simplifies to the Stefan-Boltzmann law if the emissivity is independent of wavelength. However, fig. 2.15 shows that that this is not the case and we must take into account the spectral dependence. Previously, Landström et al. approximated the emissivity of a tungsten nanoparticle as $\epsilon(\lambda, a) = \epsilon_c/\lambda$ [66]. Solving the integral in equation 2.38, they derived a modified Stefan-Boltzmann equation for an emissivity with a $1/\lambda$ dependence.

$$C\frac{dT}{dt} = -A_s \epsilon_c \sigma'_{SB} (T - T_0)^5 \qquad \mathrm{W} \tag{2.39}$$

where σ'_{SB} is the modified Stefan-Boltzmann constant, $\sigma'_{SB} = 3.84(k_B/hc)\sigma_B$. T_0 is the ambient temperature. Figure 2.18 compares two methods of calculating the power radiated from a hot nanoparticle, (1) Modified Stefan-Boltzmann and (2) numerical integration of a calculated blackbody curve.

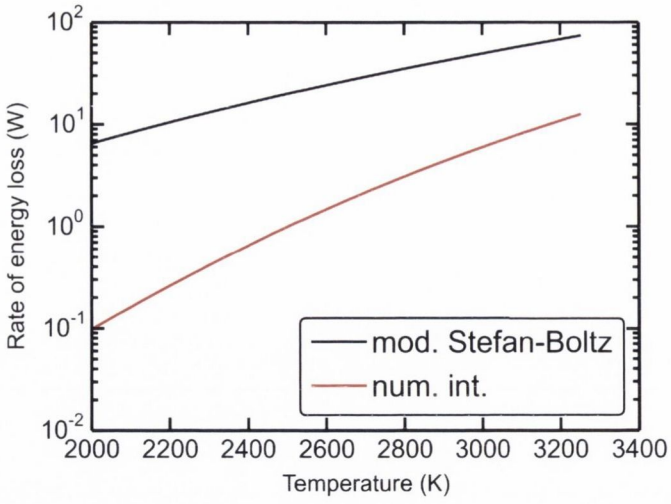

Figure 2.18: Calculated power radiated for a gold nanoparticle of radius 5 nm calculated using the different methods.

The value of emissivity chosen for the modified Stefan-Boltzmann calculation was 0.1 at 530 nm, this gives a value of $\epsilon_c = 5.3 \times 10^{-8}$. As seen in fig. 2.15, the emissivity of gold does not follow the $1/\lambda$ dependency and the choice of emissivity will strongly affect the calculated cooling rate. As the nanoparticles cool the peak of emission will shift from the visible to infra-red where gold has a greatly reduced emissivity. Therefore, in applying this method of calculating the cooling rate the appropriate choice of ϵ_c is different at different temperatures.

Chapter 3

Experimental methods

In this chapter, the main experimental and analysis methods are described. A general description of the experimental setup is given. The exact beam profile, fluence, optical delivery system are described in the relevant chapter specific to each experiment. We will focus on discussing the main characterisation methods used; time and space resolved emission spectroscopy, Langmuir ion probe analysis, optical absorption measurements and thin film depositions. Other characterisation methods used, but not discussed in this chapter include; scanning transmission electron microscopy (STEM) and intensified charge-coupled device (iCCD) imaging.

3.1 Experiment setup

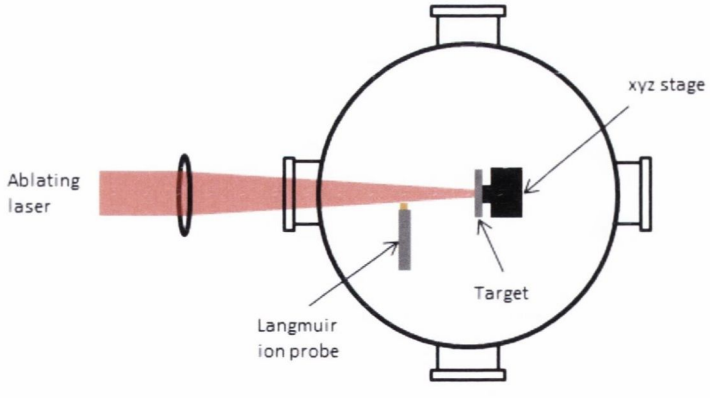

Figure 3.1: Schematic diagram of a standard laser ablation chamber setup.

Figure 3.1 shows a diagram showing a general laser ablation setup. The laser beam is focused to an intensity above the damage threshold so that ablation is achieved. Typically, the damage threshold for ablation of a copper target is, for femtosecond ablation,

$\approx 0.1\,\mathrm{J\,cm^{-1}}$ and for nanosecond, $\approx 0.6\,\mathrm{J\,cm^{-1}}$ [67, 68]. The ablation depth is typically on the order of tens to hundreds of nanometers depending on the ablation conditions.

Laser ablation is usually carried out in vacuum, or low pressure background gas, in a vacuum chamber. The addition of background gas can be used to lower the ion energy distribution, or as a reactant for gas-phase chemistry. The Langmuir probe is usually positioned between 5-15 cm from the target. Its optimal size is dependent on the distance and number of ions in the plume. The target is positioned on a translational stage (rotational or x-y rastering) to avoid drilling a pit into the target. Ablating the same point in the target creates a crater within which the plasma is formed. This crater acts to laterally confine the plasma and will change the shape of the plume expansion the greater the number of shots fired on the same position. Therefore, for conducting repeatable ablation events the target position has to be constantly adjusted.

3.1.1 Laser systems

The femtosecond laser system (Coherent Legend Elite) used for ablation consists of an oscillator (Coherent Micra), a pulse stretcher and a Ti-sapphire regenerative amplifier with pulse compressor. The exact specifications are summarised in table 4.1. The oscillator produces a high repetition rate, low energy femtosecond pulses which is used to seed the regenerative amplifier. The regenerative system consists of a multi pass pulse stretcher, an optically pumped Ti:Sapphire amplifier and a pulse compressor. This outputs a 1 kHz, 130 fs, 1 mJ per laser pulse at 800 nm.

Table 3.1: Laser systems

Laser	Wavelength	Rep. rate	Power	Pulse duration
Micra (seed laser)	800 nm	80 MHz	0.5 W	130 fs
Legend Elite (amplifier)	800 nm	1 kHz	1 W	130 fs

Temporal pulse shape measurement is usually carried out using a time resolved photodetector. However, fast photodiodes rise times are on the order of several picoseconds, much longer then the laser pulse length (130 fs). To solve this issue we use a commercially available auto-correlator (APE pulseCheck). This particular system allows pulse measurements in the range of 50 fs - 3.5 ps full width half maximum (FWHM). A simplified diagram indicating the main components of the auto-correlator is shown in fig. 3.2. Firstly, a beam splitter (BS) splits the beam into two beam lines, one a fixed length line, and second, a variable delay line. The two beams are recombined on the second

harmonic generation (SHG) crystal. The difference in the length of each beam line results in a different intensity profile in the crystal. The transmission through the SHG crystal is intensity dependent, which gives a different transmitted signal detected on the detector. The autocorrelation signal is given by

$$A^{(2)}(\tau) = \int_{-\infty}^{\infty} I(t)I(t-\tau)dt \tag{3.1}$$

where $A^{(2)}(\tau)$, is the auto-correlation signal and τ is the delay applied to the second arm of the interferometer relative to the first. $I(t)$ and $I(t-\tau)$ are the beam intensity through the reference line and the beam intensity through the delay line respectively. Multiple shots are used with a variation in the delay line timing to build up a symmetrical trace related to the femtosecond laser pulse temporal width. In order to obtain the real pulse duration a temporal pulse shape must be assumed. Assuming a Gaussian pulse shape, the laser pulse length, τ_l is equal to the ratio of the FWHM of the auto-correlation pulse, τ_{ac} divided by the Gaussian deconvolution factor, 1.41.

$$\tau_l = \tau_{ac}/1.41 \tag{3.2}$$

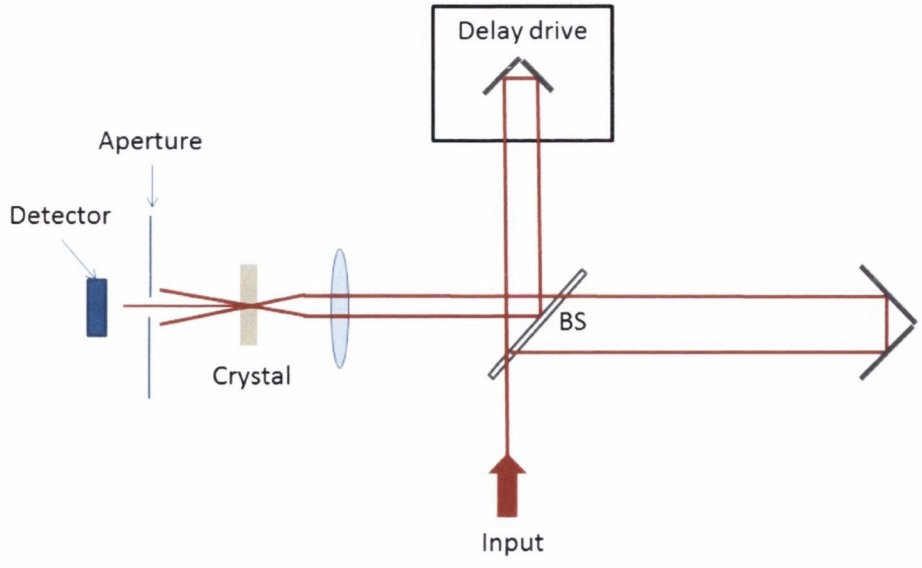

Figure 3.2: Setup of auto-correlator.

3.2 Spectrometer calibration

For the measurement of the spectral optical emission we use a Czerny-Turner spectrograph (Oriel MS 260i) coupled with a time resolved iCCD camera. The optical configuration of this spectrometer is shown in figure 3.3 which allows for spatial resolution along one axis. The spectrometer was equipped with 3 gratings, 1200, 600 and 300 l/mm. The spectral resolution was determined by measuring the width of the 546 nm line produced by a low density mercury lamp and found, for the 300 l/mm grating, to be 0.8 nm. The iCCD camera (Andor 334T) can be gated to a minimum of 2 ns, this can be incremented in steps of 1 ns.

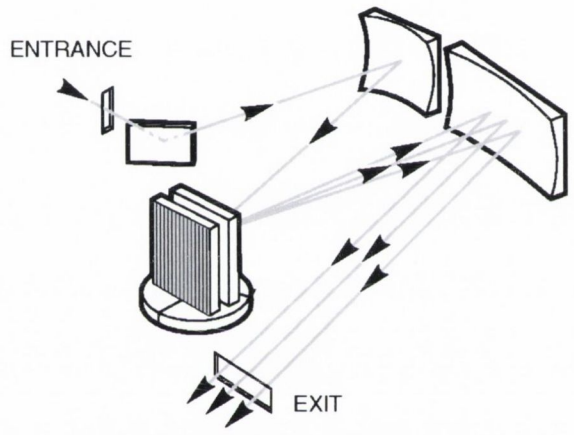

Figure 3.3: Optical setup of Oriel MS260i.

By using a source of known spectral intensity the spectral radiance of the plasma can be calculated from the number of counts recorded by the spectrometer iCCD camera. The number of counts recorded by a pixel depends on the MCP gain, gate time and the responsivity of the iCCD at a given wavelength. The counts measured from the plasma plume can be calibrated by imaging a known spectral irradiance through the optical system. A 100 W tungsten lamp, which produces a known spectral irradiance when placed 50 cm from the imaging plane was imaged through the optical system onto the spectrometer slit. This allows us to define a function $F(\lambda)$ that accounts for all losses that occur due to the light collection optics. $F(\lambda)$ can be found from the number of counts, C_L detected by the iCCD when the lamp is imaged through the optical system, shown in figure 3.4 and is given by the equation

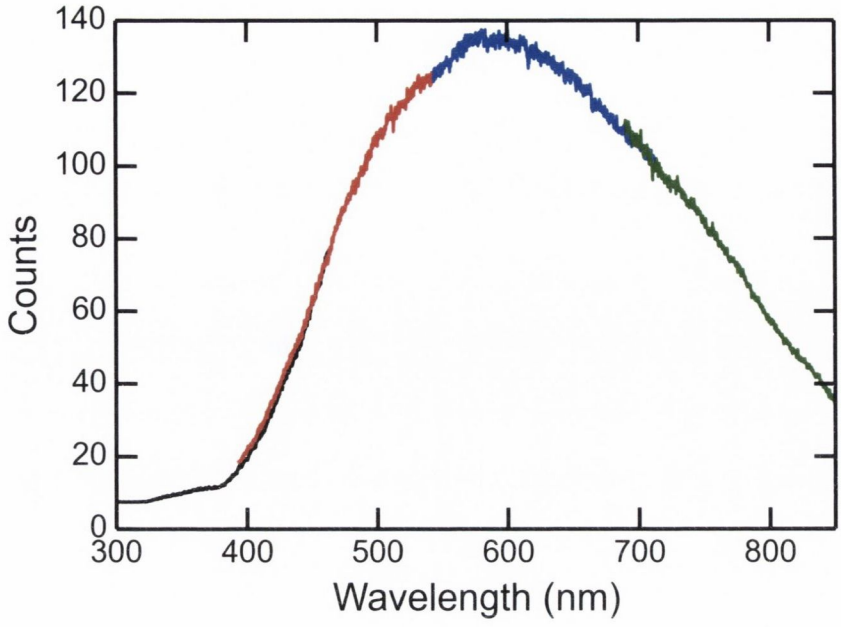

Figure 3.4: Counts recorded from the tungsten halogen lamp in the visible spectral region with camera settings of; gate time of 50 μs, gain of 3500 and 10 acquisitions.

$$C_L(\lambda) = F(\lambda) I_L(\lambda) n_L^{Aq} n_L^{Px} \Delta t_L \tag{3.3}$$

where n_L^{Px}, n_L^{Aq} and Δt_L are the number of number of pixels binned , the number of acquisitions and the gate width used to record the lamp spectral irradiance. The solid angle of the lamp emission at the plasma position is less then the solid angle of the optical collection system. Therefore, there is no light lost due to the geometry of the optical system when recording the lamp counts, $C_L(\lambda)$. $I_L(\lambda)$ is the calculated lamp spectral irradiance, shown in figure 3.5.

$$I_L(\lambda) = A_{fit} \cdot 10^{-9} \frac{2\pi hc^2}{\lambda^5} \frac{1}{e^{\frac{hc}{\lambda kT}} - 1} \qquad \mathrm{W\,m^{-2}\,nm^{-1}} \tag{3.4}$$

The fitting constant, $A_{fit} = 7.64 \times 10^{-6}$ and the lamp temperature, $T = 3317.8$ K. The counts measured from the plasma optical emission can be given by the relation

$$C_P(\lambda) = F(\lambda) L_P(\lambda) \Omega n_P^{Aq} n_P^{Px} \Delta t_P \tag{3.5}$$

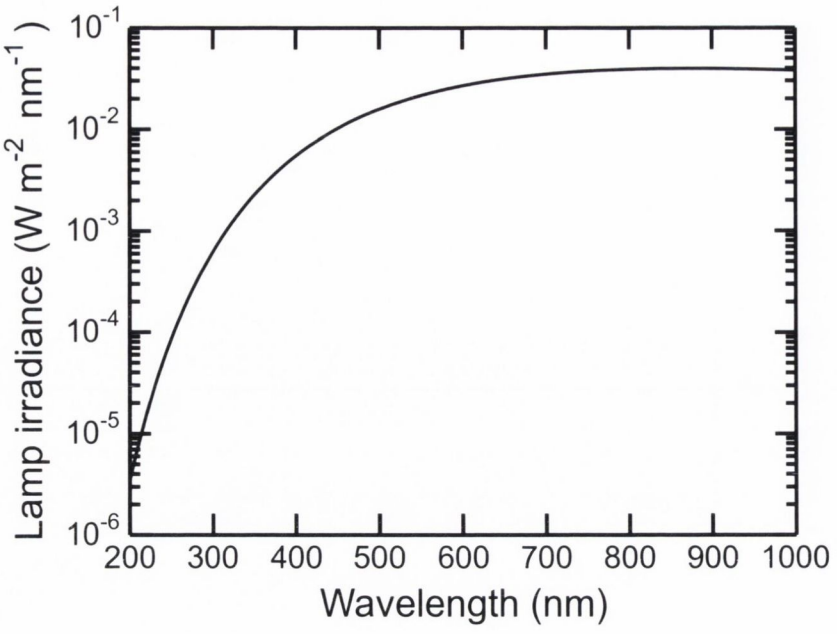

Figure 3.5: Irradiance at 50 cm from the quartz tungsten halogen calibration lamp.

where n_P^{Px}, n_P^{Aq}, Δt_P and $L_p(\lambda)$ are the number of number of pixels binned, the number of acquisitions, the gate width used to record the plasma spectral irradiance and the plasma spectral radiance. Ω is the solid angle of the optical collection system. Comparing equations 3.3 and 3.5 we can derive a relation to give the spectral radiance of the plasma.

$$L_p(\lambda) = \frac{C_P(\lambda) I_L(\lambda) n_L^{Aq} n_L^{Px} \triangle t_L}{C_L(\lambda) n_p^{Aq} n_p^{px} \triangle t_p \Omega} \qquad \mathrm{W\,m^{-2}\,nm^{-1}\,sr^{-1}} \tag{3.6}$$

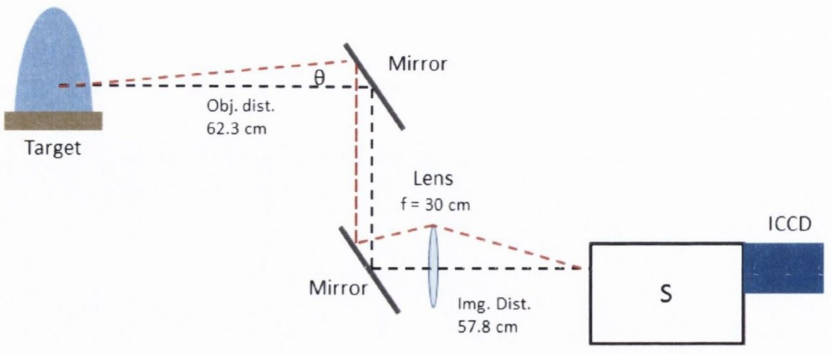

Figure 3.6: Spectrometer optical imaging system setup.

Figure 3.6 shows a typical optical imaging system. The plasma plume was imaged onto the spectrometer slit using a 30 cm planoconvex lens with a magnification of 0.93. The

slit dimensions were 50 μm × 3 mm giving a maximum object size of 3.2 mm. The maximum angle at which the light emitted from the plasma and would be collected and delivered by the optical system was calculated and the solid angle, Ω, was found to be 1.27×10^{-3} sr. The optical system described was used to characterise early nanosecond spectral emission (Appendix A.1).

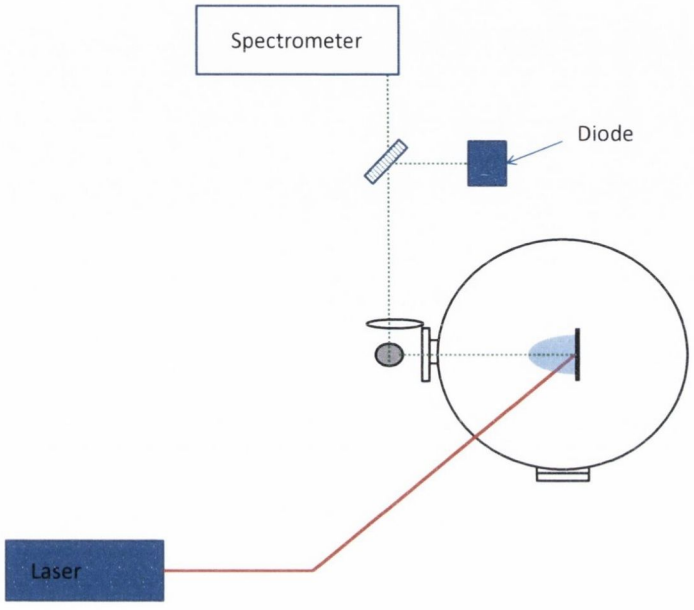

Figure 3.7: Simplified diagram showing the spectrometer and diode optical emission measurements.

In order to verify the validity of the spectral intensity calibration method, an alternative approach was used. Figure 3.7 shows a simplified diagram of the spectrometer optical imaging system. The system was aligned so that the optical axis was along the normal of the target. This results in the laser spot directly imaged onto the slit and a spatially a uniform region of emission was observed. A removable mirror was installed in the system to facilitate the positioning of a photodiode at the image plane of the plasma emission. The calibrated Thorlabs photodiode (TDC001) has a 1 ns rise time, to provide temporal resolution, and biased with a 12 V battery so that there is a linear relationship between light irradiance and output voltage.

Using a band-pass filter (532 nm, FWHM 40 nm) we can experimentally measure the intensity of the lamp in the pass region and compare with the absolute intensity calibrated spectra in fig. 3.8. The relationship between the output voltage of the photodiode and the power incident on the diode is given by

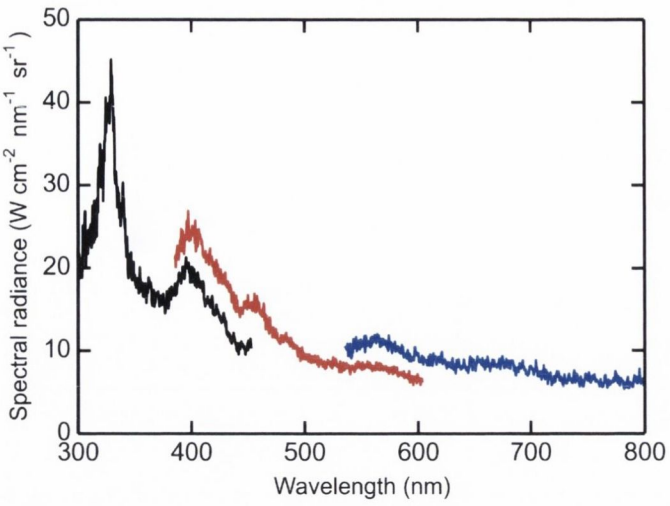

Figure 3.8: Calibrated silver spectral emission recorded during the first 10 ns of optical emission. The plume was formed using an 8 ns Nd:YAG with a fluence of 4 J cm^{-2}.

$$V = P \times R(\lambda) \times R_{load} \tag{3.7}$$

where P is the incident power, $R(\lambda)$ is the responsivity in A W^{-1} and R_{load} is the load resistor (50 Ω). The in-band plasma radiance is given by

$$L = \frac{V}{T\Omega\, A\, R(\lambda)\, R_{load}\, \Delta\lambda_{pass}} \qquad \text{W m}^{-2}\,\text{nm}^{-1}\,\text{sr}^{-1} \tag{3.8}$$

where A is the diode area (1 mm diameter circular active area), Ω is the solid angle and $\Delta\lambda_{pass}$ the filter band-pass (40 nm). The spectrometer calibration takes into account the transmission of the optical system as it relates the theoretical output of the tungsten lamp and the number of counts detected by the CCD camera. The reflectivity of each mirror and the transmission of the band-pass filter and lenses at 520 nm is ≈0.87. There are 5 mirrors and lenses in the system therefore the total transmission of the system, $T \simeq 0.87^5$.

Figure 3.9 shows the photodiode signal calibrated for plasma intensity using equation 3.8. The plasma spectral radiance during the first 10 ns of emission was found, using the photodiode to be 6.9 W cm^{-2} nm^{-1} sr^{-1}. From figure 3.8 above, the spectral radiance at 520 nm measured using the emission spectrometer is 8.25 W cm^{-2} nm^{-1} sr^{-1}.

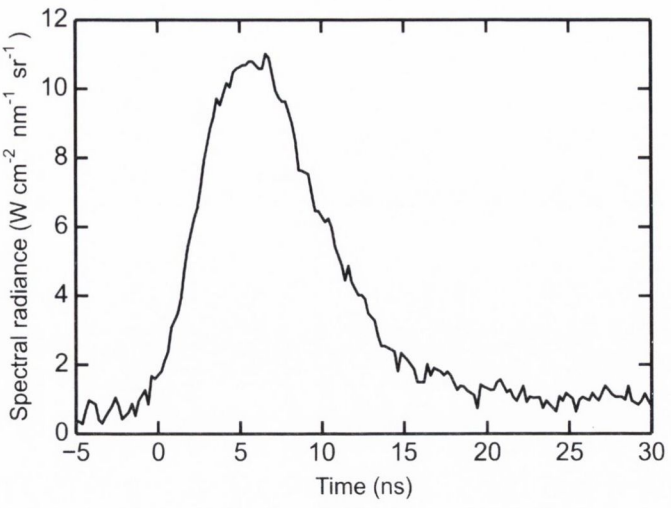

Figure 3.9: Absolutely calibrated photodiode signal of silver plasma optical emission in the spectral range between 500 - 540 nm.

3.3 Langmuir probe

Langmuir probes are one of the oldest, yet effective, methods of characterising laboratory plasma plumes in vacuum or low pressure background gas. The Langmuir probe can be used to measure a number of the plasma properties including; the ion and electron density, electron temperature, ion velocity and ion kinetic energy [69]. It is a relatively cheap diagnostic method, but it is invasive, in the sense that it needs to be placed in the plasma. The probe was developed by Langmuir and its use as a diagnostic in flowing plasmas was developed by Koopman using a simply biasing circuit [70, 71]. The probe consists of a small conducting electrode, typically a metal wire is used. For this work we use a metal planar plate, with insulating back and side surfaces, placed in the path of the expanding plasma plume. A small biasing circuit, shown in figure 3.10, is used to produce an electric field at the probe surface. Two conditions must be satisfied when deciding on the components for the biasing circuit.

1. The total charge collected by the probe must be much less than the stored charge in the capacitor, C_1.

2. The voltage drop measured over the load resistor must be much less than the biasing voltage (V_1) applied to the probe.

The probe can be biased positively or negatively. Due to the quasi-neutral nature of the plasma the probe bias will only influence charged particles within a few Debye lengths from its surface. This region is called the probe sheath. To detect ions, the probe voltage

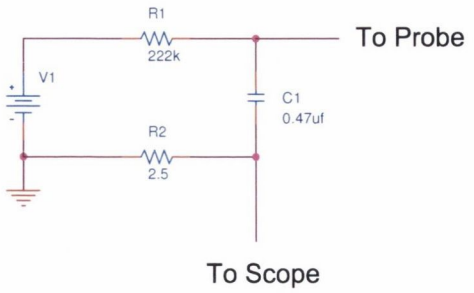

Figure 3.10: Langmuir probe bias circuit diagram.

is biased negatively. With a high enough negative bias (typically ≈ -15 V) the recorded ion current will saturate when electrons with the highest energy are prevented from reaching the probe. The ion current becomes independent of the applied voltage and is given by

$$I = n_i e A \upsilon_i \tag{3.9}$$

where A is the probe area, n_i is the ion density and υ_i is the ion velocity, which is calculated by assuming the plasma expands at a constant velocity and hence can be inferred from the probe signal.

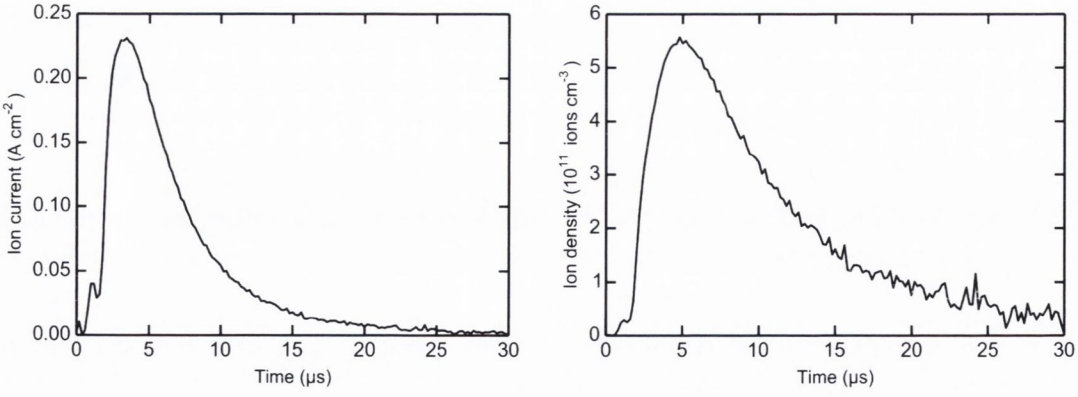

(a) Ion current **(b)** Ion density

Figure 3.11: (a) Langmuir ion probe signal of silver measured at 10.5 cm from the target, and (b) corresponding ion density profile. The plume was formed using a fluence of 4 J cm^{-2} from a 1064 nm, 8 ns Nd:YAG.

Figure 3.11 shows an example probe signal and derived ion density for ablated silver in vacuum recorded at 10.5 cm from the target. The silver target was irradiated with a 1064 nm, 8 ns pulse with an incident fluence of 4 J cm^{-2}. The velocity and ion energy distributions can be calculated from the probe signals by [46]

$$\frac{dN}{dv} = \frac{I(t)t^2}{Aed} \tag{3.10}$$

$$\frac{dN}{dE} = \frac{I(t)t^3}{Amed^2} \tag{3.11}$$

where m is the ion mass and d is the probe-target distance. The plasma undergoes an initial acceleration phase, after which, it then expands at constant velocity. The plume velocity can be inferred as $v = x/t$, and $E = 1/2mv^2$. An example velocity and energy distribution is shown in 3.12. The average ion energy can then be found from the ion energy distribution using the following equation

$$\langle E \rangle = \frac{\int E\frac{dN}{dE}dk}{\int \frac{dN}{dE}dk} \tag{3.12}$$

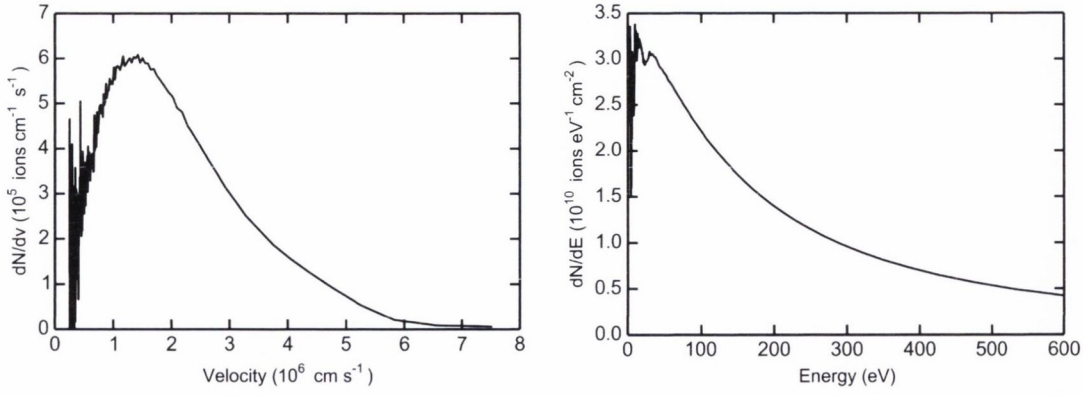

(a) Velocity distribution **(b)** Energy distribution

Figure 3.12: Velocity and ion energy distributions calculated from the ion probe signal given in fig. 3.11.

The average ion energy is an important factor in PLD, if sufficiently high ion energies are present it can lead to a significant amount of sputtering of the material newly deposited

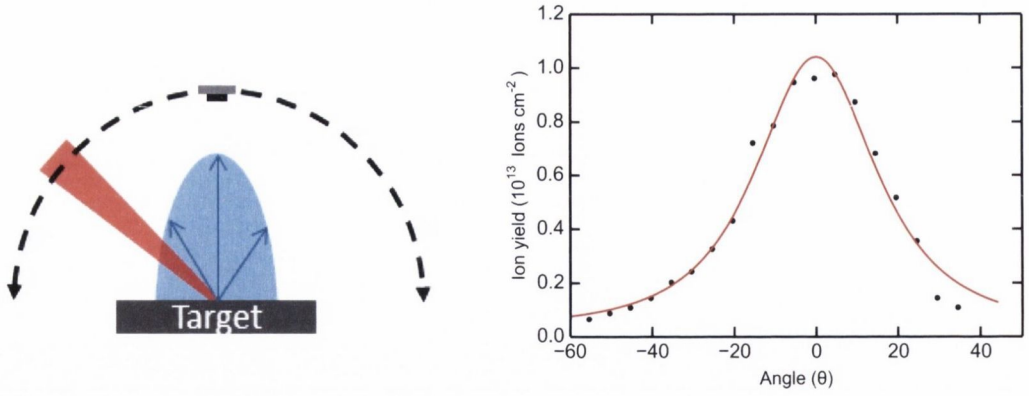

(a) Experimental setup **(b)** Integrated angular ion flux

Figure 3.13: (a) Diagram typical rotational probe geometry and (b) Angular variation of ion yield for the same ablation conditions as in fig. 3.11.

on the substrate and cause damage to the substrate itself. The total ion yield in the plume can be calculated from the angular dependence of the ion yield, given in fig. 3.13

$$N = \frac{2\pi d^2 F(0)}{k_{xz} k_{yz}} \tag{3.13}$$

where N, $F(0)$ are the total ion yield and ion fluence normal to the target. The plume shape is described by the aspect ratios k_{xz} and k_{yz} in the x-z and y-z planes. The shape of the plume expansion is related to the plasma initial dimensions, X_0, Y_0 and Z_0. X_0 and Y_0 can be approximated as having the same dimensions as the ablation crater. The initial thickness of the plume normal to the target surface, Z_0, is the thickness of the plasma at the end of the laser pulse which can be approximated as the product of the sound velocity and the laser pulse length.

3.4 Nanoparticle optical absorption

As discussed in section 2.1, the nanoparticle plume consists of a hot nanoparticle ensemble with a polydisperse size range. Currently, the main diagnostic methods used to characterise nanoparticle plumes are thin film depositions and emission spectroscopy. However it is advantageous to apply time resolved single wavelength absorption measurements. Unlike in the case of emission, nanoparticle absorption is weakly dependent on the plume temperature and is not reliant on the nanoparticles been sufficiently hot to produce observable emission.

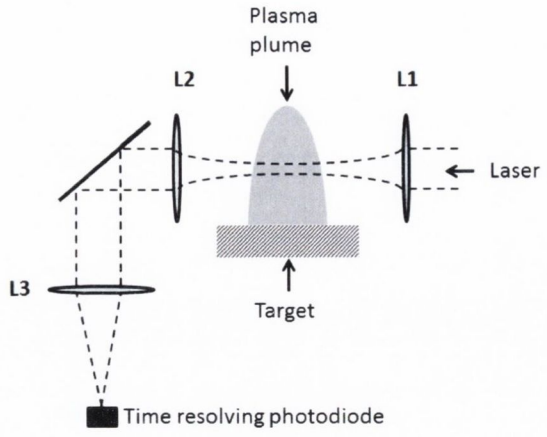

Figure 3.14: Simplified diagram for time-resolved single-wavelength optical absorption measurements.

The probe beam was a 532 nm, 3 mW continuous wave laser with a diameter of 1 mm. The beam was expanded to 6 mm using a 30 cm and 5 cm focal length lenses (not shown on diagram), arranged so that the resultant beam was collimated. The laser beam was then focused using a 30 cm lens, $L1$, with the plasma plane at the focus of the lens. As the laser travels through the plasma, it will see a refractive index variation perpendicular to the target surface axis due to density variation within the plume which will cause a small deflection of the probe beam. Measurements of the beam deflection and its use of a method to characterise laser ablation plasma plume expansion has been carried out previously by numerous authors [72–74]. The output optical system has been designed so that the first collection lens, $L2$, will collimate the probe laser beam. As long as the deflected probe beam is collected by the lens entrance aperture the output beam will exit parallel to the optical axis. The photodiode is positioned at the focus of the lens $L3$ to ensure all the incident beam is collected by the photodiode and any spatial deflection in the probe beam position will result on the ray been focused on the same position on the photodiode. This imaging system ensures that as long as the beam is collected by $L2$ any loss of signal detected on the photodiode is due to absorption or scattering of the laser pulse and not caused by a change in position of the laser spot on the photodiode.

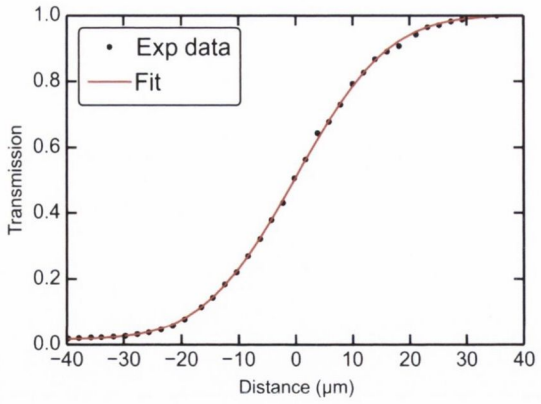

Figure 3.15: Knife edge measurement of probe beam radius at plume position. Fitted with equation 3.14 to give a $1/e^2$ diameter of 50 μm.

To characterise the size of the probe beam at the plume position, the knife-edge method was used to determine the spot size. This is advantageous over using a CCD camera due to the small beam waist and the finite pixel size of the CCD. A sharp edge was placed on a translational stage at the plume position and translated through the probe beam. As the stage was translated the transmitted beam intensity was measured. The radius of the probe beam can be calculated from the variation in voltage measured on the photodiode, shown in figure 3.15 by

$$V = V_{max}\left(1 - erf\left(\frac{x}{w_0}\right)\right) \tag{3.14}$$

where $V(x)$, V_{max}, w_0 are the voltage, max voltage and $1/e^2$ beam diameter where e is Euler's number. The beam waist was found to be $w_0 = 50$ μm.

The transmission of a laser as it travels through an absorbing medium is described by the Beer-Lambert law. From this, the plume transmission can be related to the amount of material by it's density×length product, nL

$$nL(t) = \frac{-ln\,T}{C_{ext}} \tag{3.15}$$

where n is the nanoparticle density, L is the width of the plume at the probe beam position and C_{ext} is the extinction cross-section. The target-probe beam distance was varied to provide spatial resolution and measure the NP plume velocity. Figure 3.16 shows the transmission through a gold nanoparticle plume, recorded with a target substrate

distance of 100 μm. In the case of gold we observe two peaks, the number of observed peaks is material and distance dependent.

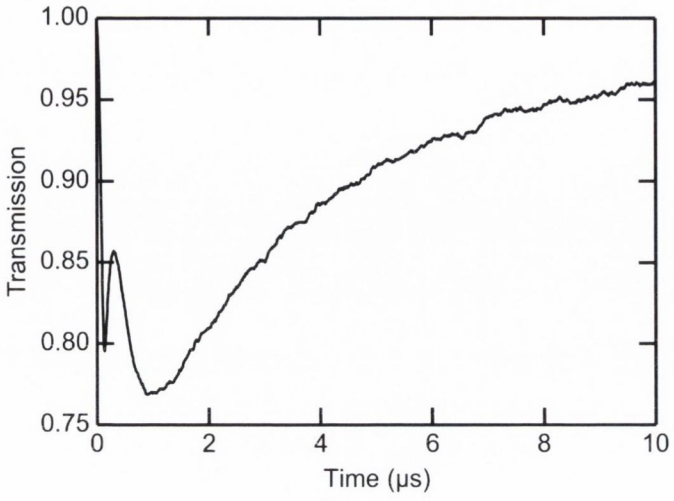

Figure 3.16: Variation in plume transmission versus time at 100 μm from a femtosecond laser ablated gold target.

The length of the plume through which the plume propagates, $L(t)$ is time dependent, as the plume expands the density is reduced but $L(T)$ increases and therefore cannot directly extract a value of n_{np} without knowing information on the shape of the expansion. The extinction cross-section, C_{ext}, is equal to the sum of the absorption and scattering cross-sections. From equation 2.26, the extinction cross-section for a 5 nm gold particle is 7.6×10^{-18} m^2. Applying equation 3.15 to the data presented in fig. 3.16 we obtain the time dependent variation of the density×length product, shown in fig. 3.17.

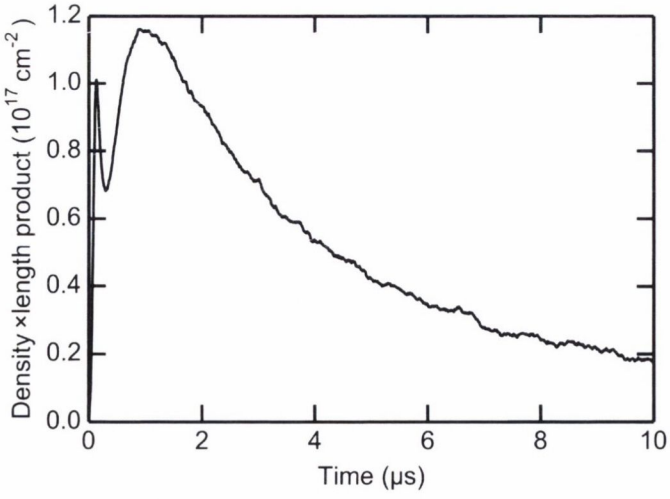

Figure 3.17: Variation in density×length product versus time at 100 μm from a femtosecond laser ablated gold target.

3.5 Film thickness estimation

To study the angular distribution and total amount of ablated material the ablation plume was deposited on a large planar acetate substrate. From this, the deposited film thickness distribution can be obtained (see fig. 3.18). The space resolved optical transmission of the film was measured using a calibrated flat bed scanner (Epson Perfection V700 Photo). A large number of shots were used so that the initially formed nanoparticles coalesced into a thin film so that the transmission through the substrate can be approximated by the bulk optical properties of the material. This was verified using UV-Vis measurements and comparing the shape of the absorption with bulk absorptivity data.

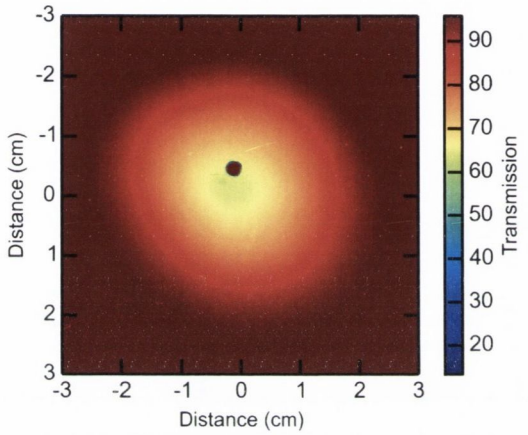

Figure 3.18: Angular deposition of gold femtosecond ablation plume. Deposited with a target-substrate distance of 6 cm and 12,500 laser shots.

Figure 3.19 shows the formalism used in the analysis of the depositions. The scanner was used to measure the transmission of the coated substrate, T_T, and the transmission through the bare substrate, T_G. The substrate is assumed to be non absorbing and the transmission loss through the substrate is due to the reflection at each interface, T_B where $T_G = T_B^2$. The total transmission was normalised to the transmission through the bare substrate

$$T = \frac{T_T}{\sqrt{T_G}} = \frac{T_f T_B}{T_B^2} = \frac{T_f}{T_B} \tag{3.16}$$

The scanned image measures the transmission in three components, Red (R), green (G) and blue (B). The green component is extracted using an algorithm developed in Python. A calibration curve was measured using neutral density filters to relate the scanner counts to transmission at ≈520 nm, T_T, shown in fig. 3.20.

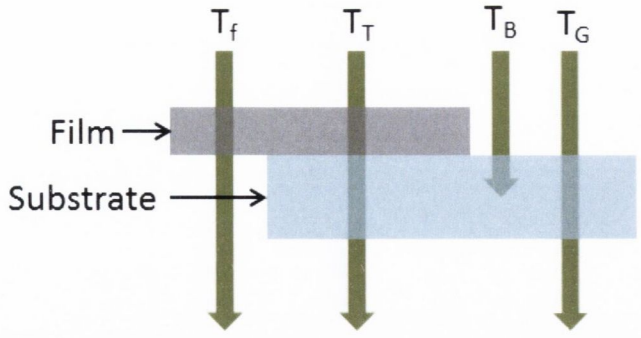

Figure 3.19: Schematic of a coated substrate. In this figure the formalism for the deposition analysis indicated.

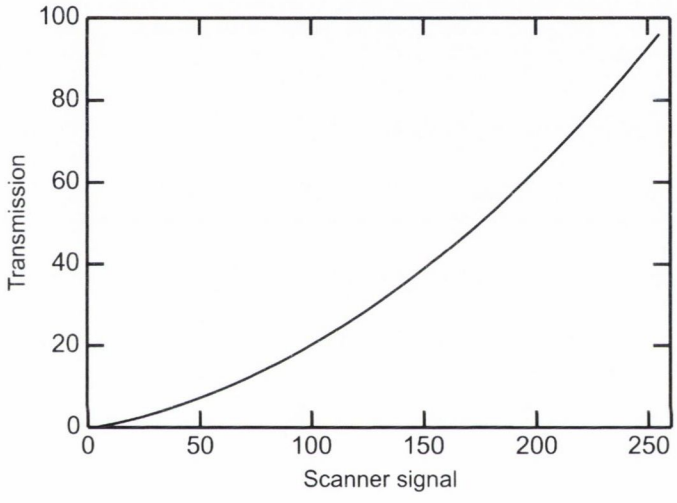

Figure 3.20: Calibration curve to convert from scanner signal to transmission through the substrate, T_f.

A computer program, IMD/XOP, using bulk optical properties, was used to calculate the optical properties of a thin metal film to generate a normalised thickness-transmission relation, T, shown in fig. 3.21. Using this data to calibrate 2D scanner images of the deposition results in a 2D thickness distribution map, from which the shape of the deposition and by integrating, the total amount of material can be estimated.

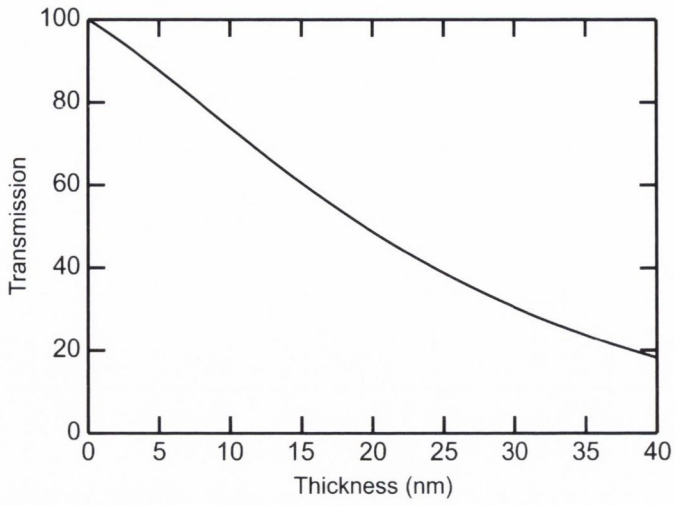

Figure 3.21: Calculated film thickness for gold versus scanner transmission.

3.6 White light interferometry

White light interferometry (WLI) is a non-contact optical surface profiling method. It generates a 3D surface map which is ideal for ablation crater analysis. It offers nanoscale depth resolution. Multiple laser pulses are used to generate a crater with depth on the micrometer range in order to get an accurate, average value for the amount of material ablated per pulse. In order to achieve this level of accuracy WLI interferes two waves, one whose light path is through a reference arm of the WLI and the second which is reflected back off the sample. The depth can be accurately determined by the phase difference between the two wave fronts when recombined on the detector. This is the basic principle on which most interferometers work. An example WLI image is shown in fig. 3.22. The crater was formed by ablating gold with an 800 nm, 130 fs laser with a peak fluence of $1.6\,\mathrm{J\,cm^{-2}}$.

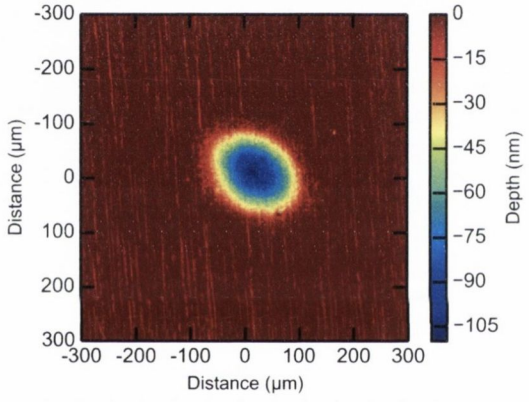

Figure 3.22: Gold ablation crater image recorded using white light interferometry. Crater depth is given in per laser shot.

Chapter 4

Femtosecond laser ablation and deposition

This thesis focuses on characterising femtosecond laser ablated material. To achieve this a number of diagnostic methods have been employed to perform a detailed characterisation of the ablated material. This chapter will consider the experimental parameters, the material removed during ablation and the nature of material deposited on substrates. Initially, we will discuss the experimental and diagnostic setups that were designed to study the ablation plumes discussed in the next few chapters. Our discussion is focused on four materials; gold, silver, aluminium and tin. White light interferometry, discussed in section 3.6, was used to quantify the amount of material ablated and the ablation crater dimensions. The ablation crater dimensions facilitate an estimation of the initial plume dimensions which serves as a good starting point for modelling the hydrodynamic plume expansion. In later chapters, for characterising each plume component emission and absorption techniques were employed. The analysis of which was expanded beyond current descriptions by accounting for the nanoparticle temperature dependent emissivity. In this work we assume a small average particle size such that the Rayleigh approximation to Mie theory is applicable. The validity of this will be discussed by measuring the nanoparticle size using electron microscopy.

Figure 4.1 shows the configuration of the various diagnostic methods setup specifically for the work contained in this thesis. ICCD and time- and space- resolved emission spectroscopy were recorded parallel to the target surface, with the axis of plasma flow imaged onto the spectrometer slit. A 532 nm, 3.5 mW continuous wave diode laser, aligned parallel to the target surface was used for time resolved single wavelength absorption of the nanoparticle plume. The Langmuir ion probe, with dimensions of 2.1×4.5 mm was positioned at 3 cm from the target and rotated about the laser spot.

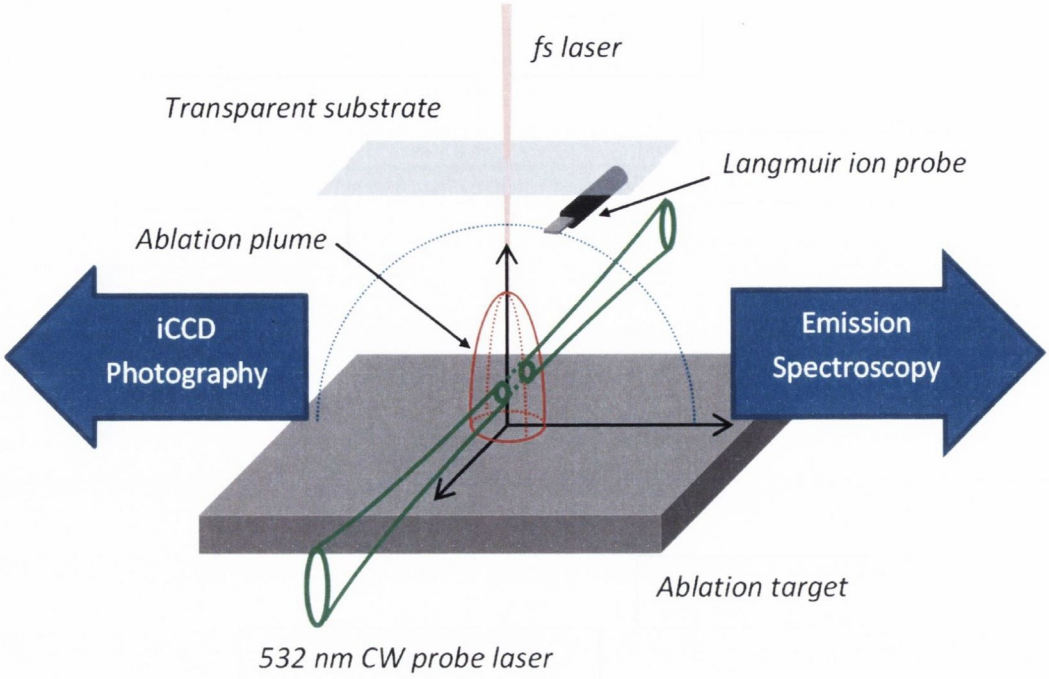

Figure 4.1: Experimental setup showing configuration of diagnostic techniques.

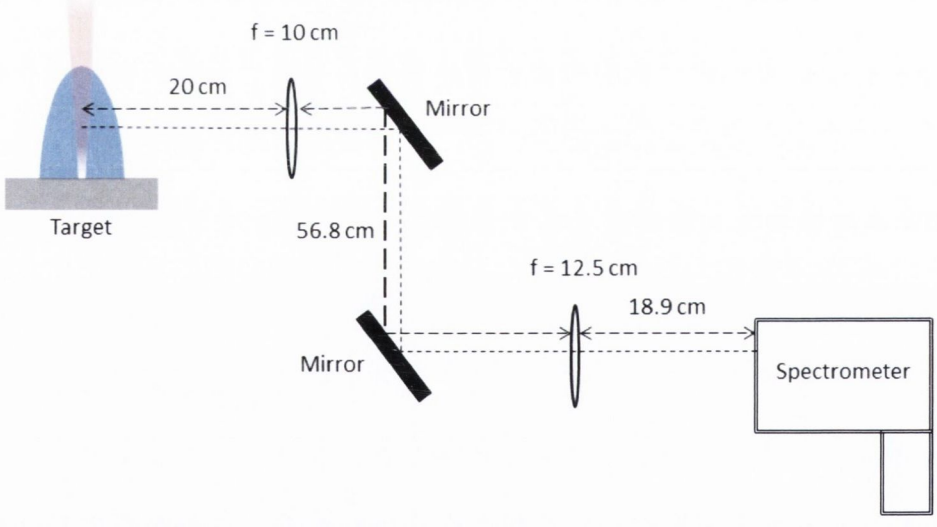

Figure 4.2: Schematic diagram showing the spectrometer imaging system.

Figure 4.2 shows a simplified diagram of the spectrometer and its optical imaging system. Unlike the setup described in section 3.2, two achromatic lenses were used in this imaging system. Achromatic lenses limit the effect of chromatic aberration. The plume was imaged onto the spectrometer slit with a magnification of 0.51. The acceptance solid angle of the imaging system was calculated and found to be 3.4×10^{-3} sr. The spatial dimension was calibrated by imaging a wire mesh of known dimensions placed

at the plume position onto the spectrometer and found to be 56.8 px/mm. The spatial resolution of the system was determined by taking a line profile across the edge of the image of the wire and found to be ≈65 μm. The spectral resolution of the spectrometer, equipped with a 300 l/mm grating, was measured using a low density mercury lamp and found to be 0.8 nm at a wavelength of 436 nm to give a resolving power, $\lambda/\Delta\lambda$ = 550. Multiple grating positions were used to cover a wide spectral range. ICCD and spectroscopy images were background corrected so that only plume emission was taken into account.

The ablating laser beam was focused using a 30 cm biconvex lens with a lens-target distance of 26 cm. The beam profile on the target, shown in fig. 4.3, was recorded using a Coherent LaserCam-HR camera. In order to reduce the intensity of the laser beam incident on the camera while ensuring the spatial profile remained unchanged two glass wedges were used. The beam profile along its shortest and longest axis was fitted with a Gaussian (fig. 4.3b). The focused spot was found to be slightly elliptical with $1/e^2$ diameter of 360 and 330 μm. The energy incident on the target was 0.55 mJ producing a peak fluence of 1.6 J cm^{-2}.

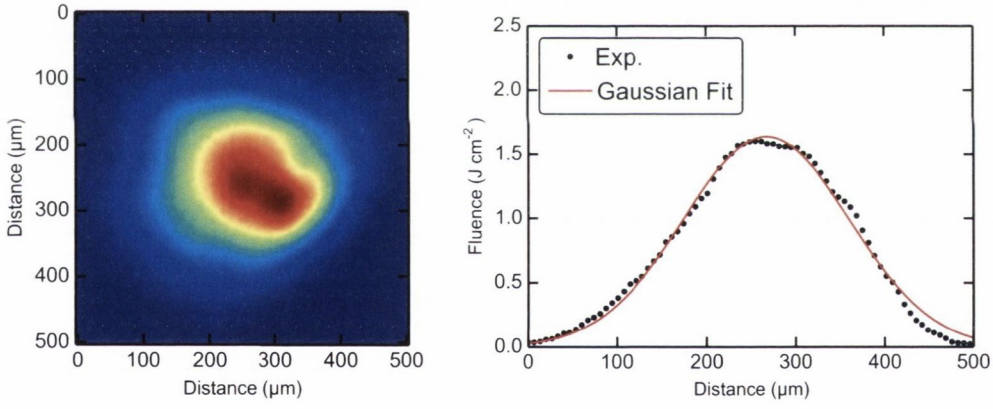

(a) **(b)**

Figure 4.3: CCD image of of laser pulse spatial profile and (b) 1-D line out showing fluence spatial distribution at target position.

4.1 Crater analysis

The ablation spot was analysed using white light interferometry to determine the initial shape of the plasma and to estimate total material removed. An ablation crater was produced by stopping the target translation stage and firing the laser pulse at the same position on the target. Figure 4.4a shows the ablation crater for gold generated using 50 laser shots. The crater was slightly elliptical with dimensions of $180 \times 220\,\mu m$. The total number of atoms ablated per pulse was 7.4×10^{13} (2.5×10^{-11} kg). As shown in fig. 4.4, this method was repeated for silver, aluminium and tin with 100, 100 and 50 laser shots respectively. The number of atoms ablated per pulse and crater dimensions are given in table 4.1. For each material, two craters were formed to estimate the error in this measurement and found to be <10%. In fig. 4.4d, the ablation crater of tin is distinctively different than the rest of the materials. This has been observed previously and is possibly due to the low melting point of tin.

Table 4.1: White light interferometry analysis of ablation craters for gold, silver, aluminium and tin.

	Gold	Silver	Aluminium	Tin
Atoms ablated	7.4×10^{13}	3.9×10^{13}	6.4×10^{13}	1.2×10^{14}
Mass ablated	2.5×10^{-11} kg	6.6×10^{-12} kg	2.9×10^{-12} kg	2.36×10^{-11} kg
Crater dimensions	$180 \times 220\,\mu m$	$140 \times 170\,\mu m$	$200 \times 260\,\mu m$	$290 \times 370\,\mu m$

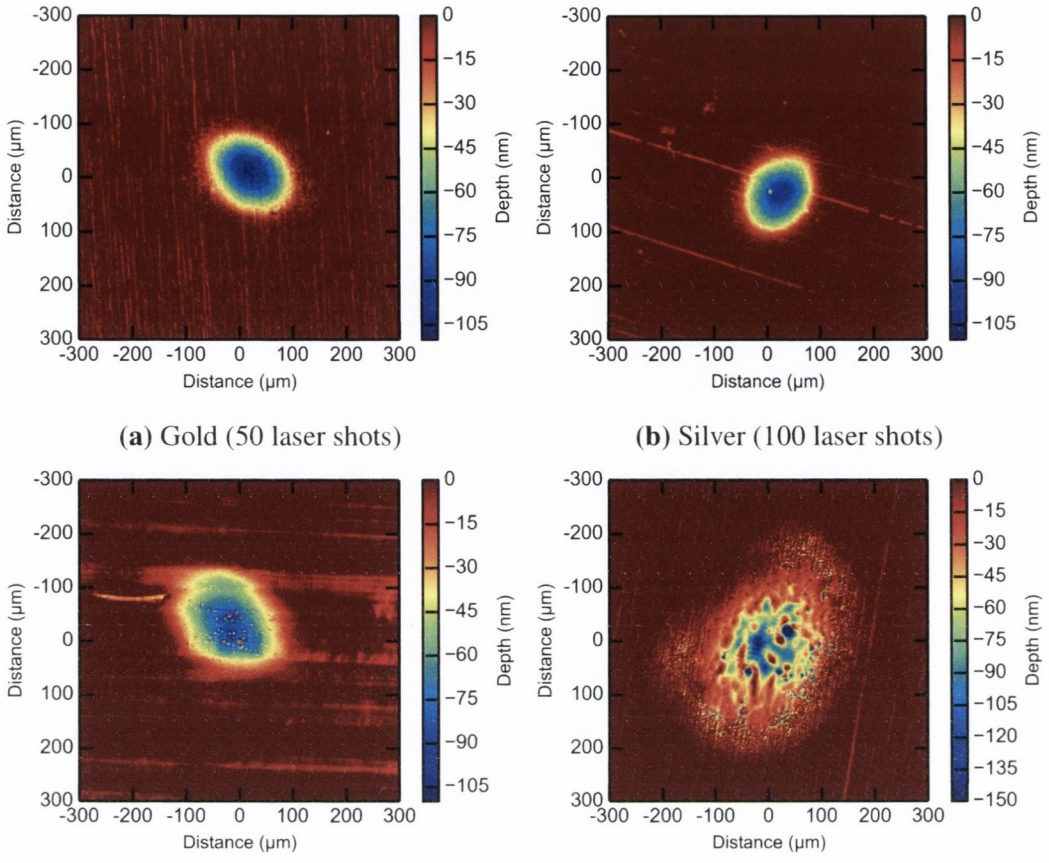

(a) Gold (50 laser shots)

(b) Silver (100 laser shots)

(c) Aluminium (100 laser shots)

(d) Tin (50 laser shots)

Figure 4.4: White light interferometry analysis of ablation craters made in; (a) gold, (b) silver, (c) aluminium and (d) tin. Crater depth (in nm) shown per laser pulse.

4.2 STEM depositions

The nanoparticle size plays an important role in its optical response. If a nanoparticle satisfies the size parameter such that $2\pi a << \lambda$ the Rayleigh approximation to Mie theory can be applied, the absorption and scattering cross-sections of a nanoparticle are given by equations 2.26 and 2.27. As $C_{abs} \propto a^3$ and $C_{scatt} \propto a^6$ the nanoparticle size determines the dominant extinction mechanism. In order to measure the nanoparticle size distribution, depositions were carried out on a carbon coated transmission electron microscope (TEM) grid. The grid was placed in the chamber at 6 cm from the target. A low number of shots (600) were used to ensure the particles on the grid were well separated with a low probability of overlap. The nanoparticles were imaged with a scanning transmission electron microscope (STEM). Post processing analysis was carried out using statistical counting to obtain the size distribution. Figure 4.5 a, c, e, g shows the depositions of gold, silver, aluminium and tin respectively. For each material the nanoparticles are well separated. The corresponding size distribution for each material are also shown in fig. 4.5 fitted with a log-normal distribution. The average particle Feret diameter was between 9.5 nm for gold and tin to 16 nm for aluminium. The Feret diameter is defined as the width of a particle measured along its widest dimension. For particles of this size, as discussed in section 2.4, absorption is the dominant extinction mechanism.

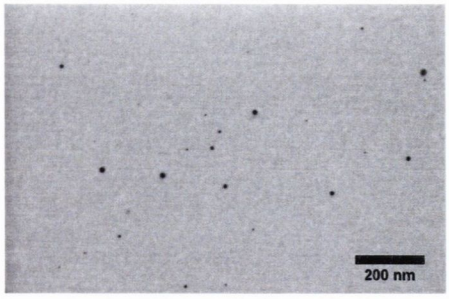

(a) Gold STEM image

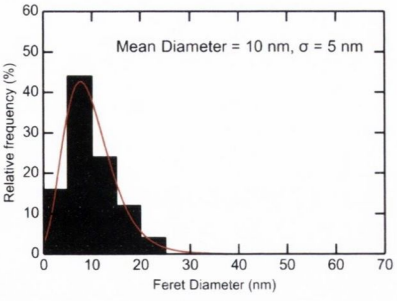

(b) Gold size distribution

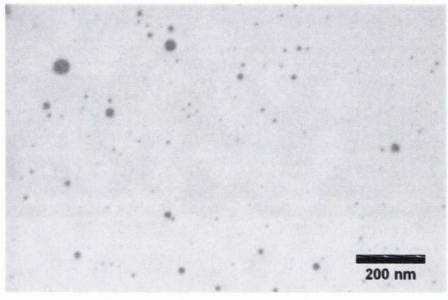

(c) Silver STEM image

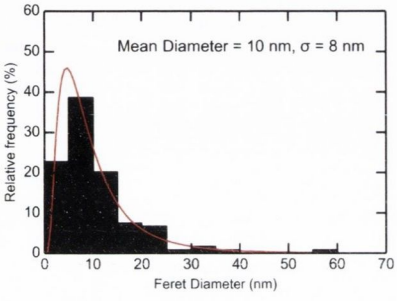

(d) Silver size distribution

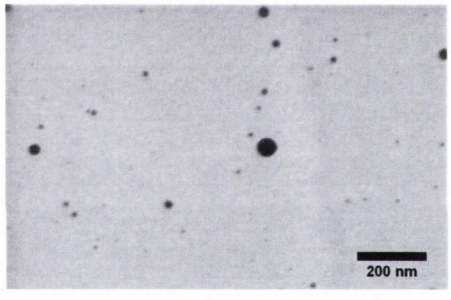

(e) Aluminium STEM image

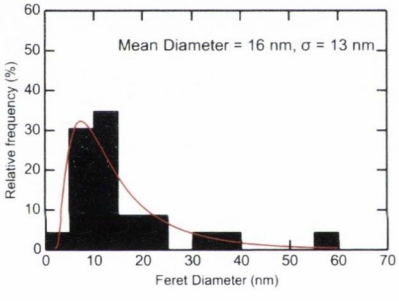

(f) Aluminium size distribution

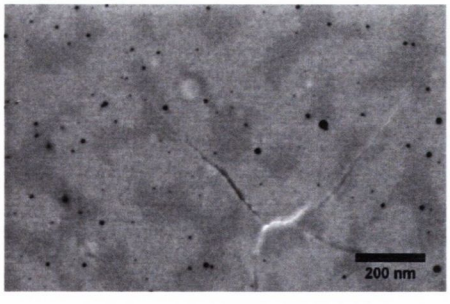

(g) Tin STEM image

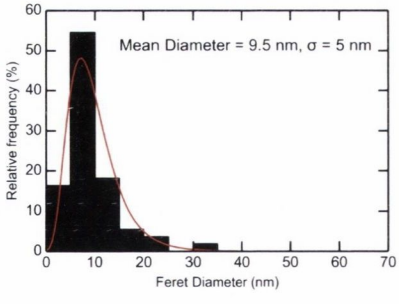

(h) Tin size distribution

Figure 4.5: STEM images a, c, e, g and corresponding Feret diameter distributions b, d, f, h of gold, silver, aluminium and tin nanoparticle films produced using 600 laser shots. {σ is the Feret diameter standard deviation.

4.3 Angular distribution of deposition

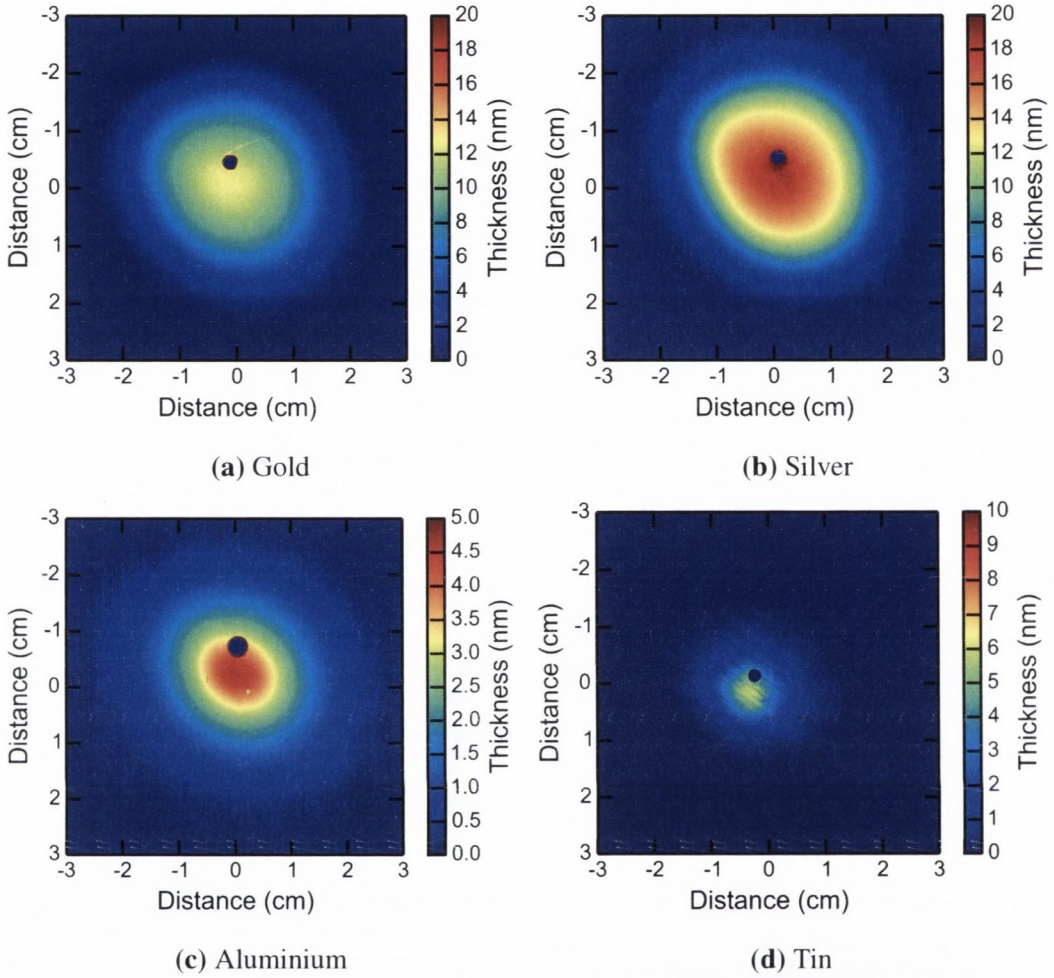

(a) Gold **(b)** Silver

(c) Aluminium **(d)** Tin

Figure 4.6: Depositions of a. gold (12,500 shots), b. silver (12,500 shots), c. aluminium (10,000 shots), and d. tin (5,000 shots) on planar substrates and analysed as described in section 3.5.

Large area depositions provide a measure of the total amount of material deposited. The film thickness was chosen such that the transmission through the film was appreciable, but not opaque. The film should be thick enough so that a continuous film is formed so that the film exhibits bulk optical properties. The transmission through the film was measured in the green spectral region ($\approx$ 515 nm). The calibration procedure to estimate the thickness of the film as a function of transmission and calculate the total amount of material is described in more detail in section 3.5. Figure 4.6 shows the spatial variation of the thickness distribution for each material. Integrating over the total deposition the total number of atoms deposited was found, for gold, to be 3.7×10^{13} per pulse. The total deposited material for each metal is listed in table 4.2.

4.4 Conclusions

To characterise each plume component in detail, we designed the experimental setup to be composed of multiple diagnostic methods which we introduced in this chapter. The laser beam profile at the target position was accurately measured using a CCD based beam profiler. From this, the peak fluence was found to be $1.6\,\mathrm{J\,cm^{-2}}$.

Low shot number depositions on carbon coated TEM grids were used to estimate the size of nanoparticles produced in the ablation of each material. Each material had a mean Feret diameter below 20 nm. In this size regime, the Rayleigh approximation to Mie theory applies and the absorption and scattering cross-sections of the particles are described by equations 2.26 and 2.27.

Table 4.2: Material inventory for fs ablation of different materials.

	Gold	Silver	Aluminium	Tin
Atoms ablated	7.4×10^{13}	3.9×10^{13}	6.4×10^{13}	1.2×10^{14}
Atoms deposited	3.7×10^{13}	5.7×10^{13}	1.4×10^{13}	6.7×10^{13}

Table 4.2 shows the variation in material ablated and deposited for each material. There is a discrepancy in the case of silver, which implies that more material is deposited than ablated. The thick depositions were analysed using UV-Vis spectrophotometry and no surface plasmon resonance peak was detected. We are assuming for the calibration procedure that the film is continuous and can be treated as a bulk film. For thick depositions, using nanosecond laser ablation, a thin, uniform film can be formed. It is unclear whether this is the case for thick films produced by femtosecond laser ablation. This is outside the scope of this work, however, it does warrant further investigation. Figure 4.6 shows the variation of thickness distribution. Towards the edge of the film we see the estimated film thickness decrease below 5 nm. Previous studies have shown that films of this thickness are not continuous and exhibit nanoparticle optical properties [75]. Therefore, it is possibly that surface plasmon effects will cause an over estimation of the amount of material towards the edge of the depositions.

Chapter 5

Femtosecond atomic plume

In this chapter we will focus on the properties of the atomic plume produced by femtosecond laser ablation of metals. There have been numerous studies focused on different aspects of the atomic plume [18, 75, 76]. Toftmann et al. compared silver ablation plumes produced with UV femtosecond and nanosecond lasers [76]. Their work describes the use of angular Langmuir probe and deposition measurements to characterise the ablated material. Consistent with our work, their Langmuir ion probe measurements show a fast contamination peak which they analyse using an ion energy analyser to show that it is due to hydrogen and carbon/oxygen. The resolution of their system was such that they were unable to distinguish between carbon and oxygen atoms. They found that the energy efficiency of fs laser ablation is $\approx$10 times higher than ns ablation. Amoruso et al. studied the femtosecond laser ablation of nickel and compared with molecular dynamic simulations [18]. They primarily used time- and space- resolved spectroscopy and iCCD imaging for their study. From this, they clearly resolved two plume components, the origin of which is described in more detail in section 3.4. They verify the state of the material in each plume component using spectroscopy, which, for the fast component shows discrete line emission characteristic of atomic bound-bound electronic transitions. By comparing with molecular dynamic simulations they were able to study the thermodynamic trajectories the material undergoes at different depths within the target responsible for the formation of the two distinct plumes components. It is also worth noting that, as has been reported previously, femtosecond laser ablated material has a much lower ion fraction than for nanosecond ablation due to the absence of laser-plume interactions. Mirza et. al. showed that for the ablation of silver, the nanosecond plume is nearly fully ionized while for femtosecond ablation the ion fraction is $\approx$ 1% [75].

For our study, we aim to combine multiple diagnostic techniques to give a detailed description of the plasma plume. A detailed description of the setup is given in chapter 4. A rotational Langmuir ion probe was used to measure the angular distribution of ions, ion yield of the ablated material, and the ion energy and velocity distributions.

The shape and constituents of the plume will be be studied using iCCD imaging and time- and space- resolved spectroscopy measurements. A detailed analysis of the silver atomic plume will be presented by modelling the emission spectra using the spectral synthesis code PrismSPECT. From this, we can estimate the plume temperature, thickness and density. It also allows us to output the plasma ion fraction and atomic level populations. Combining this analysis with plume shape information measured from iCCD images we devised a method to estimate the total amount of atoms in the plasma plume. The electron density will be independently studied using using Stark broadening measurements.

5.1 Langmuir ion probe

The ionic component of the fast, plasma plume was characterised using a Langmuir ion probe, biased at -25V, as described in more detail in section 3.3. Figure 5.1 shows gold ion signals as a function of angle recorded for the experimental conditions described in chapter 4. We observe the expected decrease in the ion signal and increase in peak time of flight versus angle, as observed by Toftmann et al. [76], Doggett et al. [46] and described by the Anisimov model [20, 21]. We observe two components, an initial fast peak and a slower main component. By ablating the same point on the target at 1 Hz, the contamination peak amplitude reduced to a minimum value of approximately 10% of the main peak amplitude. The ratio between the component intensities changes with angle as a result of each component having a different aspect ratio. The exact composition of the fast peak has yet to be determined but it has been suggested that it is due to low Z contamination of the target surface [47]. This could be verified by a short experiment and would be of interest for future work using an electrostatic analyser to measure the charge to mass ratio, and hence determine the species in the plume. The ion fluence at a given angle was found by integrating the ion flux in time. The initial contamination peak was discarded and the ion flux was integrated under the main plume component shown in fig. 5.1a. The plume aspect ratio, k, can be found by fitted the angular ion fluence with

$$F = F(0)\left(\frac{1 + tan^2(\theta)}{1 + k^2 tan^2(\theta)}\right)^{3/2} \tag{5.1}$$

where $F(0)$ is the ion fluence normal to the target. The total number of ions in the plasma was calculated using equation 3.13. For gold, the total number of ions was 4×10^{11}

±15%. Figure 5.2 shows the ion signals and corresponding ion angular distributions for aluminium, silver and tin. In each case, the peak of the fitting angular ion fluence distribution was positioned at 0 degrees to account for any misalignment of the probe to the laser spot. From this, the total number of ions for silver, aluminium and tin was found to be 7.5×10^{11}, 4×10^{11} and 3×10^{11} respectively.

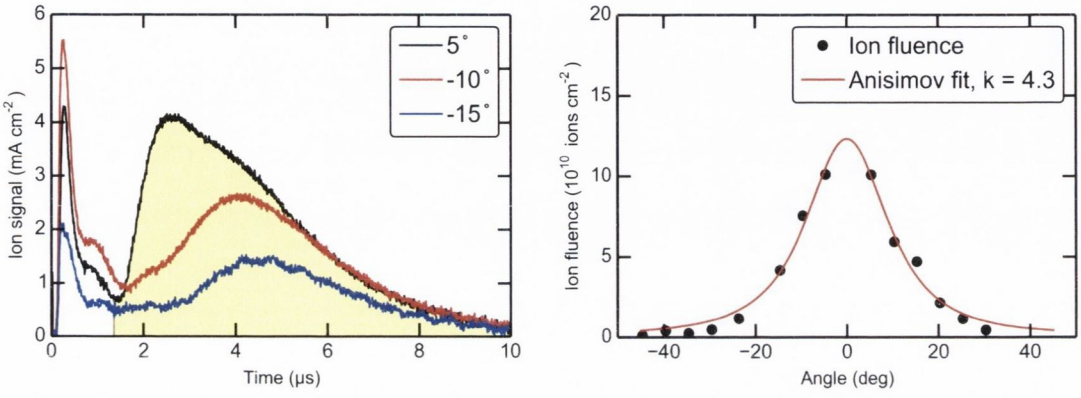

(a) Angular probe measurements **(b)** Ion fluence as a function of angle

Figure 5.1: Langmuir ion probe analysis of femtosecond gold atomic plume, with a target-probe distance of 3 cm. (a) The variation of ion signal at different angles and (b) integrated ion yield versus angle.

From the measured ion time of flight signals, the ion energy distributions were derived using equation 3.11 and are shown in fig. 5.3. The average ion energy for each material is indicated on their respective graphs and it can be seen that the ion energies range up to a few hundred eV.

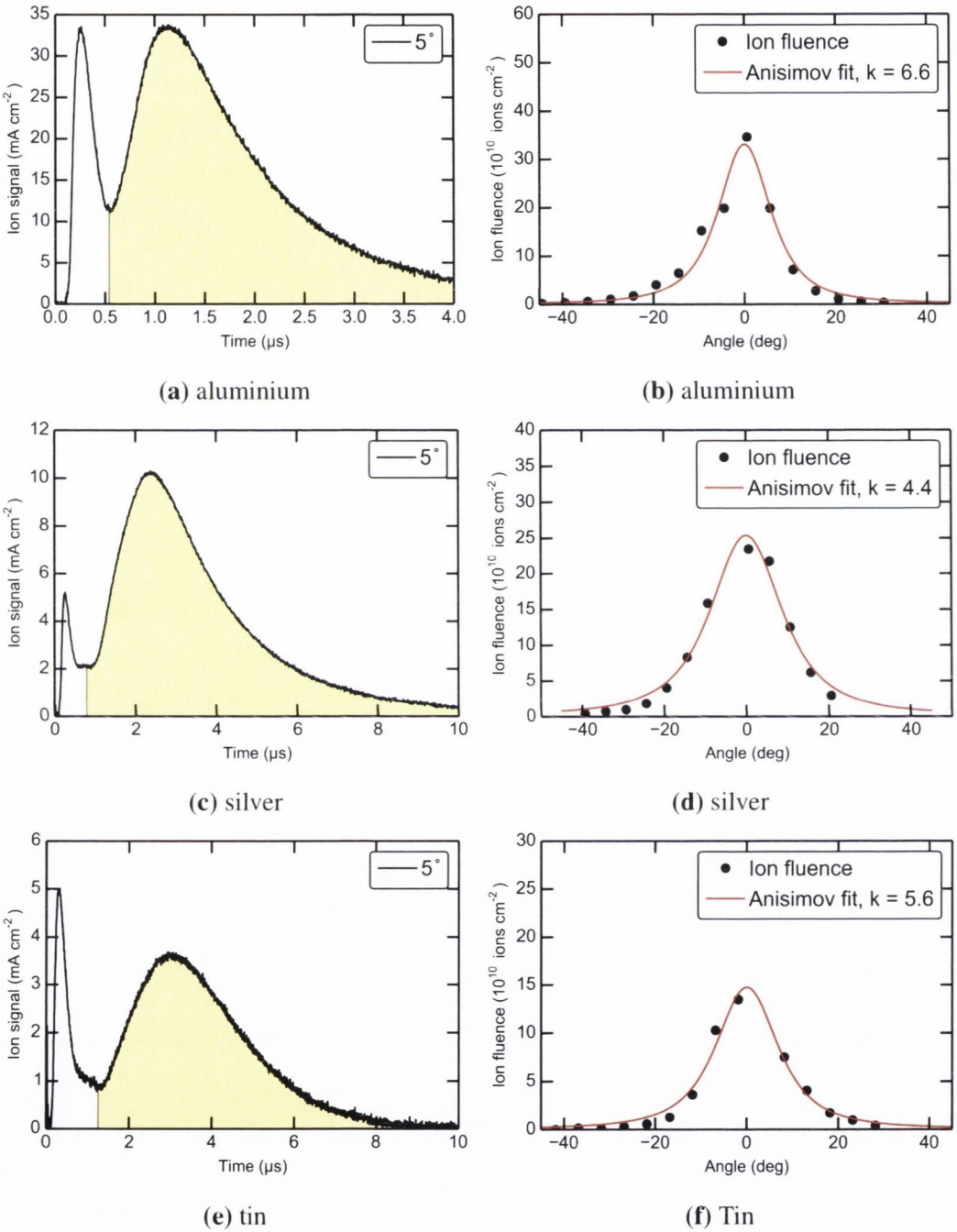

(a) aluminium **(b)** aluminium

(c) silver **(d)** silver

(e) tin **(f)** Tin

Figure 5.2: Comparison of ion probe time of flight signals and ion angular distributions for (a)-(b) aluminium, (c)-(d) silver and (e)-(f) tin.

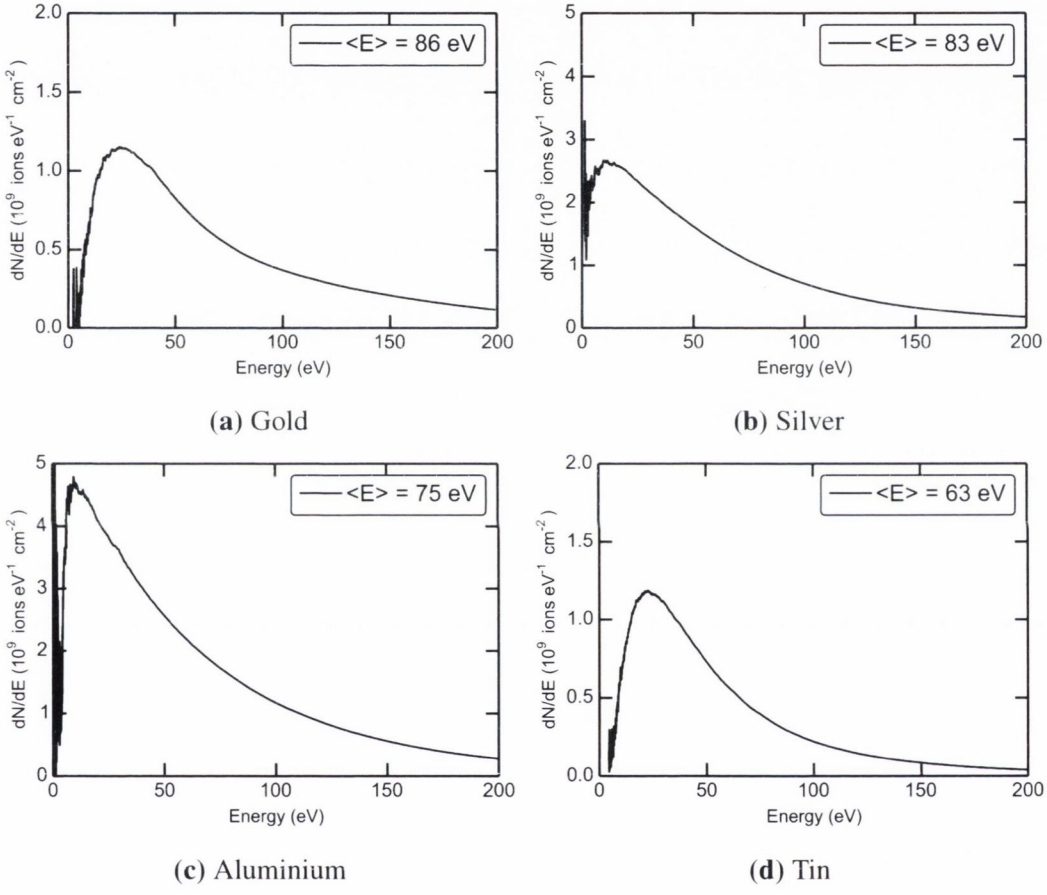

(a) Gold **(b)** Silver

(c) Aluminium **(d)** Tin

Figure 5.3: Ion energy distributions for (a) gold, (b) silver, (c) aluminium and (d) tin.

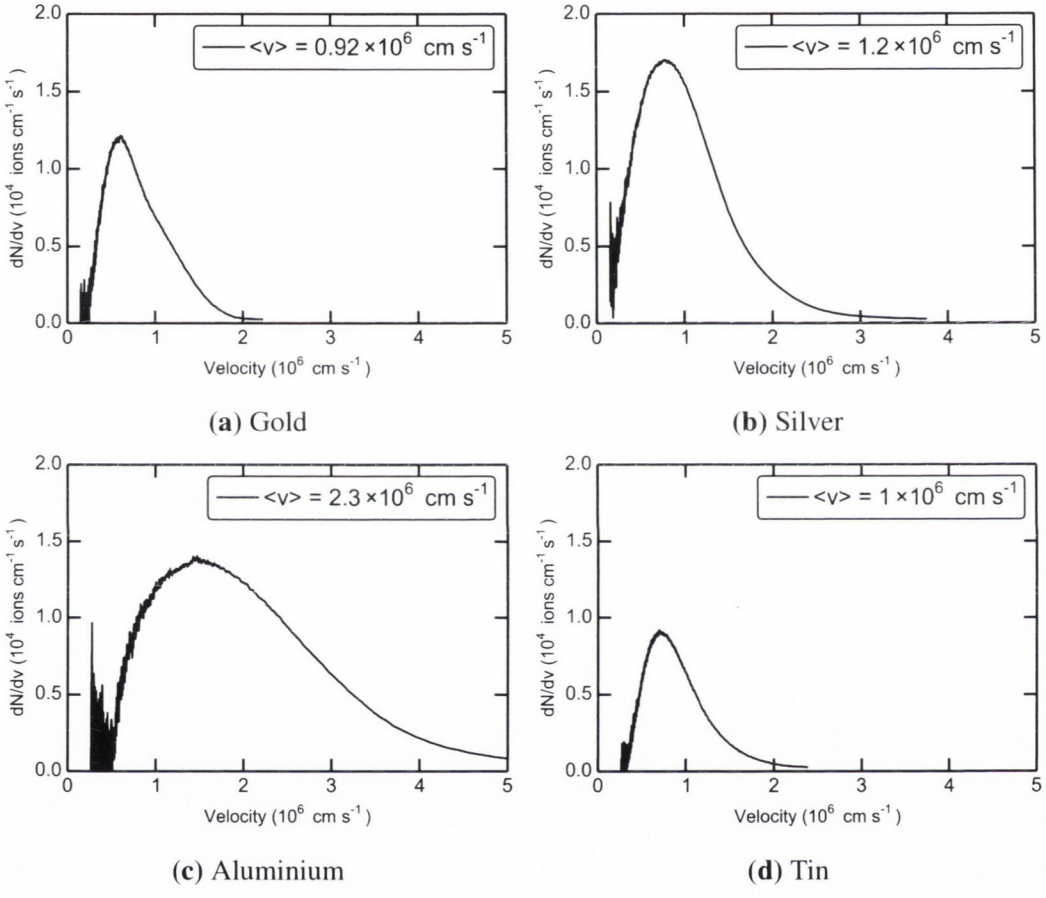

Figure 5.4: Ion velocity distributions for (a) gold, (b) silver, (c) aluminium and (d) tin.

Using equation 3.10, the ion velocity distributions were calculated from the probe signals. The velocity distribution for each material are compared in fig. 5.4. As expected, the lighter elements have a higher velocity, detailed in table 5.1.

For each material a Langmuir probe study was conducted at late times and no evidence of charged nanoparticles was observed.

Table 5.1: Ion plume parameters for various materials.

Material	Aspect ratio (k_{xz})	Total ions $\times 10^{11}$ atoms	Avg. ion energy eV	Avg. velocity $\times 10^{6}$ cm s^{-1}
Gold	4.3	4 ± 6	73	0.92
Silver	4.4	7.5 ± 1.1	83	1.2
Aluminium	6.6	4.0 ± 0.4	75	2.3
Tin	5.6	3.0 ± 0.5	63	1

5.2 ICCD imaging

Figure 5.5 shows some examples of time-resolved iCCD images for gold at different time delays. Each plume component can be seen to expand in a forward directed expansion. The position of maximum emission of the plasma plume can be seen to disconnect from the target and propagate away. The nanoparticle plume remains connected to the target with its peak emission remaining close, but not at the target surface. The Anisimov model predicts the maximum particle density located at the target surface. Doggett et. al. has shown previously that for a nanosecond laser ablated silver target, the atomic plume produced undergoes an Anisimov-like expansion [46].

Figure 5.6 shows lineouts of some of the images in fig. 5.5, taken along the central axis of the plume in the z–direction. Early in time, at 50 ns and 100 ns, we see both plume components clearly resolved and separated in space. The atomic plume has a smaller aspect ratio and a much higher velocity (shown in fig. 5.6b). Therefore, its signal reduces at a much faster rate; beyond 500 ns the atomic plume is no longer observable. Figure 5.6a shows the velocity fit for the atomic plume front which has a velocity of $(0.80 \pm 0.03) \times 10^{6}$ cm s^{-1}, the nanoparticle plume front is approximately 50 times slower with a velocity of $(1.5 \pm 0.1) \times 10^{4}$ cm s^{-1}. The plume front position was approximated as the point at which the counts are 10% of their peak value.

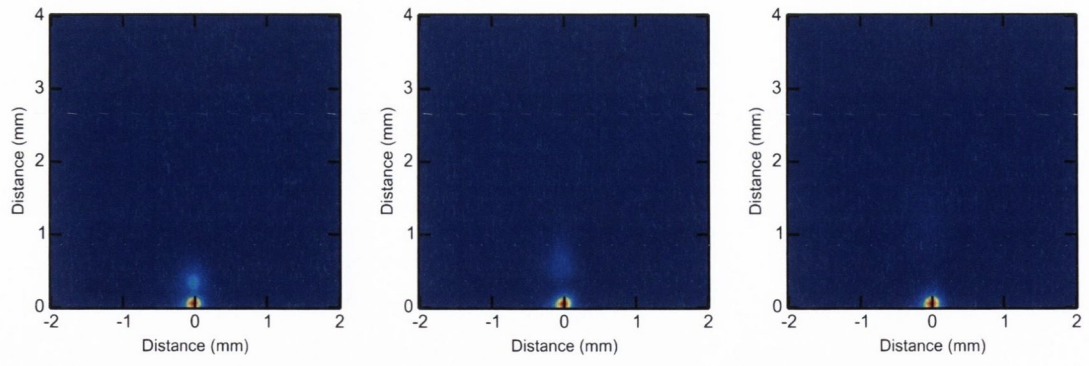

(a) 50 ns **(b)** 100 ns **(c)** 200 ns

(d) 500 ns **(e)** 800 ns **(f)** 5 μs

Figure 5.5: Time resolved iCCD images showing the evolution of the gold plume expansion.

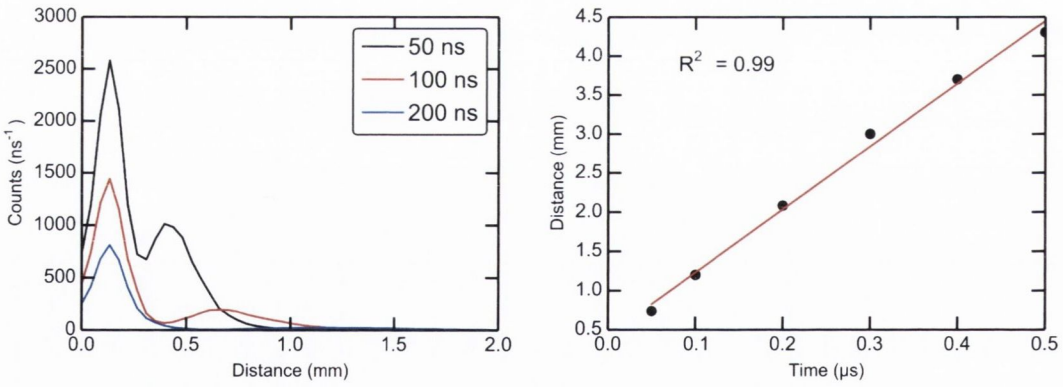

(a) **(b)**

Figure 5.6: (a) Lineouts extracted from gold iCCD imaging at different times and (b) atomic plume front velocity fit. The plume front position was approximated as the point at which the counts are 10% of the peak value.

For each material, table 5.2 shows a comparison of the average ion velocity, measured using a Langmuir ion probe (fig. 5.2) and the plume front velocity measured from iCCD images. The tin plume front velocity is not shown as the atomic plume emission was too weak to measure an accurate velocity. For gold and aluminium, the average velocity

measured using the Langmuir probe is higher than the front velocity measured from iCCD images. However, it is important to note that the Langmuir probe measures the ionic component of the plume. It has been observed previously, using space resolved emission spectroscopy, that the ionic component of the plume can leave the target at a higher velocity than the neutrals (appendix A.1) [77].

Table 5.2: Plume velocities measured with iCCD imaging and a Langmuir ion probe for various materials.

Material	Avg. Velocity Langmuir probe $\times 10^6$ cm s^{-1}	Front Velocity iCCD imaging $\times 10^6$ cm s^{-1}
Gold	0.9	0.80 ± 0.03
Silver	1.2	1.5 ± 0.1
Aluminium	2.3	1.6 ± 0.1
Tin	1	-

ICCD images give a somewhat qualitative description of the plume. The recorded counts are related to the emission of the plasma by the wavelength dependent transmission of the imaging lens, the spectral sensitivity of the iCCD and the camera settings; gain, gate width and number of acquisitions. Due to the spectral response of the iCCD, emission of the same intensity from different spectral regions will produce a different number of counts recorded. However, if we assume the plume is optically thin and in thermodynamic equilibrium we can relate the counts recorded to the number density of atoms in the plume and therefore, describe the relative distribution of plume density. The plume spectral radiance emitted along the optical axis, x, is directly proportional to the intensity incident on the iCCD and hence the counts recorded.

$$L(\lambda, T) = \int J(\lambda, T) n(x, y, z) dx = J(\lambda, T) n_a(y, z) \tag{5.2}$$

where $J(\lambda, T)$ and $n_a(y, z)$ are the spectral density, and areal number density respectively. The areal number density is related to the number density by $n_a(y, z) = \int n(x, y, z) dx$. If we define a normalised density function as

$$n'(x, y, z) = \frac{n(x, y, z)}{N_{pl}} \tag{5.3}$$

where N_{pl} is the total number of atoms in the plume. The normalised density is related to the plasma radiance detected by the iCCD camera by

$$n'_p(y,z) = \frac{L(y,z)}{\int\int L(y,z)dydz} \tag{5.4}$$

where $L(y,z)$, the plasma spectral radiance, is directly proportional to the counts recorded on the iCCD camera, and hence, the normalised plume density can be extracted from the iCCD images. From this, we can relate the plume density, measured using spectroscopy and optical absorption measurements to normal density distribution to estimate the total number of atoms in the plume.

Figure 5.7 shows iCCD imaging of each material at 50 ns, 200 ns and 5 μs. The relative intensity of each of the plumes varies from material to material. The tin atomic plume is barely observable. In contrast for silver, the atomic plume emits strongly and the NP plume is much less intense.

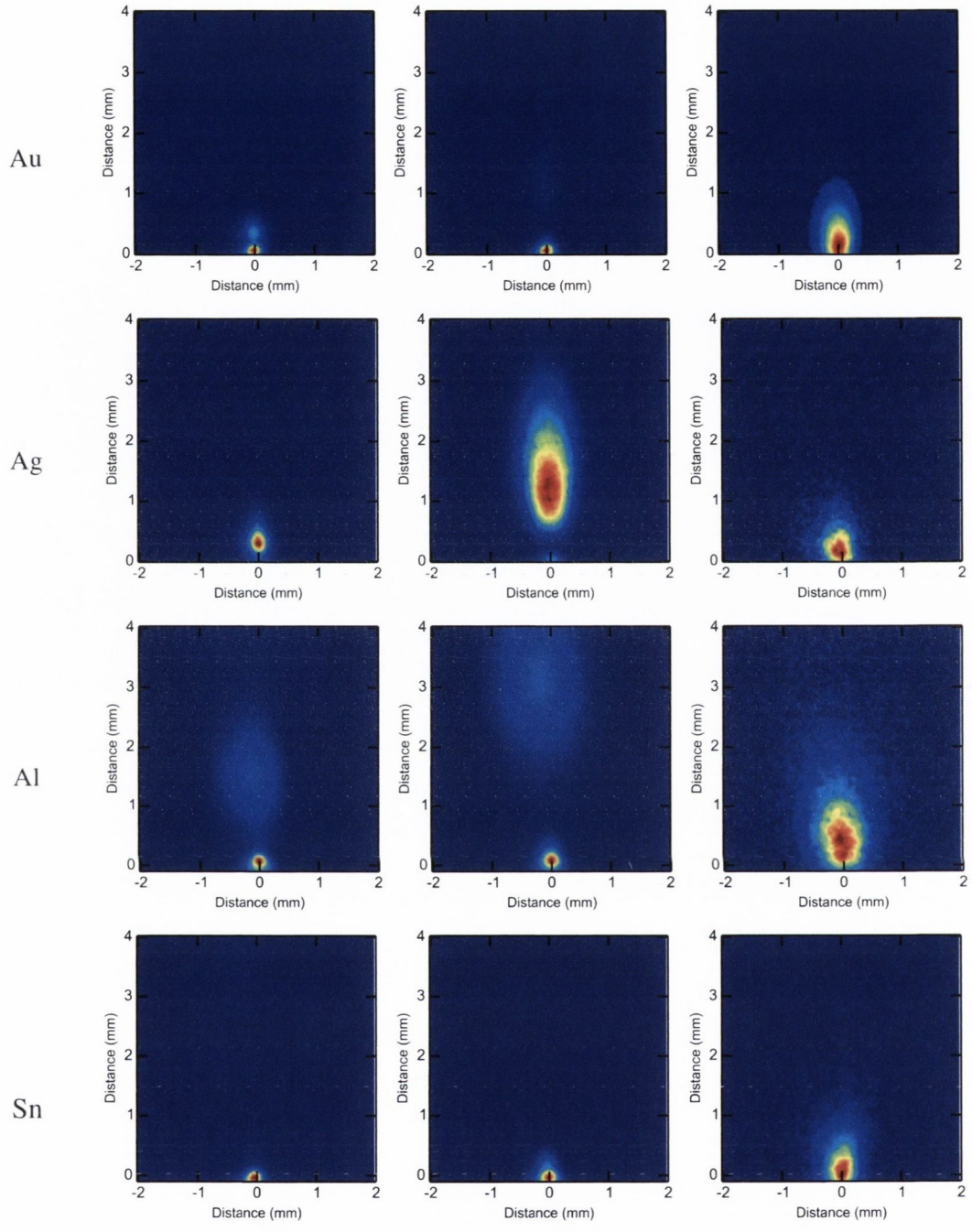

(a) 50 ns **(b)** 200 ns **(c)** 5 μs

Figure 5.7: Time resolved iCCD images showing the evolution of the atomic and nanoparticle plume expansions for gold, silver, aluminium and tin.

5.3 Spectroscopy

Figure 5.8 shows time and space resolved spectra for the ablation of each material at (a) 50 ns, (b) 100 ns and (c) 200 ns after the laser pulse for the experimental conditions described in chapter 4. For each material, a reflection of the plume from the target is observed as emission coming from behind the target position. For gold, both the fast and slow plume components are clearly resolved. The fast component is comprised of well separated discrete lines characteristic of gold atomic emission. As observed with iCCD imaging, the relative intensity of the fast and slow plume components varies from material to material. This suggests a difference in the relative number of atoms in the fast and slow plume components.

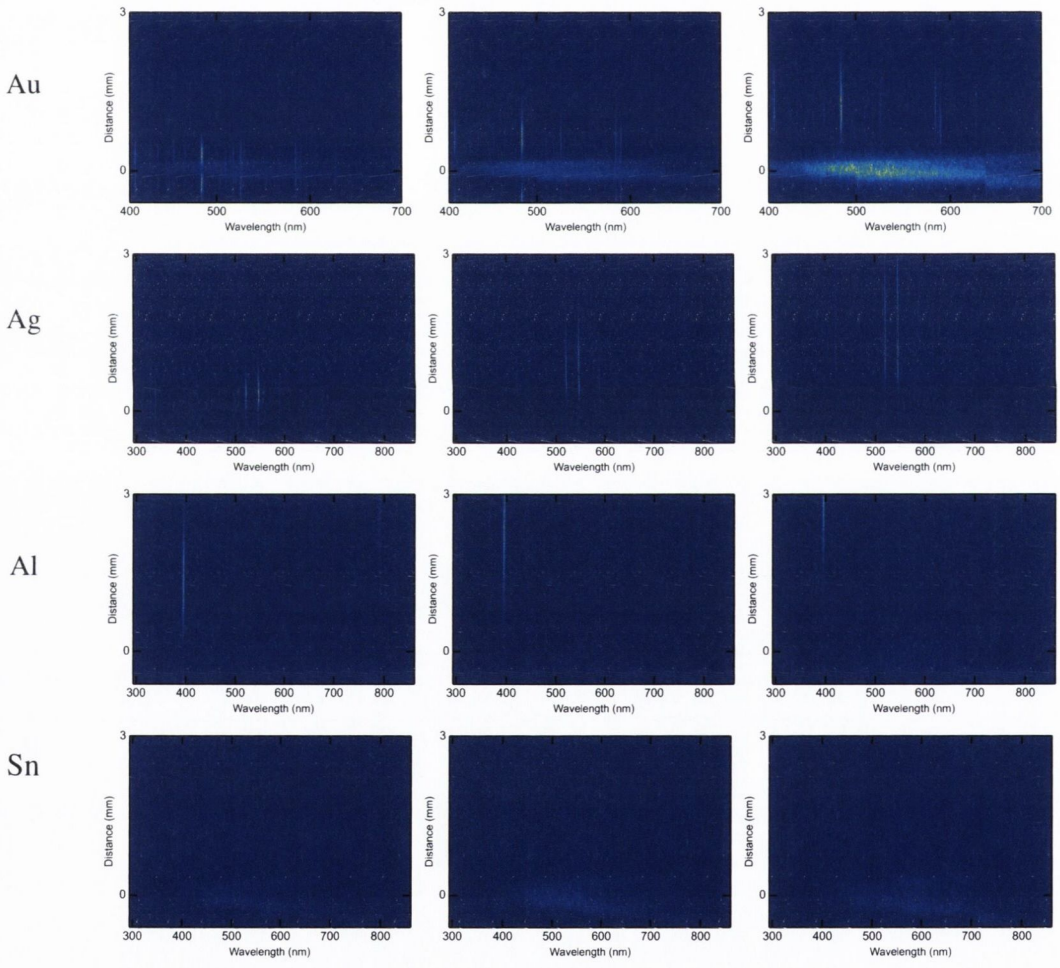

Figure 5.8: Time resolved emission spectra showing the evolution of the atomic and nanoparticle plumes for gold, silver, aluminium and tin.

5.3.1 Gold

Figure 5.8 shows discrete spectral line emission from the fast plume characteristic of atomic bound-bound transitions. Spectral lineouts in fig. 5.9 were formed by averaging the emission intensity over a 10 pixel region (170 μm) centred at the peak of the atomic plume optical emission which has a velocity of 4.4×10^5 cm s^{-1}.

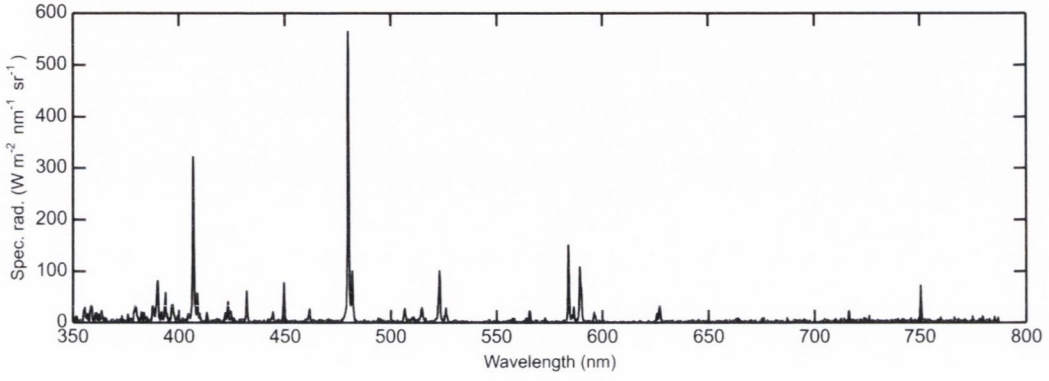

(a) 100 ns

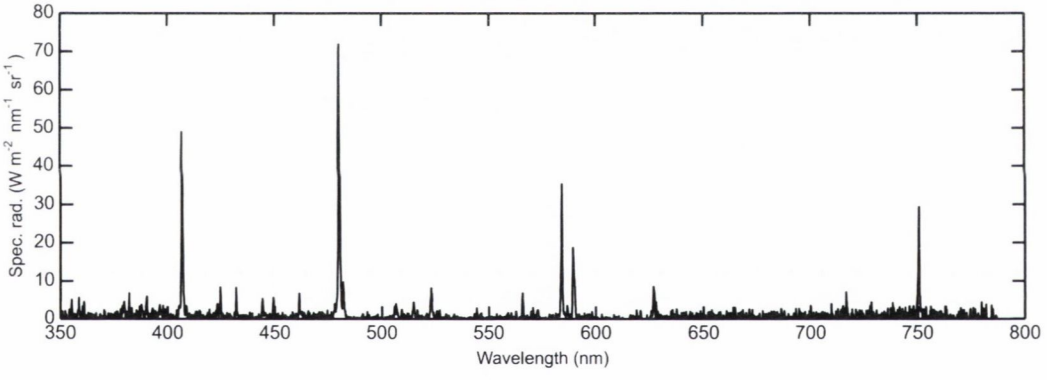

(b) 200 ns

Figure 5.9: Spectral emission from the gold atomic plume recorded (a) 100 ns and (b) 200 ns after the laser pulse with a gate width of ≤ 10% of the delay.

Table 5.3: Main experimentally observed Au I lines.

Wavelength (nm)	g_1:g_2	f_{21}	A_{21} (s^{-1})	E_2 (eV)	Transition
406.07	2:4	0.608	1.226×10^8	7.68	$5d^{10}6d$: $^2D_{3/2} \rightarrow 5d^{10}6p$: $^2P^\circ_{1/2}$
479.5	4:6	0.651	1.259×10^8	7.69	$5d^{10}6d$: $^2D_{5/2} \rightarrow 5d^{10}6p$: $^2P^\circ_{3/2}$
583.9	2:2	0.1640	3.2×10^7	6.755	$5d^{10}7s$: $^2S_{1/2} \rightarrow 5d^{10}6p$: $^2P^\circ_{1/2}$
627.8	4:2	0.01	3.4×10^6	4.63	$5d^{10}6p$: $^2P^\circ_{1/2} \rightarrow 5d^9 6s^2$: $^2D_{3/2}$
751	4:2	0.1878	4.4×10^7	6.755	$5d^{10}7s$: $^2S_{1/2} \rightarrow 5d^{10}6p$: $^2P^\circ_{3/2}$

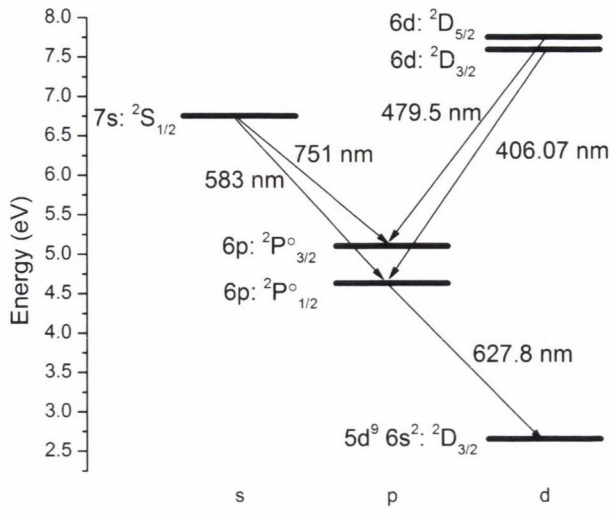

Figure 5.10: Simplified energy level diagram for Au I showing the most important radiatively linked levels. The atomic transitions are detailed in table 5.3.

Properties of the main gold radiative transitions are summarised in table 5.3 and shown on the energy level diagram in fig. 5.10 [78, 79]. The A-values have been calculated from the oscillator strengths using equation 2.20 [79]. Boltzmann plots were calculated from the emission spectra shown in fig. 5.9 and were used to calculate the plasma temperature. Each spectral line was integrated to get the total emission from each transition and applied to equation 2.19 to generate the Boltzmann plots shown in fig. 5.11. The slope of the linear fit is equal to $-1/kT$, for 100 and 200 ns the temperature was found to be 1.1 ± 0.1 and 1.0 ± 0.1 eV respectively.

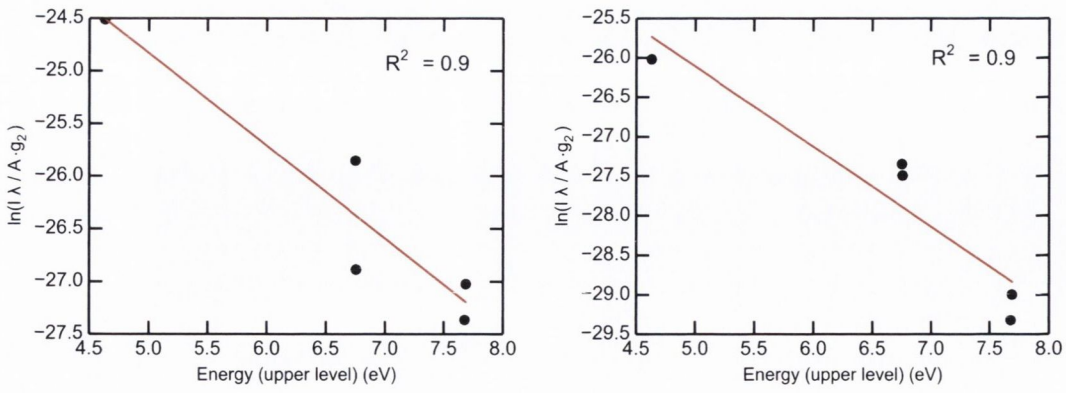

(a) 100 ns **(b)** 200 ns

Figure 5.11: Boltzmann plots of gold at (a) 100 and (b) 200 ns centred at the peak of atomic emission.

5.3.2 Silver

It is clear from figs. 5.8 and 5.12 that the silver femtosecond ablation plume differs significantly from gold. For gold, both plume components were clearly observable, however, for silver spectral images only atomic line emission is clearly resolved. This strong emission coupled to relatively available atomic transition properties makes silver an ideal choice for performing a detailed analysis.

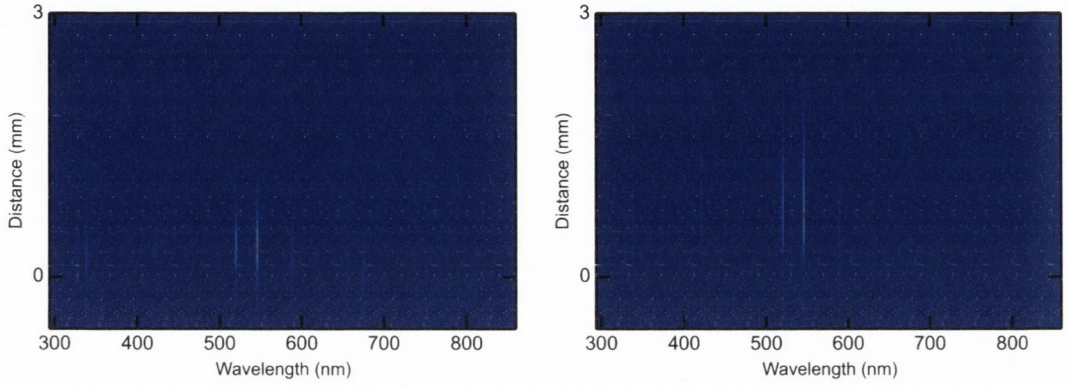

(a) 50 ns **(b)** 100 ns

Figure 5.12: Time and space resolved iCCD images of femtosecond ablated silver at (a) 50 ns and (b) 100 ns after the laser pulse.

Figure 5.13 shows the spectral emission observed at 50 ns after the laser pulse. The main spectral lines are indicated on the plot. The 328 and 338 nm lines are a result of transitions from the $4d^{10}5p$ to the $4d^{10}5s$ ground state. These lines are of much lower intensity than observed previously for nanosecond laser produced plasmas [80]. This may be due to low transmission in the UV through the optical collection system as a result of the two glass achromatic lenses. While the absolute intensity calibration method, described in section 3.2, takes into account the wavelength dependence of the transmission through the optical system, the lower number of counts recorded in this region reduces the accuracy of the calibration method. The spectral lines in the 580-700 nm region are currently unidentified but may be due to Ag II transitions or contamination on the target surface (carbon, oxygen etc.).

A simplified energy level diagram for Ag I is shown in fig. 5.14 indicating the main Ag I levels that give rise to the observed spectral emission. Table 5.4 lists the identified radiative transitions. Energy level data was taken from the NIST spectral database. A_{21} transition rates are only available for some lines in the NIST database [81]. Therefore, the values shown are extracted from the PrismSPECT spectral code [52].

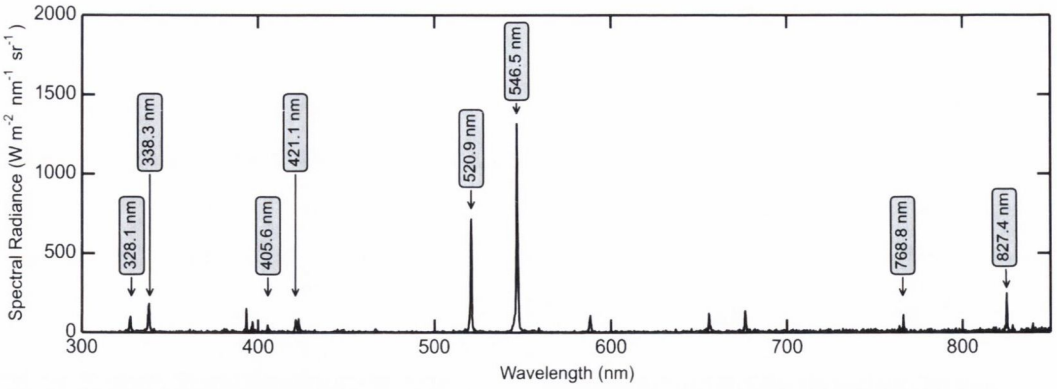

Figure 5.13: Silver spectral emission recorded 50 ns after the laser pulse showing the main observed lines. The atomic transitions are detailed in table 5.4.

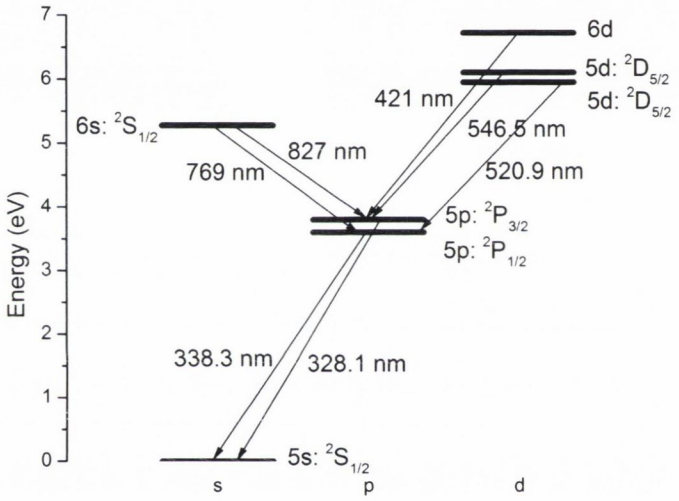

Figure 5.14: Simplified energy level diagram for Ag I showing the most important radiatively linked levels. The main atomic transitions are listed in table 5.4.

Figure 5.15 shows intensity calibrated emission spectra recorded at (a) 200 and (b) 300 ns after the laser pulse. In each case, 10 pixels were binned to improve the signal to noise ratio. This corresponds to approximately 175 μm. For each lineout, the spectra were extracted at the peak of the optical emission which has a velocity of 5×10^4 m s^{-1}.

As described by the Boltzmann equation, the spread in the upper energy levels of observed transitions determines the accuracy of a temperature fit. For the Boltzmann equation to be applicable, the plasma must be optically thin and the levels of interest must be in local thermodynamic equilibrium. The emission spectra will be modelled using PrismSPECT, described in more detail in section 2.3.1. PrismSPECT can model non-LTE level populations, i.e. it does not assume the population of levels follows a Boltzmann distribution. It also takes into account a number of line broadening mechanisms

Table 5.4: Important radiative transitions for Ag I. The transition rates were taken from the PrismSPECT modelling code.

Wavelength (nm)	g_1:g_2 (nm)	A_{21} (s^{-1}) (Prismspec)	E_2 (eV)	Transition
827.4	4 : 2	9.6×10^6	5.276	$4d^{10}6s$: $^2S_{\frac{1}{2}} \rightarrow 4d^{10}5p$: $^2P_{\frac{3}{2}}$
768.8	2 : 2	6.0×10^6	5.276	$4d^{10}6s$: $^2S_{\frac{1}{2}} \rightarrow 4d^{10}5p$: $^2P_{\frac{1}{2}}$
547.2	4 : 4	1.3×10^7	6.043	$4d^{10}5d$: $^2D_{\frac{3}{2}} \rightarrow 4d^{10}5p$: $^2P_{\frac{3}{2}}$
546.5	4 : 6	8.6×10^7	6.045	$4d^{10}5d$: $^2D_{\frac{5}{2}} \rightarrow 4d^{10}5p$: $^2P_{\frac{3}{2}}$
520.9	2 : 4	7.5×10^7	6.043	$4d^{10}5d$: $^2D_{\frac{3}{2}} \rightarrow 4d^{10}5p$: $^2P_{\frac{1}{2}}$
421.3	4 : 4	4.3×10^6	6.72	$4d^{10}6d$: $^2D_{\frac{3}{2}} \rightarrow 4d^{10}5p$: $^2P_{\frac{3}{2}}$
421.1	4 : 6	2.6×10^7	6.721	$4d^{10}6d$: $^2D_{\frac{5}{2}} \rightarrow 4d^{10}5p$: $^2P_{\frac{3}{2}}$
338.3	2 : 2	1.35×10^8	3.66	$4d^{10}5p$: $^2P_{\frac{1}{2}} \rightarrow 4d^{10}5s$: $^2S_{\frac{1}{2}}$
328.1	2 : 4	1.47×10^8	3.77	$4d^{10}5p$: $^2P_{\frac{3}{2}} \rightarrow 4d^{10}5s$: $^2S_{\frac{1}{2}}$

such as, Doppler, natural, instrumental, Stark and opacity. In fig. 5.15, the emission was fitted with a PrismSPECT simulated spectra for the conditions; temperature = 1 eV, $n_i = 9.5 \times 10^{15}\,\mathrm{cm}^{-3}$, thickness = 720 μm which gives a mean charge, $Z = 1$. At 300 ns the best fit was found for the conditions; temperature = 0.75 eV, $n_i = 3.5 \times 10^{15}\,\mathrm{cm}^{-3}$, thickness = 1070 μm and $Z = 0.97$. The best fit was found by comparing the simulated and experimental integrated line intensities of the 827, 768, 546 and 521 nm lines for different plasma conditions. The inset in fig. 5.15b shows the difference between the simulated, and experimental line width of the 521 nm Ag I line. The plasma thickness was estimated from iCCD imaging assuming the plume aspect ratios k_{xz} and k_{yz} are equal. To fit the data, the integrated intensity of each line was compared. The calculated data shown in fig. 5.15 is corrected for the instrumental broadening. As a result of this, the density extracted from the simulations is not based on the spectral linewidth and instead, derived from the absolute intensity of the line. The accuracy of the calculated ion density is strongly influenced by the accuracy of measurement of plasma thickness from iCCD imaging. This is a more appropriate method of determining the plasma density as lines are primarily instrument broadened.

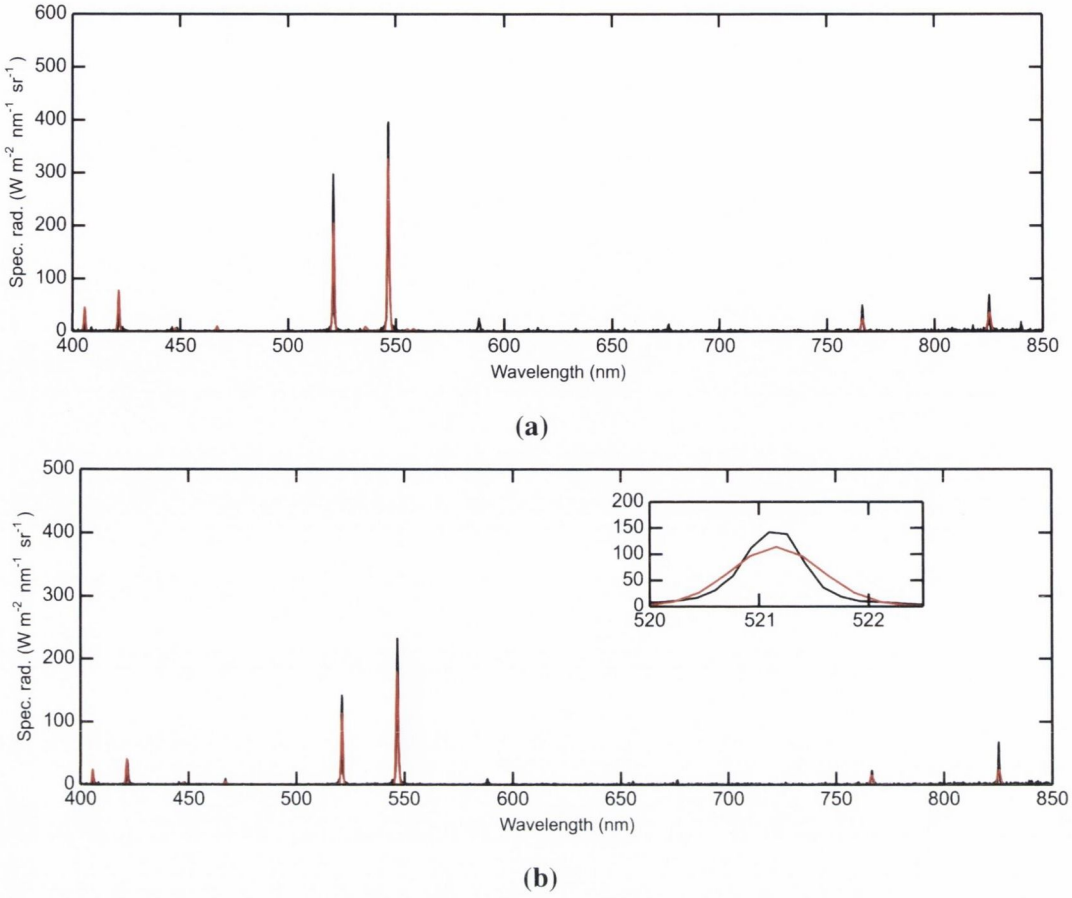

Figure 5.15: Silver spectral emission recorded (a) 200 ns and (b) 300 ns after the laser pulse. The spectral emission was modelled using the PrismSPECT spectral code to estimate the temperature.

To calculate the total mass of the atomic plume by utilizing the normalised density distribution measured using iCCD imaging we must first satisfy certain assumptions; the plume can be described as having a single temperature and the plume is optically thin. This can be proven by modelling the line emission spectra using PrismSPECT at different positions at a fixed time. Figure 5.16 shows the spectral emission 200 ns after the laser pulse. The target position is shown at 0 mm. Spectral line-outs are taken at 3 different distances from the target spaced 750 μm apart. By modelling the plasma properties in each region we can determine if assuming a single temperature is a reasonable approximation. The assumption that the plasma is optically thin will also be investigated using the PrismSPECT code which can output the plasma opacity.

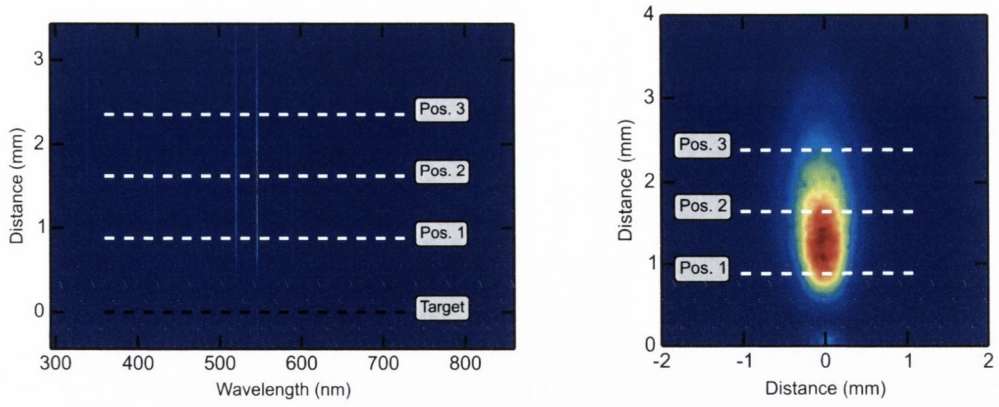

(a) Space resolved spectra **(b)** ICCD imaging

Figure 5.16: Space resolved spectra and iCCD image of silver atomic plume recorded recorded at 200 ns after laser pulse.

Figure 5.17 shows spectral line-outs at the three different positions illustrated in fig. 5.16. As before, the plasma thickness parameter is estimated from iCCD imaging and the spectra is fitted by comparing the integrated line intensity between measurement and simulation. The fitting parameters, summarised in table 5.5, show only a small change in temperature at different positions within the plume.

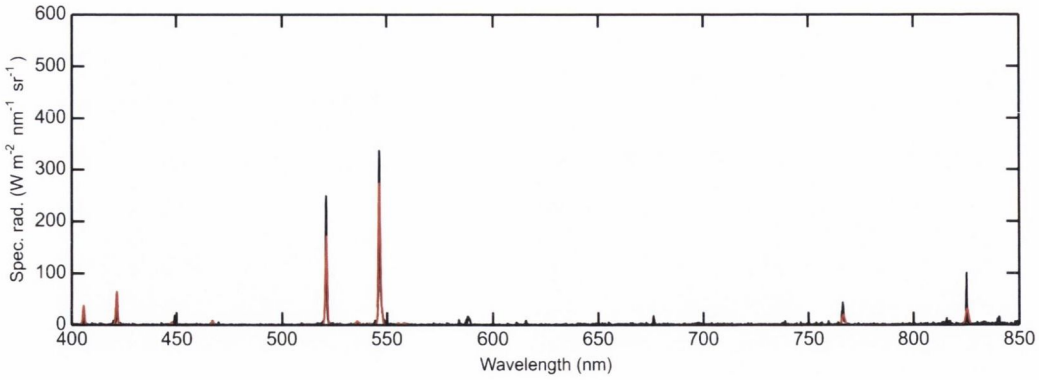

(a) Position 1

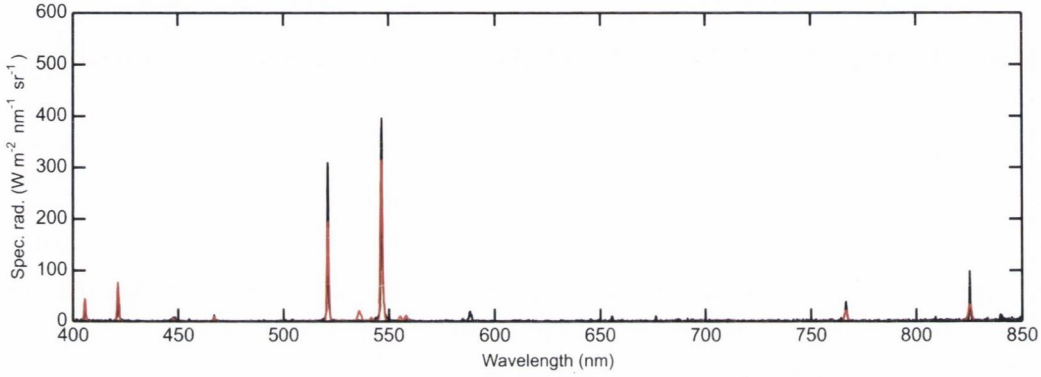

(b) Position 2

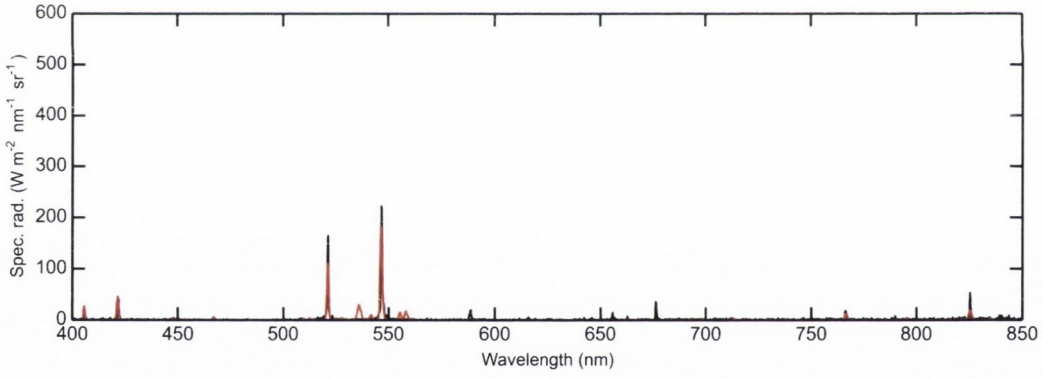

(c) Position 3

Figure 5.17: Lineouts of silver spectral emission recorded at 200 ns at 3 different positions from the target shown in fig. 5.16.

Using PrismSPECT, the plasma opacity can be calculated. Shown in fig. 5.18 the peak optical depth is much less than 1 and therefore, the plume opacity is not significant.

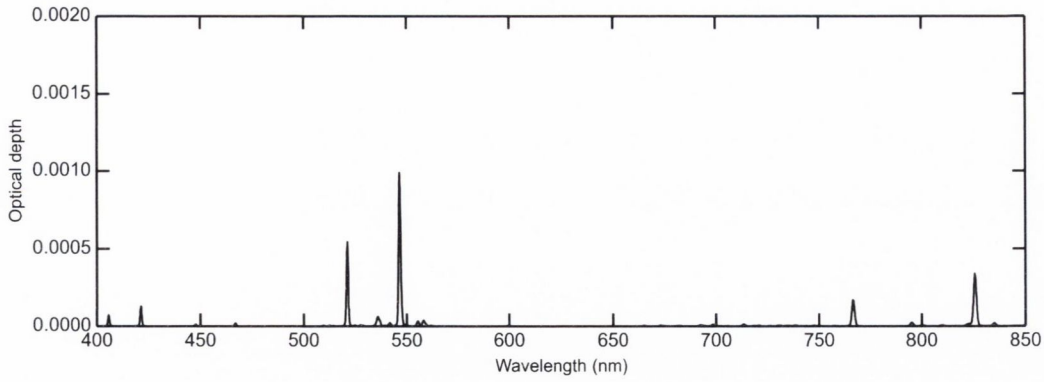

Figure 5.18: Opacity calculated using PrismSPECT for silver atomic plasma emission shown in fig. 5.17b.

Table 5.5: PrismSPECT fitting parameters for silver spectra fitting shown in fig. 5.17.

Position	Thickness μm	Temperature eV	Ion density cm^{-3}	Density×length cm^{-2}
Pos. 1	550	1	1×10^{16}	5×10^{14}
Pos. 2	720	1.05	1×10^{16}	7×10^{14}
Pos. 3	804	1.1	7.5×10^{15}	6×10^{14}

The total number of atoms in the plume can be calculated by relating the normalised density function to the integrated density×length product

$$\int\int n(x, y = 0, z)dxdz = \int\int n'(x, y = 0, z)N_p dxdz \tag{5.5}$$

where n, n', N_p are the atom density, normalised atom density and the total number of atoms in the plume. Integrating fig. 5.16 we find the average spectral radiance between 0.5 and 4 cm along the z-axis as shown in fig. 5.19. Also shown is the PrismSPECT fit for a 1.05 eV, 1×10^{16} atoms cm^{-3} and 450 μm thick plasma. The plasma thickness is the length of the plasma along the x-direction. From this, the plume integrated density×length product, $\int\int n(x, y = 0, z)dxdz$, was found to be 1.6×10^{15} cm^{-1}. Integrating the iCCD image shown in figure 5.16b to solve for $\int\int n'(x, y = 0, z)dxdz$, the total number of particles in the plume, $N_p = 1 \times 10^{13}$.

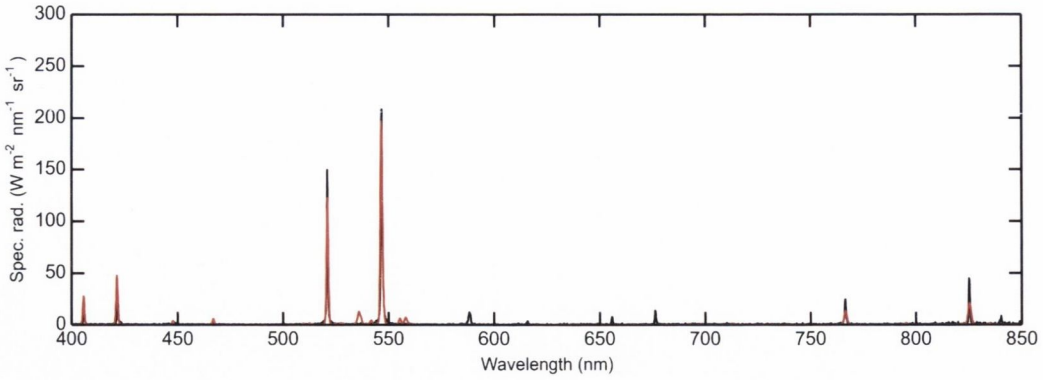

Figure 5.19: Silver atomic plume average spectral radiance in the region from 0.5 to 4 cm recorded 200 ns after the laser pulse fitted with a simulated spectra using PrismSPECT.

As described in section 2.3, the width of a spectral line is influenced by a number of plasma conditions and the experimental setup. Low temperature (few eV), high density ($> 10^{14}$ cm^3) plasmas are primarily instrumental and Stark broadened. Therefore, measurement of spectral line widths allows us to estimate the electron density. For this, the 1200 l/mm spectrometer grating was used, this reduces the spectral range of a single measurement ($\approx$40 nm), but increases the spectral resolution and gives a minimum linewidth of 0.2 nm at 546 nm. Figure 5.20 shows the 520 and 546 nm silver lines recorded (a) 10 ns and (b) 50 ns after the laser pulse. The spectra were generated by binning 10 pixels centred at the position of peak emission in each image. The spectral line widths were fitted with a Voigt function. The Gaussian linewidth parameter was set to 0.2 nm to account for instrumental broadening. The calculated Lorentzian linewidths are given in table 5.6 and their corresponding electron density which are related by

$$\Delta\lambda_{FWHM} = W\frac{n_e}{6.6 \times 10^{16}} \tag{5.6}$$

where W is the Stark broadening parameter. At late times, >50 ns, the lines are primarily instrument broadened, this reduces the accuracy of the Stark density measurements at 100 and 200 ns.

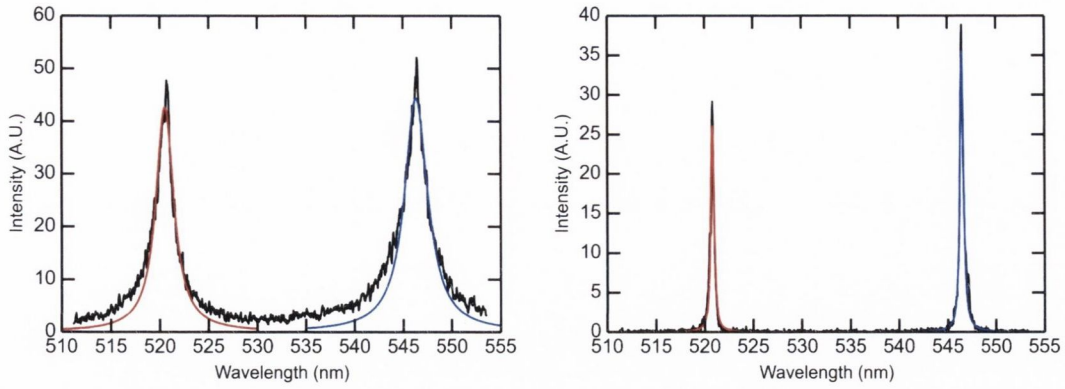

(a) 10 ns **(b)** 50 ns

Figure 5.20: Silver spectral emission recorded using 1200 l/mm spectrometer grating for line width measurements recorded at (a) 10 and (b) 50 ns. The spectral lines have been fitted with a Voigt profile to calculate the FWHM of each line.

Table 5.6: Silver atomic plume electron density measurements, calculated using experimental Stark widths. Linewidths shown have been modified to account for instrumental broadening.

Wavelength (nm)	Time (ns)	Line Width $\Delta\lambda$ (nm)	Electron density (cm^{-3}) Djenize et al.
520.9	10	2.22	6.1×10^{18}
	20	0.94	2.6×10^{18}
	50	0.32	9×10^{17}
	100	0.144	4×10^{17}
	200	0.087	2.4×10^{17}
546.5	10	2.75	7×10^{18}
	20	1.28	3.2×10^{18}
	50	0.36	1×10^{18}
	100	0.099	2.5×10^{17}
	200	0.096	2.4×10^{17}

As mentioned previously, PrismSPECT takes into account spectral line broadening mechanisms. The spectral resolution of the 1200 l/mm grating, $\lambda/\Delta\lambda = 2200$. Using PrismSPECT, the electron density was calculated by fitting the 520.9 nm silver line at 10 and 50 ns was estimated as $2.3 \times 10^{17}\,cm^{-3}$ and $1 \times 10^{16}\,cm^{-3}$ respectively. Fitting this line with experimental Stark broadening parameters, the electron densities were $6.1 \times 10^{18}\,cm^{-3}$ and $9 \times 10^{17}\,cm^{-3}$ respectively.

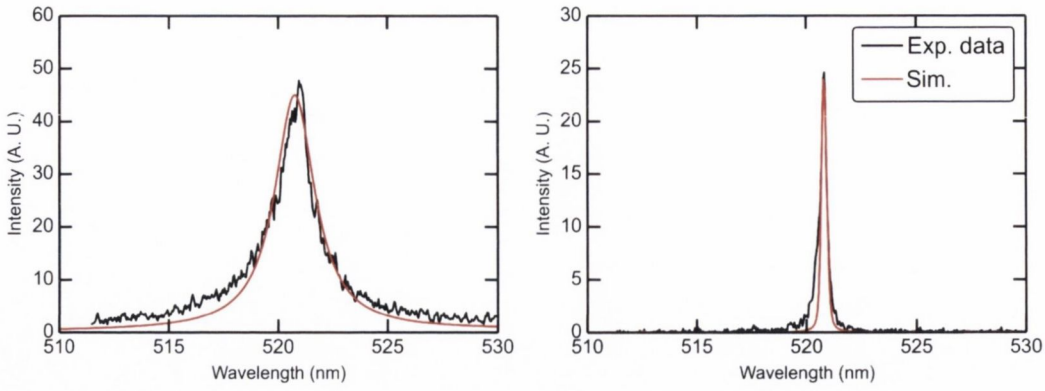

(a) 10 ns **(b)** 50 ns

Figure 5.21: Silver 520.9 line using 1200 l/mm grating at (a) 10 and (b) 50 ns fitted using prismSPECT resulting in a electron density of 2.3×10^{17} cm^{-3} and 1×10^{16} cm^{-3} respectively.

5.3.3 Aluminium

As shown in fig. 5.22, the aluminium atomic plume emission observed was of low intensity and did not result in many visible atomic line transitions. The two main clearly resolved transitions are the 394 and 396 nm. As they both have the same upper level the temperature of the plasma cannot be estimated by generating a Boltzmann plot.

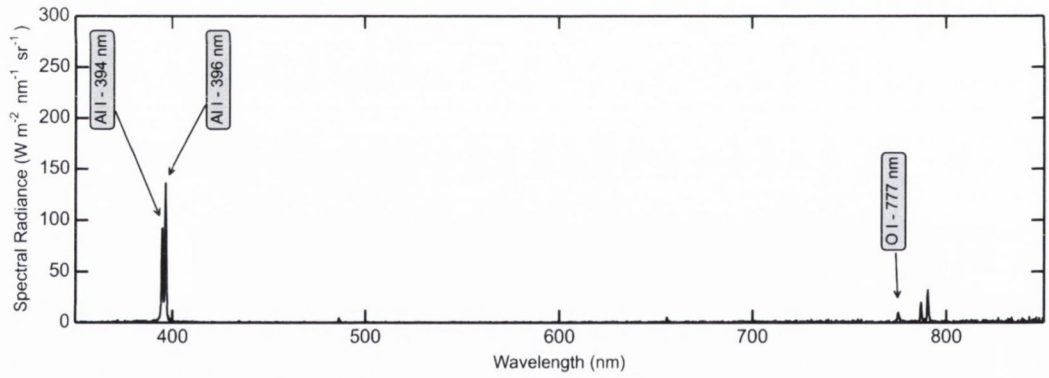

Figure 5.22: Aluminium spectral emission recorded 100 ns after the laser pulse showing the main observed lines. The atomic transitions are detailed in table 5.7.

Table 5.7: Important radiative transitions for Al I.

Wavelength (nm)	g_1:g_2 (nm)	A_{21} (s^{-1}) PrismSPECT	E_2 (eV)	Transition
396	4 : 2	9.8 x 10^7	3.14	$3s^2 4s$: $^2S_{\frac{1}{2}} \rightarrow 3s^2\ 3p$: $^2P_{\frac{1}{2}}$
394	2 : 2	4.9 x 10^7	3.14	$3s^2 4s$: $^2S_{\frac{1}{2}} \rightarrow 3s^2\ 3p$: $^2P_{\frac{3}{2}}$

5.4 Conclusions

For each material, the number of ions present in the plasma, detected at 3 cm from the target using the Langmuir probe was between 10^{11} and 10^{12}. A fast initial peak was observed in the probe signal which is due to low-Z contaminates on the target surface.

The aspect ratio of the plasma plume expansion was measured and found to vary from material to material due to the variation of the initial plume shape (spot size, plasma initial thickness). Our experimental observations point to a complex material relaxation process that determines the relative spectral intensity observed from the atomic and nanoparticle plume components. Gold exhibits strong atomic and nanoparticle plume emission in the visible. This is first suggested by iCCD imaging as the two plume components are clearly resolved and verified by space resolved spectroscopy. This is in contrast to observed emission from silver and tin plumes. From iCCD imaging, the silver atomic plume dominates its optical emission. At the other extreme, for tin, the atomic plume is only weakly observed.

For aluminium, the only identified lines are from low lying upper levels, this suggests, but does not confirm that the atomic aluminium plume is of low temperature. The low number of visible spectral lines from the aluminium and tin atomic plasmas has limited the extent to which spectral analysis can be carried out to determine their plasma properties.

A detailed characterisation of the silver atomic plume was made. Intensity calibrated spectroscopy measurements were utilized to investigate the plume properties. The plume temperature was determined to be $\approx$ 1 eV at 200 ns, dropping to 0.75 eV at 300 ns. Fitting the silver plume at 200 ns at three different positions with modelled fits using PrismSPECT. From this, a small dependency of plume temperature on position was observed, with T_e= 1 eV at 0.8 mm from the plasma to T_e = 1.1 eV at 2.3 mm. The absolute intensity calibration of the emission spectra allows a density and plume thickness to be determined from spectral modelling. The opacity was calculated using the PrismSPECT code. From this analysis, we have determined that at 200 ns, the plume is optically thin and it is reasonable to approximate the plume temperature as being single valued. A method was developed to calculate the total amount of material in the plume by measuring plume spectral radiance along the axis normal to the target and compared to iCCD images. From this, the total number of atoms in the in the silver atomic plume was found to be 1×10^{13} with a mean charge, Z $\approx$ 1. This is approximately 50 times higher than the number of ions measured using the Langmuir probe positioned 3 cm from the target. This difference may be due to radiative recombination and cooling of

the plasma between the time the emission measurements were made (200 ns) and when the ions reach the probe positioned at 3 cm.

By utilising multiple diagnostic methods the variation of the plasma plume parameters across the range of materials studied. In later chapters we will see how this impacts the nanoparticle plume in vacuum and background gas. By using a wide range of diagnostic methods we have built up a detailed description of the ablation process, from the material removed to the deposited material.

Chapter 6

Nanoparticle plume dynamics

The femtosecond laser produced nanoparticle plumes were studied for gold, silver, aluminium and tin. The experimental setup has been described previously in chapter 4. As described in chapter 2, due to the laser heated volume undergoing complex relaxation mechanisms, femtosecond laser ablation produces two distinct plume components. This chapter is focused on the slower, nanoparticle plume component. Amoruso et al. have previously studied the plume spectral emission to estimate the nanoparticle plume temperature and cooling rate [58]. They assumed the emissivity of a silicon nanoparticle followed a $1/\lambda$ dependence and fitted the spectral emission with a blackbody function to calculate the nanoparticle plume temperature. This assumption holds true if the material refractive index can be approximated as wavelength independent in the spectral region studied. For most metals this is not true. We expand on this analysis by; (a) accounting for the variation of refractive index with wavelength and (b) performing absolute spectral emission measurements to extract a more accurate temperature measurement and to make an *in situ* estimate of the total amount of material in the plume.

Secondly, we will further our study on the different behaviour of ablated materials. As seen in chapter 5, the observed relative emission intensity of the atomic and nanoparticle plumes vary with material. The silver nanoparticle plume was not clearly resolved using space resolved spectroscopy. In contrast, for tin, the atomic plume emission was barely resolvable. By combining analysis of absorption and emission measurements we aim to determine whether this is due to a lower plume temperature, leading to reduced emission or due to differences in the partition of ablated material between atoms, ions and nanoparticles.

6.1 ICCD imaging

When viewed by optical emission, the nanoparticle plume expansion is observed to undergo remarkably different dynamics compared with that of the plasma plume. As seen previously, using emission measurements, the atomic plume is observed to disconnect from the target as it propagates away from the target surface. Figure 6.1 shows time resolved iCCD images of the nanoparticle plume recorded at 500 ns, 5 μs and 10 μs after the laser pulse. In each case, the camera gate width for iCCD imaging was ≤5% of the delay. As the plume progresses, it remains connected to the target with the peak of emission just in front of the target surface. This is consistent with a theoretical plume expansion described by the Anisimov model.

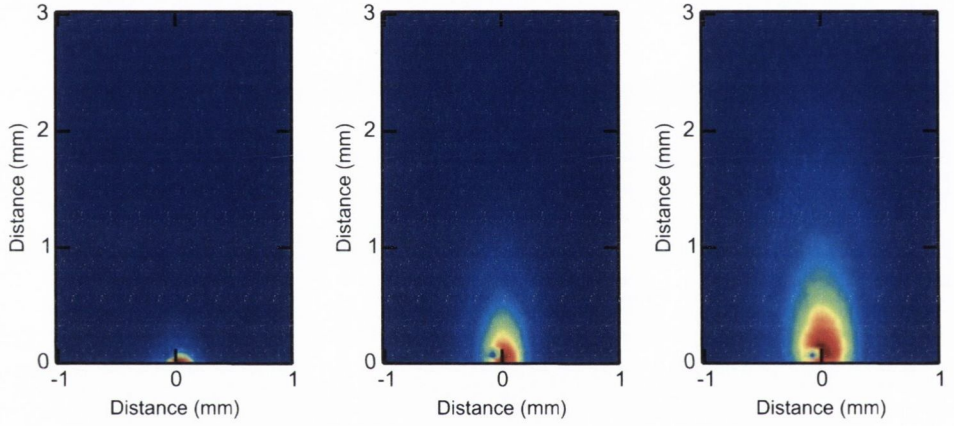

(a) 500 ns **(b)** 5 μs **(c)** 10 μs

Figure 6.1: ICCD images of the gold nanoparticle plume at (a) 500 ns, (b) 5 μs and (c) 10 μs.

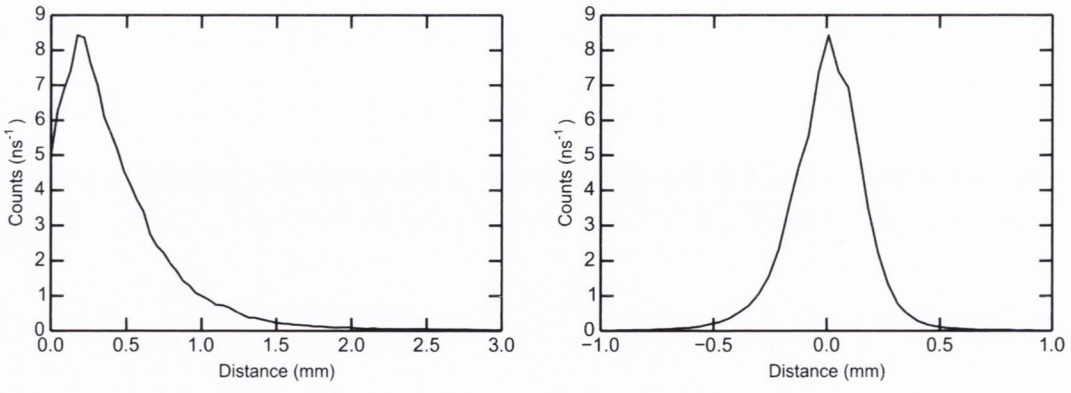

(a) **(b)**

Figure 6.2: Gold nanoparticle plume emission intensity at 10 μs (a) along the target normal and (b) parallel to target surface through the point of maximum counts (200 μm from the target surface).

Figure 6.2 shows iCCD lineouts taken parallel and perpendicular to the target surface 10 μs after the laser pulse. The plume dimensions were measured at the point at which the intensity had fallen to 10% of it's peak value. From this, the plume aspect ratio, k_{zy} was estimated to be ≈3.7. The atomic plume aspect ratio was found, using a Langmuir ion probe, to be ≈4.3. Figure 6.3 shows the linear fit for the nanoparticle plume front velocity. The gold nanoparticle plume front velocity was measured as $(1.4 \pm 0.1) \times 10^4\,\mathrm{cm\,s^{-1}}$, this is approximately 50 times slower than the gold atomic plume.

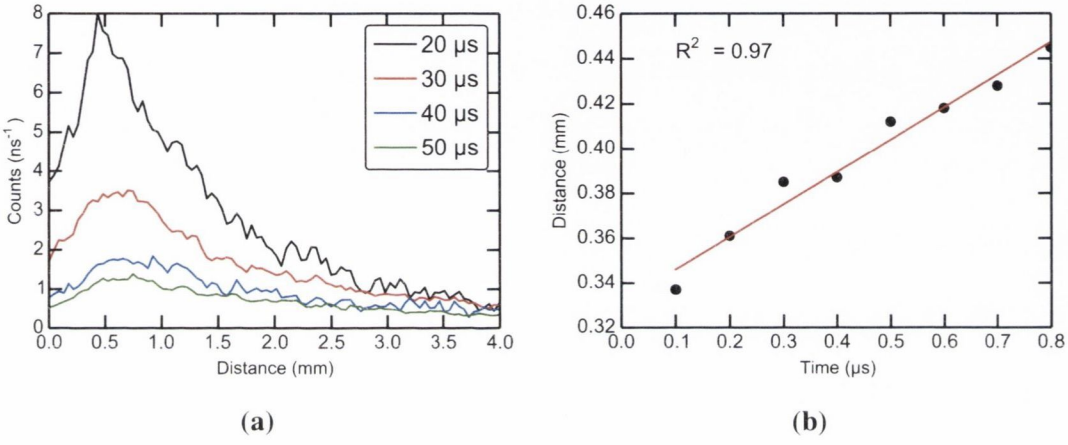

Figure 6.3: (a) Lineouts extracted from iCCD images of the gold nanoparticle plume at different times and (b) nanoparticle plume front velocity fit.

6.2 Nanoparticle plume spectroscopy

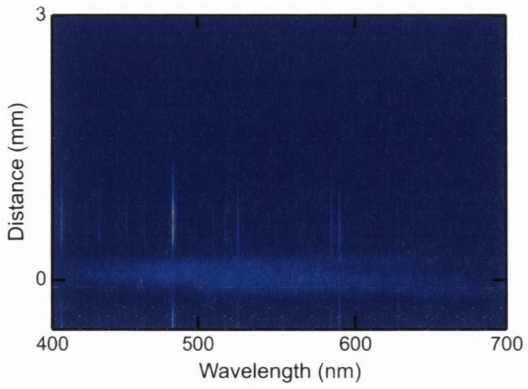

Figure 6.4: Space resolved spectral emission from femtosecond ablation of gold 100 ns after the laser pulse.

In fig. 6.4, the space resolved spectral emission recorded 100 ns after the laser pulse is shown. The atomic plume, distinguishable by its characteristic discrete line emission disconnects from the target and expands away. The reflection of the atomic plume from the target surface is clearly visible at the bottom of the image. The nanoparticle plume emission is observed as a broad continuum which remains close to the target surface as a result of the lower nanoparticle plume velocity. This broad emission feature of the slow, nanoparticle plume component has been observed for a number of metals by various research groups [18, 59, 82, 83]. Using *in situ* x-ray absorption, Oguri et al. has shown that for aluminium, the plume is comprised of nanoparticles in a liquid state [19]. The visible broad continuum is as a result of black-body emission from the nanoparticles. The spectral intensity from a single nanoparticle can be described by modifying the black-body equation for the nanoparticle emissivity, ϵ_{NP}, given by equation 2.28,

$$I_{NP,single}(\lambda, T) = \frac{2\pi hc^2 a^2}{\lambda^5} \frac{\epsilon(\lambda, a)}{exp\left(\frac{hc}{\lambda kT}\right) - 1} \quad \mathrm{W\,m^{-1}\,sr^{-1}} \tag{6.1}$$

where a is the nanoparticle radius. The emissivity, given in equation 2.28 is defined as

$$\epsilon(\lambda, a) = \frac{8\pi a}{\lambda} Im\left[\frac{m^2 - 1}{m^2 + 2}\right] \tag{6.2}$$

where m is the complex refractive index of the material. The spectral emission density per unit volume of the nanoparticle plume is given by

$$
\begin{aligned}
u(\lambda, T) &= I_{NP,single}(\lambda, T)\frac{\rho_{NP}}{\frac{4}{3}\pi a^3 \rho_L} \quad \mathrm{W\,m^{-1}\,m^{-3}\,sr^{-1}} \\
&= \frac{1}{\rho_L}\frac{12\pi hc^2}{\lambda^6} Im\left[\frac{m^2-1}{m^2+2}\right]\frac{1}{exp\left(\frac{hc}{\lambda kT}\right)-1} \times \rho_{NP} \\
&= J_{NP}(\lambda, T)\,\rho_{NP}
\end{aligned}
\tag{6.3}
$$

where $J_{NP}(\lambda, T)$, ρ_L and ρ_{NP} are the coefficient of emissivity, the material liquid density and mass density of the nanoparticle plume respectively. The spectral radiance, $L_{NP}(\lambda, T)$, recorded from a NP layer is given by

$$
L_{NP}(\lambda, T) = \int_{-X}^{+X} J_{NP}(\lambda, T)\,\rho_{NP}\,dx \quad \mathrm{W\,m^{-1}\,m^{-2}\,sr^{-1}} \tag{6.4}
$$

where the integral is taken along the line of sight. $+X$, $-X$ are the plume dimensions along the optical axis. The alignment of space resolved spectroscopy is such that the z-direction of the plasma is imaged onto the spectrometer slit, therefore the integrated intensity is given by

$$
\int_0^Z L_{NP}(\lambda, T)\,dz = \int_0^Z \int_{-X}^{+X} J_{NP}(\lambda, T)\,\rho_{NP}\,dxdz \quad \mathrm{W\,m^{-1}\,m^{-1}\,sr^{-1}} \tag{6.5}
$$

where Z is the plume dimension perpendicular to the target. The nanoparticle plume mass density, ρ_{NP}, can be defined in terms of the normalised density, ρ'_{NP} as

$$
\rho'_{NP}(x, y, z) = \frac{\rho_{NP}(x, y, z)}{M_{NP}} \tag{6.6}
$$

where M_{NP} is the total mass of the plume. The normalised density distribution integrated along the x-axis can be calculated from iCCD imaging assuming the plume is optically thin and can be approximated as having a single temperature by relating the radiance at a given position to the radiance integrated over the iCCD.

$$
\int_{-X}^{+X} \rho'_{NP}(x, y, z)dx = \frac{L(y, z)}{\int_0^Z \int_{-Y}^{+Y} L(y, z)dydz} \tag{6.7}
$$

where L(y,z) is the plasma radiance recorded by the iCCD camera. Figure 6.5 and 6.6 also shows the integrated spectral emission from the space resolved spectral images. To cover a wide spectral range the grating was re-centered at different central wavelengths. This has caused a discontinuity in some spectral lineouts observed at ≈625 nm. In fig. 6.5, spectral line emission from the atomic and nanoparticle plumes were studied up until 800 ns. The atomic plume is observed to expand rapidly away from the target due to its greater velocity. From approximately 400 ns the atomic plume is barely observable. The spectra was intensity calibrated by the procedure described in section 3.2 and fitted using equation 6.5 to estimate the temperature and total mass of the plume.

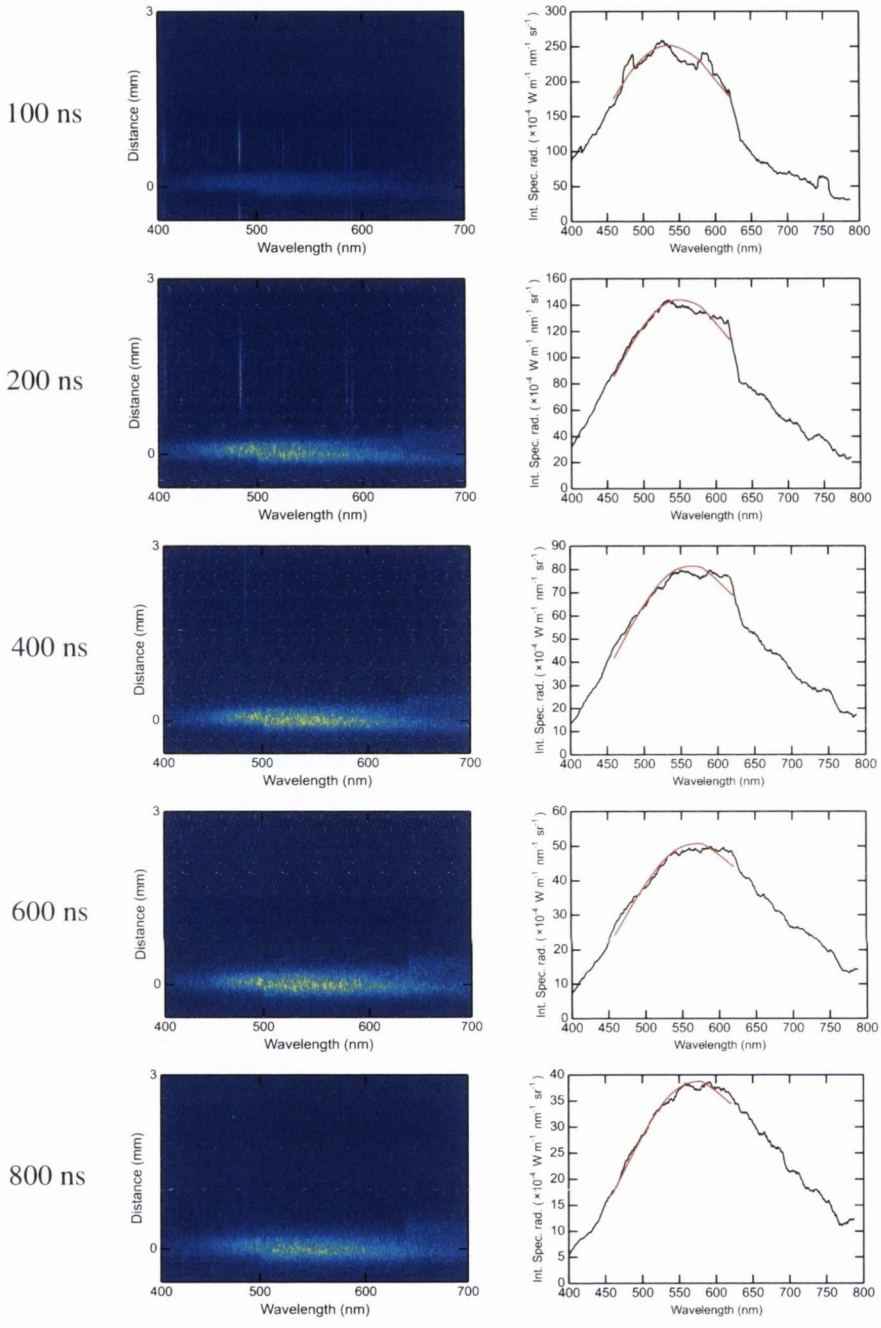

Figure 6.5: Time and space resolved spectroscopy and spectral lineouts with corresponding fits for gold nanoparticle plume from 100 to 800 ns.

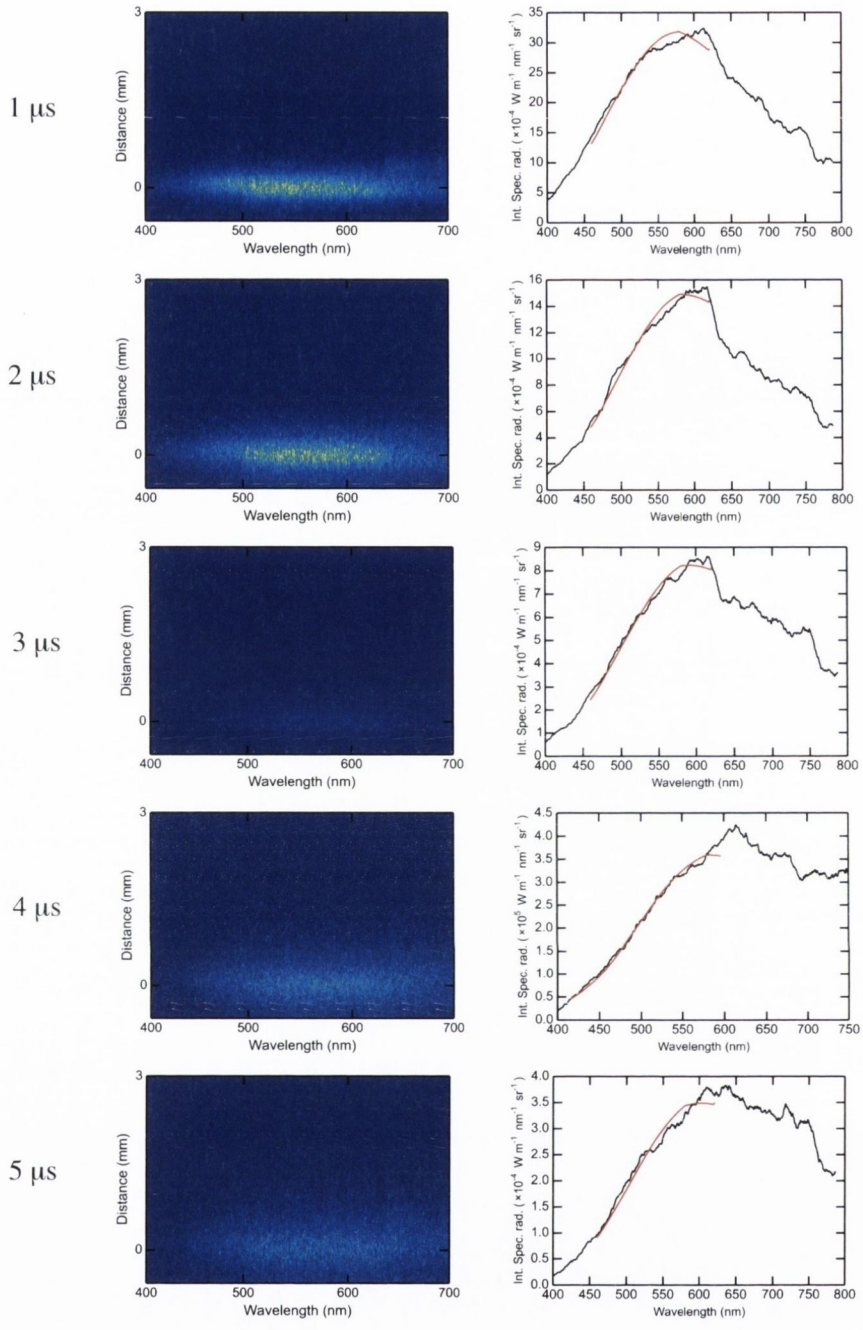

Figure 6.6: Time and space resolved spectroscopy and spectral lineouts with corresponding fits for gold nanoparticle plume from 1 to 5 μs.

As a result of the spectral fitting procedure the time dependent temperature variation of the nanoparticle plume was measured. To generate the emission spectra, the space resolved spectrum is integrated along the propagation direction, and hence, the value of temperature calculated is the average temperature over the whole plume length. Figure 6.7 shows the temporal variation of the temperature of the gold nanoparticle plume. Initially, at 200 ns, the plume undergoes rapid cooling with a rate of temperature change

of 1600 K μs^{-1}. At 2 μs, the rate of temperature change has decreased to 90 K μs^{-1}. The emission of hot gold nanoparticles have been studied previously [6]. Amoruso et al. studied the spectral emission from silicon nanoparticles and to estimate the nanoparticle plume temperature, they approximate the emissivity as proportional to $1/\lambda$ [58]. From 10 μs to 150 μs after the laser pulse they find that the dominant cooling mechanism is radiative emission. Harilal et al. studied the tungsten NP plume emission, they ablated tungsten with a 40 fs laser producing a power density of 2×10^{14} W cm^{-2} on the target, which is approximately 10 times the irradiance of our study [59]. They studied the cooling of the nanoparticle plume from earlier in time ($\approx$1 μs). A similar effect is observed to that shown for gold in fig. 6.7. Initially, at 1 μs, the tungsten NP plume temperature is $\approx$4250 K and undergoes a rapid decay in temperature until approximately 10 μs where there is a much slower cooling rate. The gold NP plume observed in our experiments is initially much cooler with a temperature of 2625 K at 200 ns, however this can be explained by the different thermal properties between gold and tungsten and the lower intensity laser spot used in our experiments. Tungsten and gold have boiling points of 6203 K and 3233 K respectively, this allows for a much higher upper limit on tungsten nanoparticle temperatures. By comparing the variation in spectral emission versus temperature the error in the temperature measurement was estimated to be $\approx$50 K.

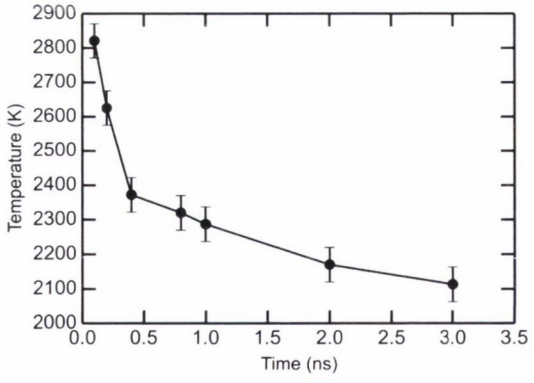

Figure 6.7: Gold nanoparticle plume temperature versus time calculated from nanoparticle emission spectra.

As described in section 2.5, there are three main cooling mechanisms for a hot nanoparticle in vacuum; thermionic emission, evaporation and optical radiation. Thermionic emission initially has a fast decay rate but with each electron emission and subsequent charging of the nanoparticle causes a large reduction in emission rate (shown in fig. 2.16). Hence, this mechanism only has a small contribution to the nanoparticle cooling rate. As discussed in section 2.5, evaporation from nanoparticle clusters with a radius 5 nm can be treated as evaporation from a bulk surface. Cooling due to optical radiation was treated by calculating the nanoparticle emission spectrum and numerically integrating over the spectrum to get the power radiated. The possibility of applying the modified Stefan-Boltzmann equation to take into account a $1/\lambda$ dependence of the emissivity was considered and discussed in section 2.4. However, because the choice of the emissivity in either case was somewhat arbitrary it was determined that numerical integration of the blackbody spectrum is a more precise method.

Table 6.1: Temperature cooling rates calculated for evaporation and optical radiation at two different temperatures corresponding to plume temperature at 200 ns and 2 μs.

Time	Temperature	Radiation	Evaporation
200 ns	2625 K	23 K μs^{-1}	2580 K μs^{-1}
2 μs	2170 K	9 K μs^{-1}	100 K μs^{-1}

As seen from table 1.1, evaporation is the dominant mechanism in the time frame studied. The accuracy of the optical radiation calculation is limited as there is no information on the high temperature near infra-red optical constants. The number density at the saturation vapour pressure for a given temperature is strongly dependent on the boiling point of the material (section 2.5).

There has been studies that show a reduction in melting point for nanoscale materials, it is feasible that the boiling point is also affected. Therefore the use of bulk thermal properties of a material could be a source of error. Thus far we have considered the nanoparticles to be isolated and the surrounding medium to be vacuum. It is unclear whether or not there is vapour present as the nanoparticle plume expands and therefore, nanoparticle cooling could also be influenced by nanoparticle-vapour collisions.

6.3 Single wavelength absorption

To further characterise the nanoparticle plume a single-wavelength absorption probe was utilised. Unlike spectral emission, plume absorption is only weakly dependent on temperature which is due to the temperature variation of the refractive index. Therefore, the plume should be observable in absorption long after the emission intensity has reduced below the detection limit. A similar method has previously applied to nanosecond laser produced plasma atomic plumes by Schittenhelm et al. [84, 85].

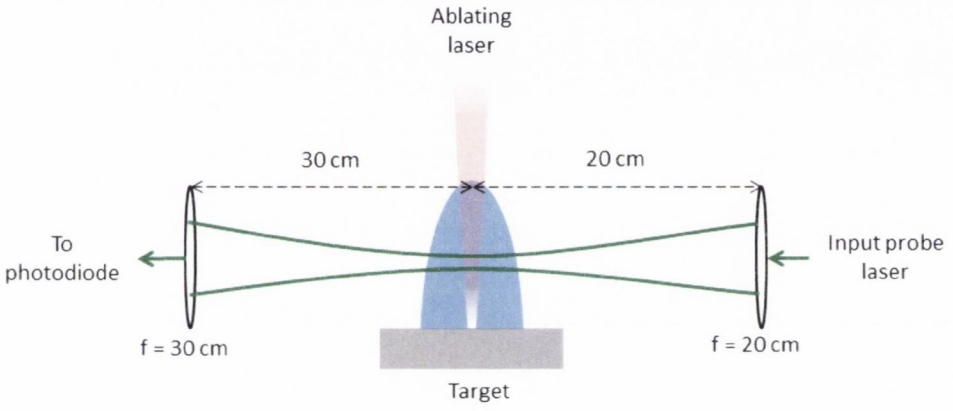

Figure 6.8: Simplified diagram of the experimental setup for optical absorption measurements.

A schematic diagram of the setup is shown in fig. 6.8, a more detailed discussion on the setup is given in section 3.4. As mentioned previously, at a given time, the plume has a variation in density versus distance from the target, which results in deflection of the probe beam. The optical system was designed such that small deflections of the laser beam as it passes through the plasma would not result in a deflection of the beam position off the photodiode. The maximum deflection that the beam can undergo and still be collected by the first lens, and hence, be detected by the photodiode, is $\approx 5^{\circ}$. It has been shown previously that for nanosecond plasma plumes that this acceptance angle is large enough to account for the deflection [86–88]. Figure 6.9 shows the temporal variation of the optical transmission for target probe distances in the range from 100-500 μm. As distance is increased there is a reduction in the minimum transmission and a shift in the peak position. Also shown is the density×length product, calculated using equation 3.15 which is the measure of the density of the plume at the probe beam position integrated along the line of sight of the laser probe, x-axis.

The gold transmission signal is observed to have two components, a fast and a slow peak. The origin of the faster absorption feature is not clear at this stage, but may be due to vapour absorption. In fig. 6.10, the plume front was measured as a function

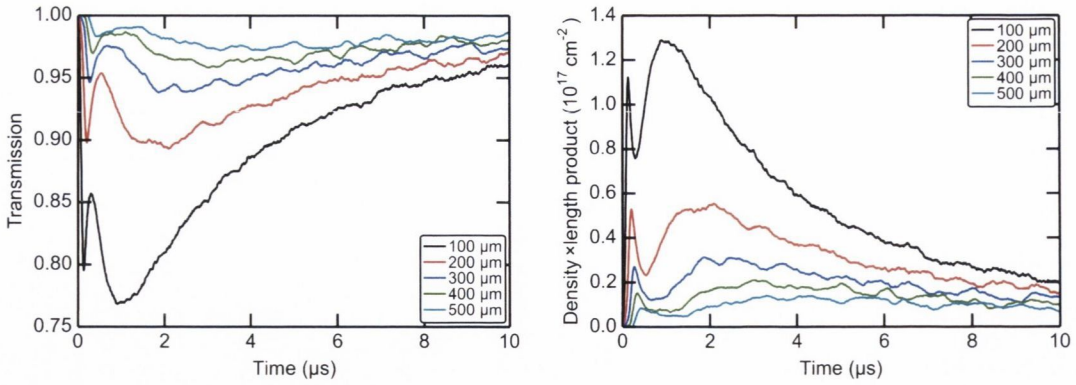

Figure 6.9: Optical absorption measurements of the gold NP plume, recorded at distances of 100-500 μm and (b) corresponding density×length product.

of distance and time and a linear fit was used to calculate the velocity of each plume component which were found to be 1.9×10^5 cm s^{-1} and 3.7×10^4 cm s^{-1}. The plume front was found by measuring the time at which the density×length product is at 10% of the maximum value. From iCCD imaging, the atomic and nanoparticle plume front velocities was estimated as 8×10^5 cm s^{-1} and 1.4×10^4 cm s^{-1} respectively.

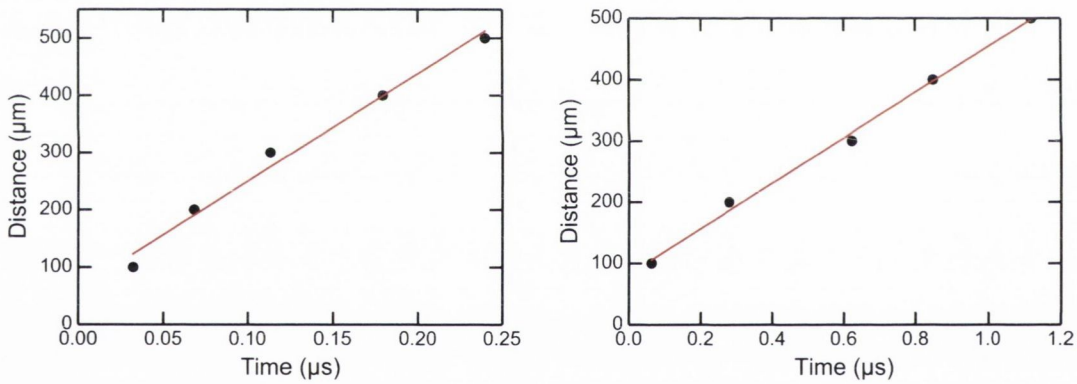

(a) **(b)**

Figure 6.10: Plume front positions of the (a) fast and (b) slow component from fig. 6.9, The plume front was approximated as 10% of the peak value.

Assuming a self-similar expansion, we can relate the density×length product at a given position, z_p and time t_0 to the density×length product at a different time t as a function of space, z by

$$\begin{aligned} nL(z', t_0) &= nL(z_p, t)\left(\frac{t}{t_0}\right)^2 \\ z' &= z_p\left(\frac{t_0}{t}\right) \end{aligned} \tag{6.8}$$

where $nL(z', t_0)$ is the density×length product measured by the absorption probe at a position z_p. In fig. 6.11, the density×length product at 200 μm was converted to spatially resolved density×length at 5 μs after the laser pulse. The red circles represent data measured directly from the signals shown in fig. 6.9b. The agreement between the calculation and discrete points measured directly suggests that treating the plume as undergoing a self-similar expansion is a reasonable approximation.

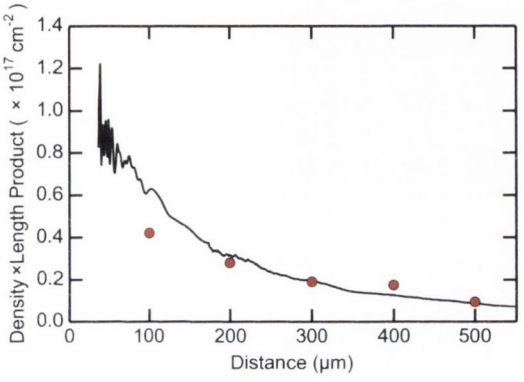

Figure 6.11: Variation in density×length product as a function of space (black line) at 5 μs and density×length product measured from absorption measurements taken at 100 - 500 μm (figure 6.9).

Single wavelength absorption measurements provide a quantifiable measurement of the amount of material at the probe beam position. From this, we can calculate the total amount of material in the plume if we know the material distribution. The normalised distribution was found using two methods.

1. Anisimov model
2. Normalised density analysis using iCCD imaging

Firstly, we will look at using the Anisimov model, described in section 2.2 to calculate the normalised density×length product. By assuming the plume undergoes a self similar expansion, ie. that its properties are constant along semi ellipsoidal surfaces, and that the expansion is adiabatic and isentropic we can employ the Anisimov model to describe the plume propagation. As the Anisimov model applies to an adiabatic, self similar gas expansion, the correct choice of γ for an ensemble of nanoparticles is unclear. Previous studies of atomic nanosecond plumes have used values in the range of 1.1-1.4. $\gamma = 1.3$ was used in this study [47, 89]. The plume initial dimensions parallel to the target surface was set to the crater dimensions, 180 × 220 μm. The plume initial dimension perpendicular to the target was varied to achieve the best fit and found

to be 1.1 μm. Figure 6.12a shows the experimentally measured density×length product at distances 100-500 μm. Figure 6.12b shows the time variation of the density×length product (normalised to the number of atoms in the nanoparticle plume) calculated using the Anisimov plume expansion model. The overall behaviour is quite similar to the experimental measurements shown, though the calculated temporal width is somewhat smaller. The width of the peak is related to the choice of gamma. A larger value of gamma may improve the fit but there is no scientific evidence to suggest that this would be a reasonable choice for a nanoparticle plume. The total number of atoms in the nanoparticle plume can be obtained by comparing the magnitudes of the signals in figs. 6.12a and 6.12b. the value obtained is 3×10^{13} which is in good agreement with the net deposition per pulse.

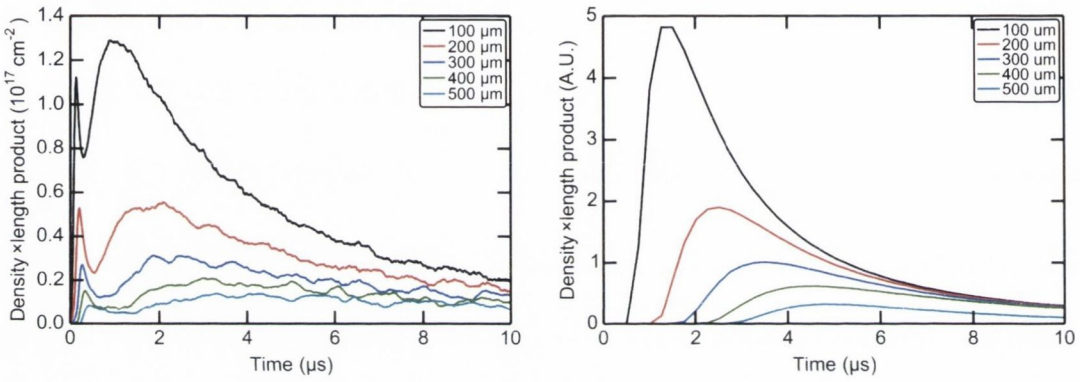

(a) **(b)**

Figure 6.12: Temporal variation of (a) the density×length product at various distances from the target surface and (b) the density×length product (normalised to the number of atoms in the NP plume) calculated using Anisimov plume expansion model.

Secondly, assuming the plume is optically thin and in thermodynamic equilibrium we can determine the total amount of material in the plume from analysing iCCD images. From equation 3.15, we can relate the transmission through the probe beam to the particle absorption cross-section and number density by

$$-\ln(T(y=0,z)) = \int_{-X}^{+X} C_{NP}(a,x) n_{NP} dx \tag{6.9}$$

where $+X$, $-X$ are the plume dimensions along line of sight at a distance z from the target. This can be written in terms of the normalised density distribution, ρ' calculated from iCCD imaging using equation 6.7.

$$-\ln(T(y=0,z)) = \frac{6\pi}{\lambda} Im\left[\frac{m^2-1}{m^2+2}\right] \frac{M_p}{\rho_L} \int_{-X}^{+X} \rho'(x,y=0,z)dx \tag{6.10}$$

From this, we can calculate the total mass of the plume, M_p and hence, the number of particles which was found to be 2×10^{13}.

6.4 Other materials

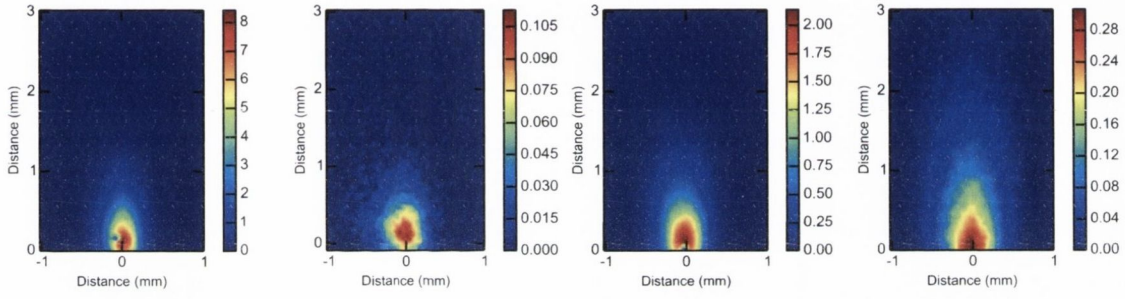

(a) Gold **(b)** Silver **(c)** Tin **(d)** Aluminium

Figure 6.13: ICCD imaging of the nanoparticle plume 5 µs after the laser pulse for (a) gold, (b) silver, (c) tin and (d) aluminium. The counts scale is in counts per nanosecond.

From the iCCD images in fig. 6.13, we can see that there is a number of differences in the optical emission observed from the nanoparticle plume of each material. Aluminium, the lightest element, shows the fastest nanoparticle plume front velocity of 4.4×10^4 cm s^{-1}. Each image was recorded with the same camera gain settings and the count scale normalised to the number of counts detected per nanosecond to account for the differences in gate width. From this, at 5 µs, the silver emission is approximately 80 times weaker than gold. While this may initially lead to the conclusion that the amount of material in the nanoparticle plume of silver is significantly less than that of gold, the iCCD images recorded are not spectrally calibrated and there are a number of factors the influence the number of counts detected on the iCCD. The camera responsivity is dependent on wavelength, with a maximum responsivity in the visible. Therefore, if a plasma strongly emits in the UV the number of counts recorded will be much less than if the emission, of the same intensity, was predominantly in the visible region. Table 6.2 compares the front velocities of the plasma and nanoparticle plumes observed using iCCD imaging. The tin plasma plume emission was weak and hence an accurate measurement of the tin plasma plume front could not be made from the iCCD images.

Table 6.2: Measured atomic and nanoparticle plume velocities from iCCD imaging.

Material	Plasma plume velocity $\times 10^6$ cm s^{-1}	NP plume velocity $\times 10^4$ cm s^{-1}
Gold	0.8 ± 0.3	1.4 ± 0.1
Silver	1.5 ± 0.1	1.4 ± 0.1
Aluminium	1.6 ± 0.1	4.4 ± 0.1
Tin	-	2.2 ± 0.3

Absolutely calibrated spectroscopy allows for a quantitative comparison of the nanoparticle plume emission. The spectral radiance, integrated along the z-axis from each materials respective nanoparticle plumes are shown in fig. 6.14. Gold and tin spectra were recorded at 5 μs after the laser pulse with the gate width being 10% of the gate delay. Silver and aluminium spectra were integrated between 2 and 7 μs to improve signal to noise ratio. This verifies the observations from iCCD images that there is a large variation in plume emission for each material. At this time, the silver plume is the coolest at 1720 K, this suggests that the weaker emission observed in iCCD imaging may not be due to the amount of material in its nanoparticle plume. In each case, the emission spectrum has been fitted using equation 6.5 and accounting for each materials emissivity. The emissivity of a 5 nm radius nanoparticle for each material is given in figure 6.15. For gold, we compare the nanoparticle emissivity calculated for optical constants at different temperatures [90, 91]. From this, we observe that the plasmon resonance feature has a strong temperature dependence. For aluminium, the plasmon resonance feature is not observed in the visible region and we see a much lower dependence on the emissivity with temperature [92]. The accuracy of the optical constants, and hence, the emissivity of the materials in the high temperature regime is a source of error in the calculated value of temperature and amount of material from optical emission and absorption measurements.

Figure 6.16 shows the transmission and corresponding density×length product for each material at 100 μm from the plume measured using the single wavelength absorption probe. In contrast to optical emission measurements the absorption in the silver nanoparticle plume is approximately equal to that of gold. Gold is more emissive at 532 nm and hence results in a smaller density×length product.

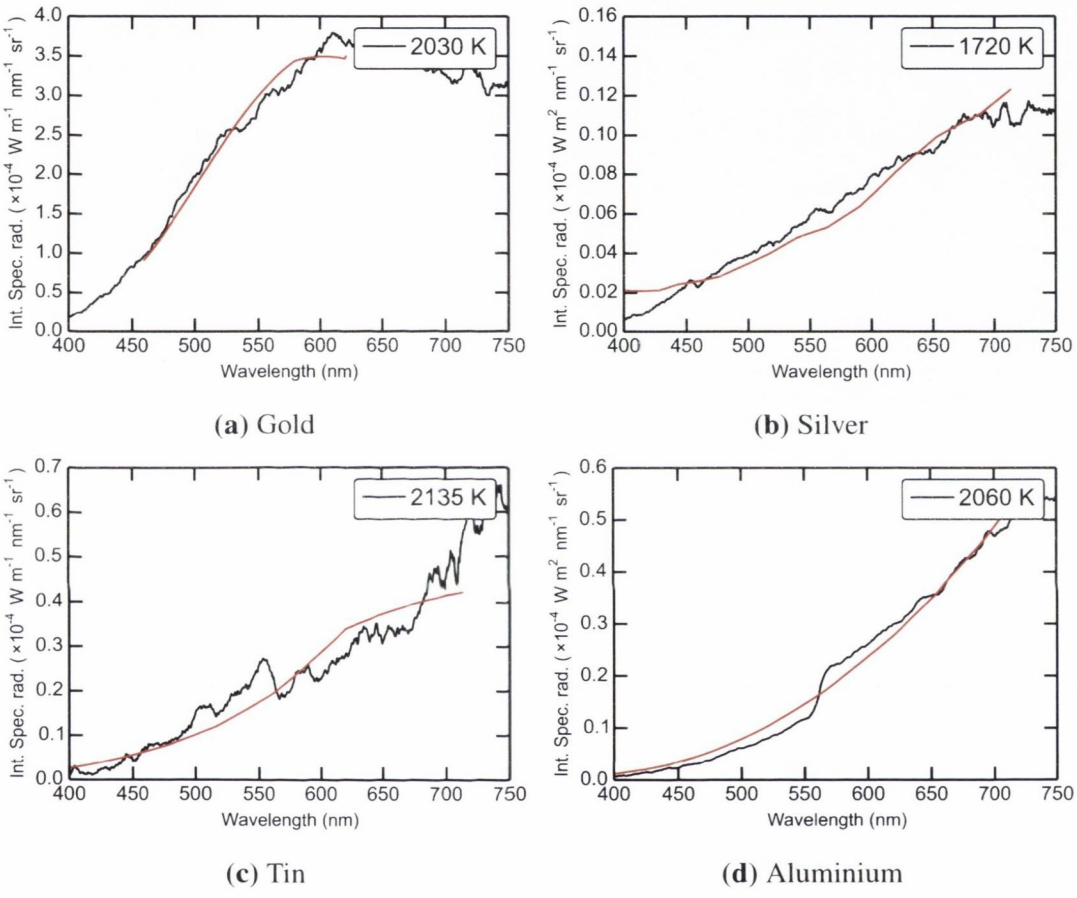

(a) Gold **(b)** Silver

(c) Tin **(d)** Aluminium

Figure 6.14: Nanoparticle plume integrated spectral emission recorded for (a) gold (b) silver, (c) tin and (d) aluminium. Gold and tin spectra were recorded at 5 μs after the laser pulse with a 10% gate width. Silver and aluminium spectra were integrated between 2 and 7 μs to improve signal to noise ratio.

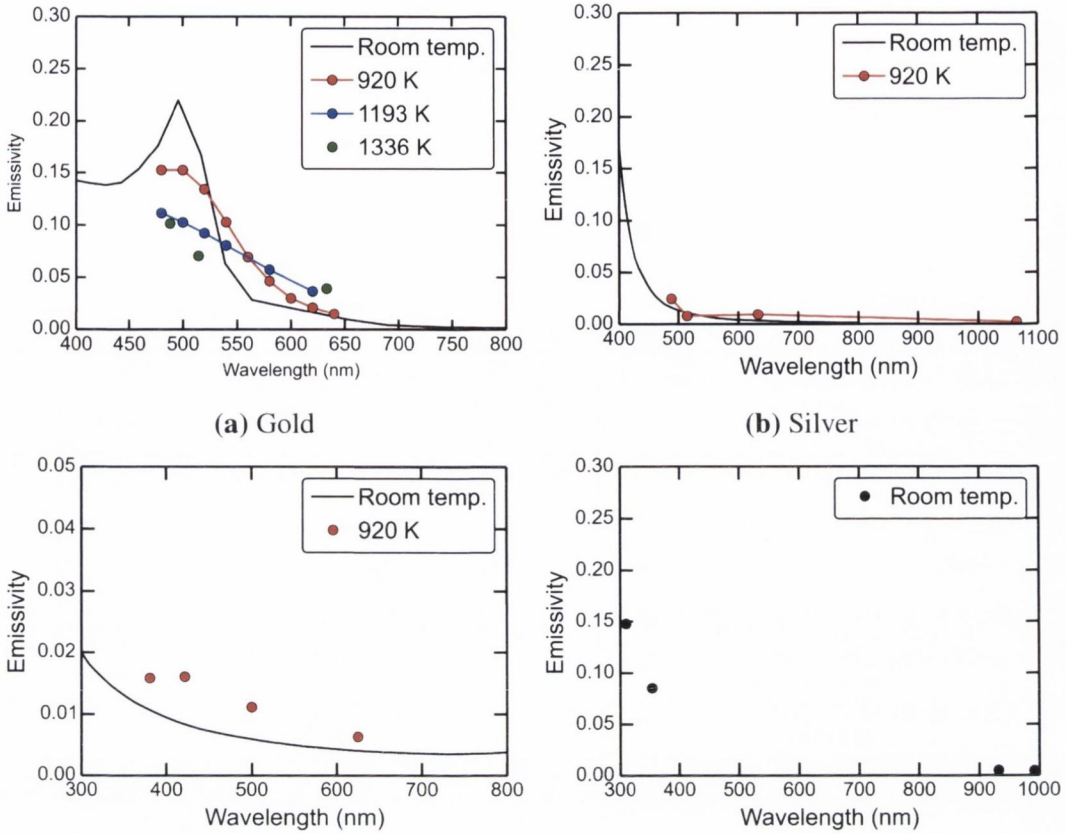

(a) Gold **(b)** Silver

(c) Aluminium **(d)** Tin

Figure 6.15: Calculated emissivities of a nanoparticle for (a) gold (b) silver, (c) aluminium and (d) tin with a radius of 5 nm.

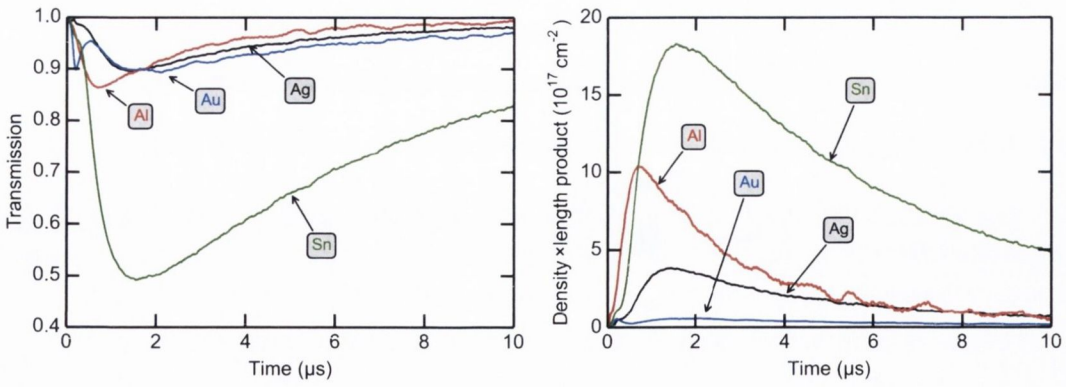

(a) Transmission **(b)** Density×length

Figure 6.16: Comparison of single wavelength absorption of silver, aluminium, gold and tin in (a) transmission and (b) corresponding density×length product recorded at 200 μm from the target.

From table 6.3, it is clear that there is a discrepancy between the emission, absorption and total number of atoms ablated. Fitting the nanoparticle spectral emission with a blackbody-like function, the estimate of the total number of atoms in the nanoparticle plume gives reasonable values, ranging from 50-85% of the atoms ablated. For silver, tin and aluminium, the amount of material in the nanoparticle plume measured using optical absorption does not agree with the other measurements. The origin of this is not currently clear. For tin, this may be partly due to limited availability of optical constants in the visible spectral region. However, the same reasoning does not apply to silver and aluminium. To address this, a potential future experiment would be a comparison of time- and space- resolved emission and absorption measurements.

Table 6.3: Comparison between the total number of atoms ablated and the *in situ* measurements of the number of atoms in the nanoparticle plume.

	Gold	Silver	Aluminium	Tin
Atoms ablated	7.4×10^{13}	3.9×10^{13}	6.4×10^{13}	1.2×10^{14}
NP plume emission	6×10^{13}	2×10^{13}	4.2×10^{13}	8×10^{13}
NP plume absorption	6×10^{13}	2×10^{14}	6×10^{14}	3.5×10^{15}

6.5 Conclusions

Initially, we focused on characterising the gold nanoparticle plume in both emission and absorption. From this, we calculated the time dependent cooling rate of the gold nanoparticle plume. Studying the rate of change of the plume temperature we have come to the conclusion that, for gold, from 100 ns - 3 μs, the plume cools primarily by evaporation. The total number of atoms in the gold nanoparticle plume was found by fitting the plume spectral emission to a blackbody function, modified for the nanoparticle spectral emissivity and found to be 6×10^{13}.

No electrostatic charge was detected from the nanoparticle plume on the Langmuir ion probe. This led to the development of the laser absorption probe method to perform an *in situ*, absolutely calibrated measurement of the nanoparticle plume dynamics. Unlike emission measurements, the ability to measure the plume by absorption is not dependent on temperature. ICCD imaging can give the relative distribution of material in the nanoparticle plume, this assumes the plume is optically thin and can be approximated as having a single temperature. For the experimental conditions and materials studied this holds true, the single wavelength absorption probe shows that for the gold nanoparticle plume at 532 nm the minimum transmission is $\approx 90\%$.

A method was developed to calculate the total amount of material in the nanoparticle plume by fitting the plume spectral radiance with a blackbody-like function. Table 6.4 summarises some of the results from the previous chapters. For each material, the number of atoms ablated was on the order of 10^{13} atoms. An interesting feature observed in the spectral emission measurements was that the silver and aluminium plumes radiated with a lower intensity. Comparing gold and silver integrated spectral radiance (fig. 6.14), the gold emission is $\approx$25 times greater than for silver. The amount of emitted light is determined by three factors: material emissivity, plume temperature and number of atoms in the plume. The gold emissivity, intensity change due to temperature and the amount of material is greater than that for silver by a factor of 5, 1.2 and 3 respectively. From this, we deduce that the reduced radiance recorded by iCCD/Spectroscopy measurements is due to the combination of factors but primarily influenced by the reduced emissivity of silver nanoparticles and the number of atoms in the nanoparticle plume.

In chapter 5, we measured the amount of atoms in the silver atomic plume by space- and time- resolved spectroscopy to be 1×10^{13}. Comparing these measurements in table 6.4, this agrees quite well with the total number of atoms ablated, 3.9×10^{13} and the total number of atoms in the nanoparticle plume, 2×10^{3}.

Table 6.4: Material inventory for fs ablation of different materials.

	Gold	Silver	Aluminium	Tin
Atoms ablated	7.4×10^{13}	3.9×10^{13}	6.4×10^{13}	1.2×10^{14}
Plasma ions	4×10^{11}	7.5×10^{11}	4×10^{11}	3×10^{11}
Deposition	3.7×10^{13}	5.7×10^{13}	1.4×10^{13}	6.7×10^{13}
NP plume (Optical emission)	6×10^{13}	2×10^{13}	4.2×10^{13}	8×10^{13}

Chapter 7

Femtosecond ablation plume dynamics in background gas

In this chapter, we will describe an investigation into plume expansion in a background gas. The analysis is currently on going but the main results will be presented. Laser ablation plume dynamics in the presence of a background gas is of much interest and has been the focus of numerous studies for both nanosecond and femtosecond laser produced plasmas [93–97]. Ablation into a background gas is already utilized in a number of applications. In pulsed laser deposition, reactive gases can be used for the production of transition metal nitride films. Nitride films are of great interest due to their strength, durability and useful optical, electronic and magnetic properties [98]. There are several reasons why PLD is of interest in nitride film growth; 1. it is a relatively simple and comparatively inexpensive thin film growth technique and 2. for some materials, it has been shown that PLD leads to good stoichiometric growth of the thin film, which is important for the growth of complex materials. Inert ambient gases have also been widely used as part of the PLD process [99]. Afonso et. al. studied growth of copper nanocrystals in argon at pressures ranging from vacuum up until 1.33×10^{-1} mbar and concluded that at pressures $\geq 7 \times 10^{-2}$ mbar anisotropy is higher and develops earlier than for films grown in vacuum, this is possibly detrimental for the production of optical elements but has potential for catalytic applications. Laser produced plasmas have been used extensively for material characterisation; laser-induced breakdown spectroscopy (LIBS) and integrated into an inductively coupled plasma mass spectrometry (ICP-MS) system [100–104]. LIBS is considered to be a non-destructive technique as only a small amount of material is removed in the ablation process, this can be carried out in both background gas and vacuum [101, 105]. Nanosecond LIBS is more common and commercial systems are available [106], however, there has been some recent studies into the feasibility of fs-LIBS [107]. Laser ablation ICP-MS (LA-ICP-MS) is an analytical technique for determining the chemical and isotropic composition of solid samples. A tightly focused laser is used to vaporise a small amount of material from a target into

gas flow. The gas flow carries the material to the ICP-MS for analysis. Both material characterisation techniques are known for their high sensitivity and in some cases can have detection sensitivity up to parts per billion.

The same setup described in chapter 4 was used, the ablation was carried out using 130 fs, 800 nm Coherent Legend Elite with a peak fluence of 1.6 J cm^{-2}. The background gas pressure was measured using a Hastings dual vacuum gauge (HPM-2002-OBE) containing a Pirani and an piezoresistive direct force sensor to give a measurement range from 1.3×10^{-4} to 1.3×10^{3} mbar. The plume expansion was studied in argon and helium atmospheres at pressures of 1, 10 and 1000 mbar and the results compared with vacuum measurements (chapters 5 and 6). The background gas pressures were chosen to cover a wide pressure range, laser ablation conducted in atmospheric pressure is of interest for high pressure depositions and material characterisation (LIBS, LA-ICP-MS). Helium and argon were chosen as the gases of interest to explore the plume dynamics in an inert atmosphere of a light and relatively heavy background gas. In order to achieve high gas purity in the chamber, the gas line was flushed and the chamber initially pumped down to a vacuum ($\leq 10^{-4}$ mbar). As before, we will mainly focus on gold as a material of interest, but will also discuss the effect of gas confinement on other materials (silver, aluminium, tin).

Figure 7.1 shows the expansion of gold femtosecond plumes in vacuum and various pressures of argon. As discussed in chapter 6, the gold atomic emission is relatively weak compared to the nanoparticle plume emission. At higher gas pressures there is a stronger influence from the confining gas and this results in complex hydrodynamic changes in the plume shape. For 10 mbar, at 500 ns and 1 μs after the laser pulse the atomic plume is still observable and is partially confined by the background gas producing a peak of emission near the plume front. The nanoparticle plume expansion is only slightly impeded at this background gas pressure, this could be due to the nanoparticle plume having a much greater mass per particle. At 100 mbar, the atomic plume is further confined, exhibits strong lateral confinement and undergoes strong de-acceleration due to the increasing pressure of the gas build up on the plume-gas interface. In the case of 100 and 1000 mbar, there is sharpening of the nanoparticle plume. Farid et al. has previously reported that for femtosecond laser ablation of copper in various pressures of air [108]. At 1000 mbar, early in time, the atomic plume is further confined and remains close to the target due to strong confinement. From 1 μs and 5 μs we observe two distinct plume components. It is possible that the second component is fast nanoparticles from the front of the nanoparticle plume or material from the atomic plume, this will be discussed and analysed in more detail later using space-resolved optical emission

spectroscopy.

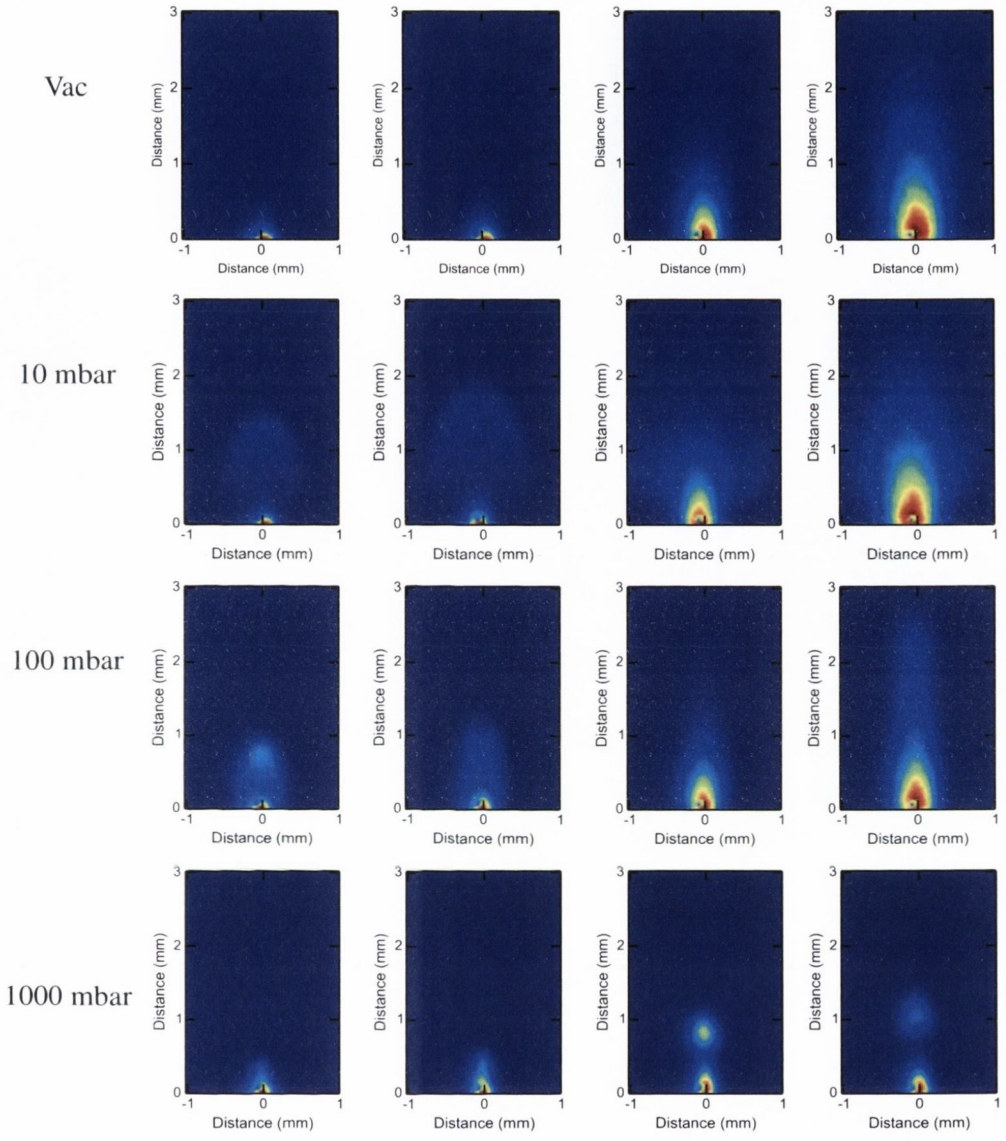

Figure 7.1: Time resolved iCCD images showing the evolution of the gold plume expansion in vacuum and 10, 100 and 1000 mbar of argon.

Figure 7.2 shows the influence of helium on the gold plume expansion. As with the case of argon, we observe the effect of confinement of the atomic plume, however, this effect is only appreciable at 100 mbar and is comparable to the effect observed in 10 mbar of argon. Plume sharpening at higher pressures is still observed, but less pronounced which shows an influence of not just the pressure but the atomic mass of the confining gas.

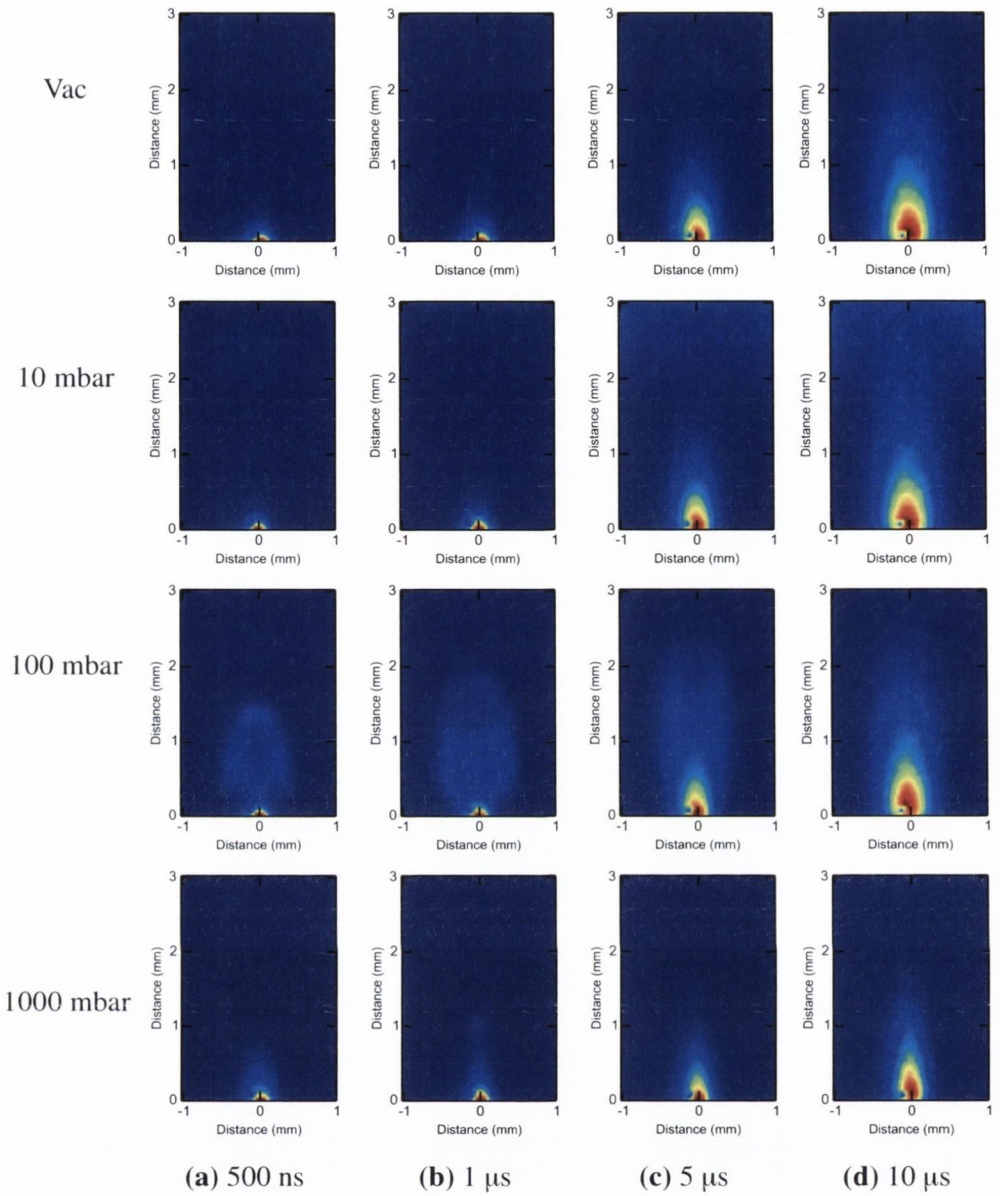

Figure 7.2: Time resolved iCCD images showing the evolution of the gold plume expansion in vacuum and 10, 100 and 1000 mbar of helium.

It is clear from figs. 7.1 and 7.2 that under the influence of the background gas the plume decelerates. By approximating the plume front position as when the signal is at 10% of its peak value we can measure the position of the plume front versus time and hence study the deceleration caused by background gas confinement. We can describe the position of the plume front by using a simple model based on the balance between the plume linear momentum variation and the external pressure applied by the background gas [96]. For the atomic plume, the model assumes the plasma undergoes a hemispherical expansion with the background gas swept up forming a thin hemispherical layer on the plume front. The equations of motion are

$$\frac{d}{dt}\left[\left(M_a + \frac{2}{3}\pi\rho_g R^3\right)u_a\right] = -2\pi R^2 p_g, \qquad \frac{dR}{dt} = u_a(t) \tag{7.1}$$

where R, u_a, M_a are the plume radius, velocity and total mass respectively. The background gas is described by its density, ρ_g and pressure, p_g. In order to solve this model, the initial conditions are $R(t = 0) = 0$ and $u_a(t = 0) = u_{a,0}$, where $u_{a,0}$ is the plume velocity in vacuum. The experimentally measured atomic plume velocity and results of the fitting procedure in different background gas pressures of helium and argon are shown in fig. 7.3. Also shown on each plot is the measurement and fitting of the plume expansion in vacuum and the linear fit used to estimate the velocity which was found to be $8 \times 10^3\,\mathrm{m\,s^{-1}}$.

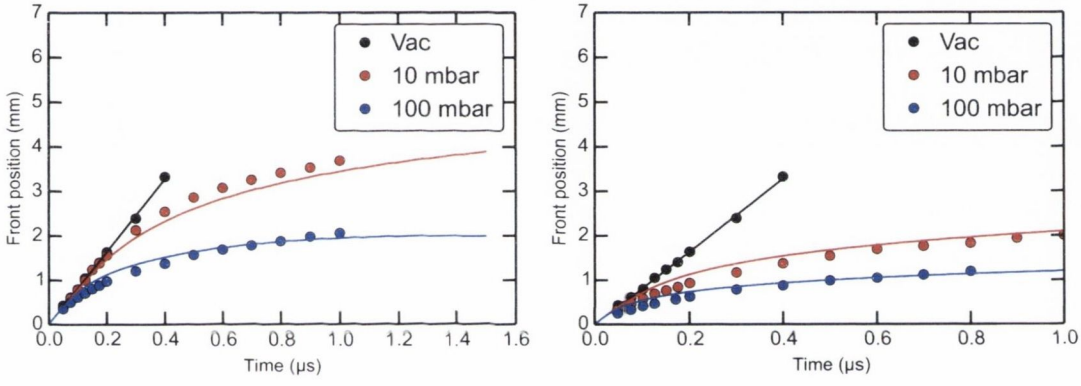

(a) Helium **(b)** Argon

Figure 7.3: Position-time plots of the gold atomic plume front position in (a) Helium and (b) Argon at different gas pressures fitted using equation 7.1.

This model adequately describes the influence of background gas on the plume velocity at 10 and 100 mbar. Experimental values taken at atmospheric pressure are not shown, at high pressures the background gas has a stronger confinement effect on the plasma plume and in the observation direction both plumes appear to overlap in space and hence we are unable to clearly distinguish between the nanoparticle and atomic plumes with iCCD imaging. From the fitting procedure, described by equation 7.1, we obtain an estimate for the mass of the plume to be 2.9×10^{-11} kg or 9×10^{13} atoms. This value does not agree well with the total number of atoms ablated, 7.4×10^{13}. However, this model assumes a hemispherical expansion, which as seen in fig. 7.1, it is forward directed. This will result in an overestimation of the total amount of material in the plume.

Figure 7.4 shows an iCCD image recorded of a gold ablation plume at 500 ns in 100 mbar of helium. In this case we have plotted the intensity on a log scale to highlight the

internal structure observed in the plasma plume which is not present in a low pressure or vacuum environment. This structure suggests more complex hydrodynamic processes involved that cannot be described by this simple model and are out of the scope of this thesis, though has potential for future work as would enhance the understanding of plume dynamics in high pressure background gases.

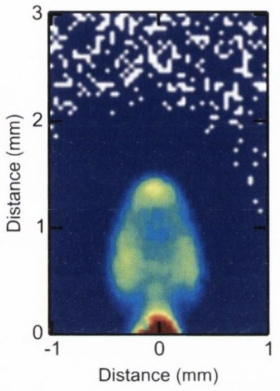

Figure 7.4: ICCD image of gold femtosecond ablation plumes recorded 500 ns after the laser pulse in 100 mbar of helium.

Figure 7.5 shows an array of images showing the plume space resolved spectral emission as a function time and background gas pressure of argon. In 10 mbar, the atomic plume, observed by discrete line emission, can be seen to expand away from the target. In this case, the plume appears to disconnect from the target as no observable line emission is seen close to the target surface. In 100 mbar, the atomic plume is confined as it can be clearly seen that 1 μs after the laser pulse the discrete line emission has not propagated as far as observed in 10 mbar, which is consistent with our assessment from iCCD imaging. One of the advantages of space resolved spectroscopy over the iCCD imaging is that we can assess the extent of the overlap between the atomic and nanoparticle plumes which are clearly distinguishable by their different emission features. At 1000 mbar, strong confinement occurs, from iCCD imaging it is difficult to determine the influence of background gas pressure on the nanoparticle plume velocity. Due to the strong confinement, at this pressure, the emission observed from the atomic plume remains close to the target and overlaps the nanoparticle plume in space. An interesting feature at this high pressure is that we observe two distinct broad continua separated in space at later times. There are a number of possible causes for this; condensation of the atomic plume into nanoparticles or a splitting of the nanoparticle plume resulting in a double peak structure. This feature is also clearly evident from iCCD imaging (fig. 7.1) and will be discussed in more detail later in this chapter.

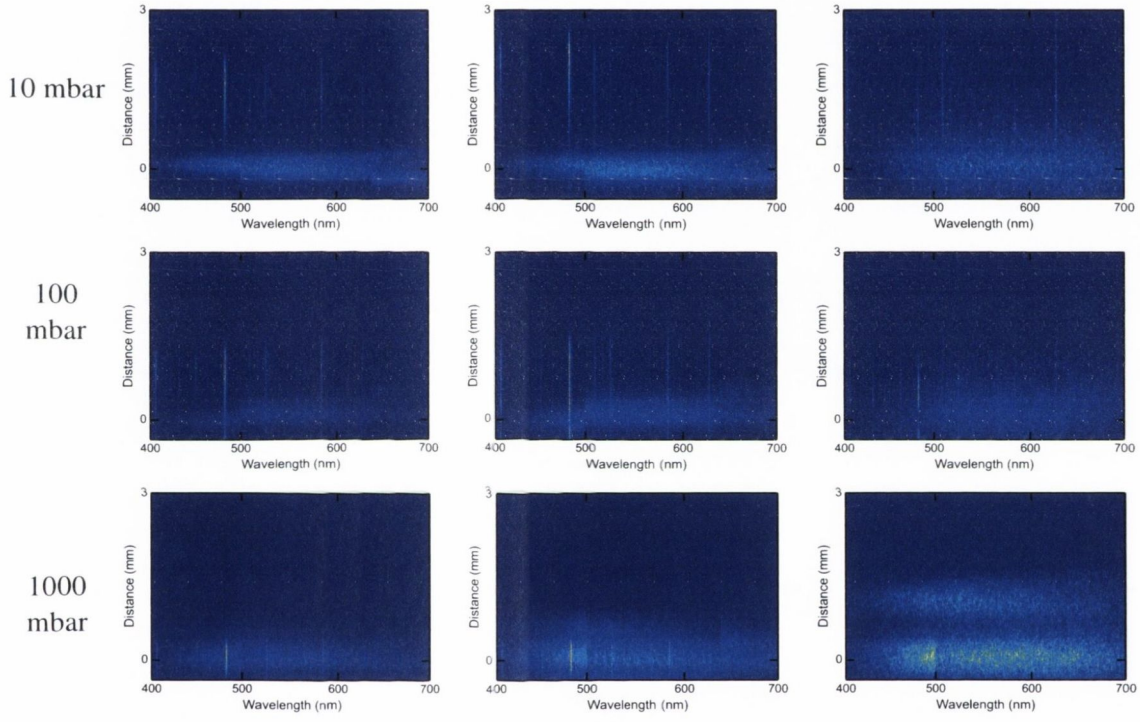

(a) 600 ns **(b)** 1 μs **(c)** 5 μs

Figure 7.5: Time and space resolved spectroscopy images sequence comparing gold plume optical emission in argon at pressures of 10, 100 and 1000 mbar.

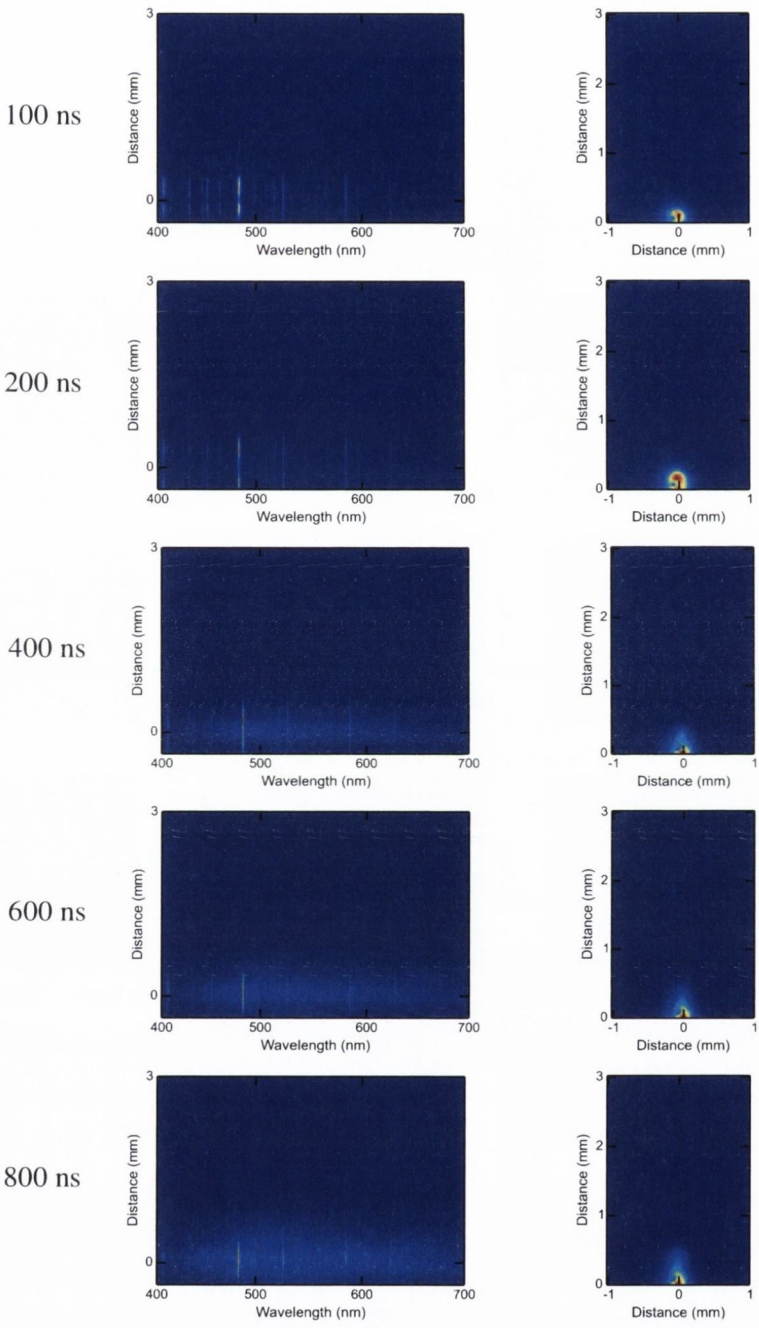

Figure 7.6: Time and space resolved spectroscopy and iCCD images images sequence comparing gold plume optical emission in argon at 1000 mbar from 100 - 800 ns.

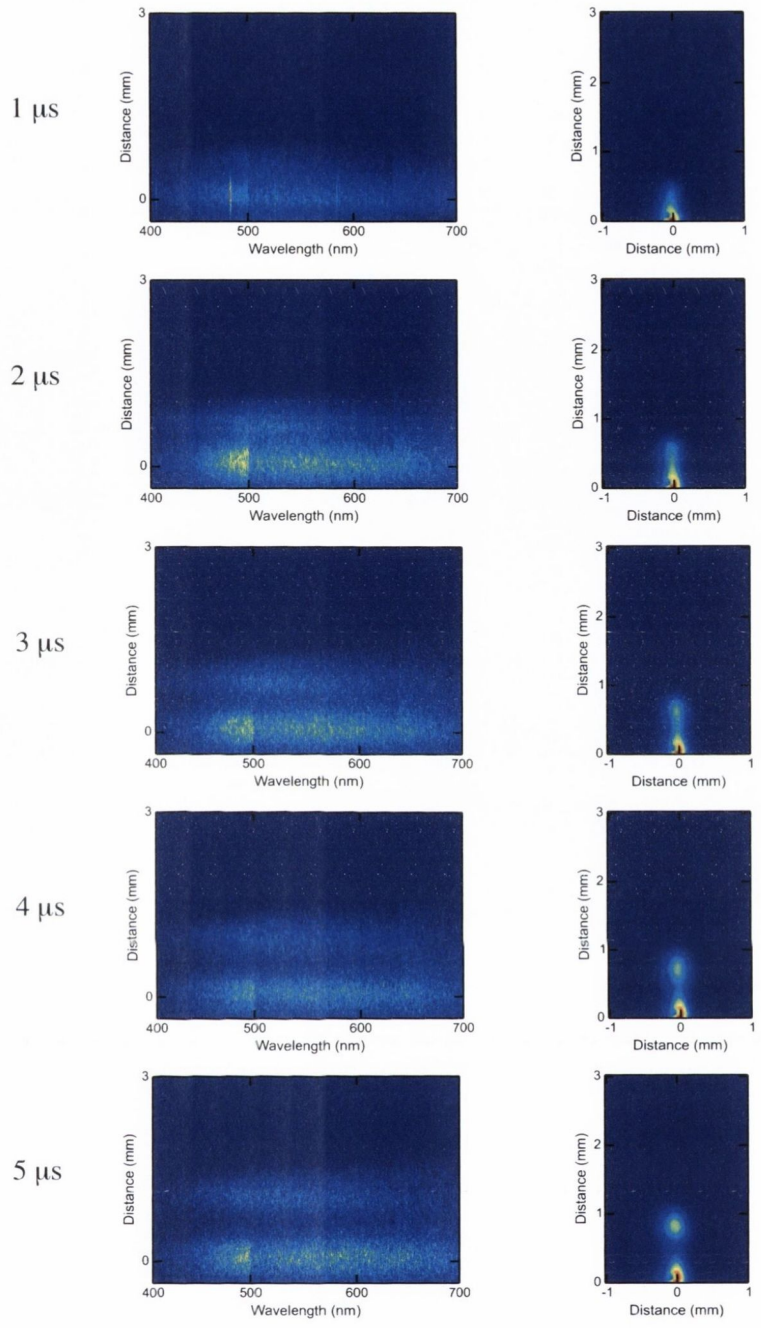

Figure 7.7: Time and space resolved spectroscopy and iCCD images images sequence comparing gold plume optical emission in argon at 1000 mbar from 1 - 5 μs.

Figures 7.6 and 7.7 shows the temporal evolution of the gold nanoparticle plume in 1000 mbar of argon using space resolved spectroscopy and iCCD imaging. Early in time (100 - 800 ns), the atomic and nanoparticle spectral line emission is clearly observable. The plasma plume is strongly confined and remains close to the target surface. At 800 ns, the broad continuum has expanded further from the target than the line emission. At later times, shown in fig. 7.7, two distinct emission peaks are observed. From

iCCD images we can see the two peaks remain connected. This feature is either due to condensation of the atomic plume resulting in a change from atomic line emission to a broad continuum, or a fast component of the nanoparticle plume. To address this, multiple spectral lineouts are taken across the emission spectra at 4 μs in the regions shown in fig 7.8. Figure 7.8 shows that the maximum plume temperature occurs at the fast peak position, while the coolest region resides between the two regions of peak emission. The fast peak temperature is ≈500 K greater than the average temperature of the nanoparticle plume in vacuum. This may be due to condensation of the atomic material to form nanoparticles, however it is also possible that the high temperature is as a result of plume confinement. As mentioned at the start of the chapter that this work is ongoing and further analysis involving the plume velocity profiles is required to confirm this hypothesis.

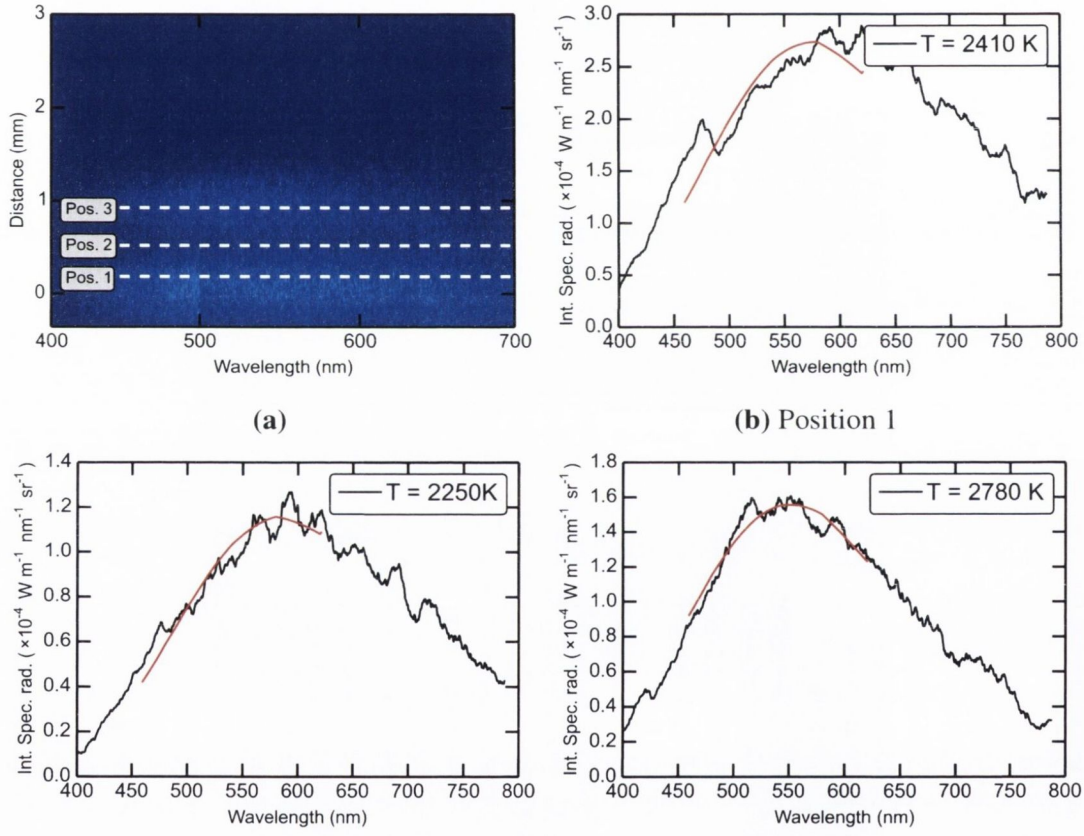

(a)

(b) Position 1

(c) Position 2

(d) Position 3

Figure 7.8: (a) Space resolved spectral emission from femtosecond laser ablated gold in 1000 mbar of argon 4 μs after the laser pulse showing two distinct plume components (b-d). Spectral lineouts at three different positions are indicated in (a).

The nanoparticle cooling rate may be influenced by the confining background gas through nanoparticles-gas collisions. Figure 7.9 shows the variation of nanoparticle plume temperature versus time in vacuum and background gas (helium, argon) at various pressures. Small variation is observed in the rate of change of the plume temperature with pressure and background gas. However, it is unclear whether this trend is due to experimental uncertainty or the interaction between the nanoparticles and background gas.

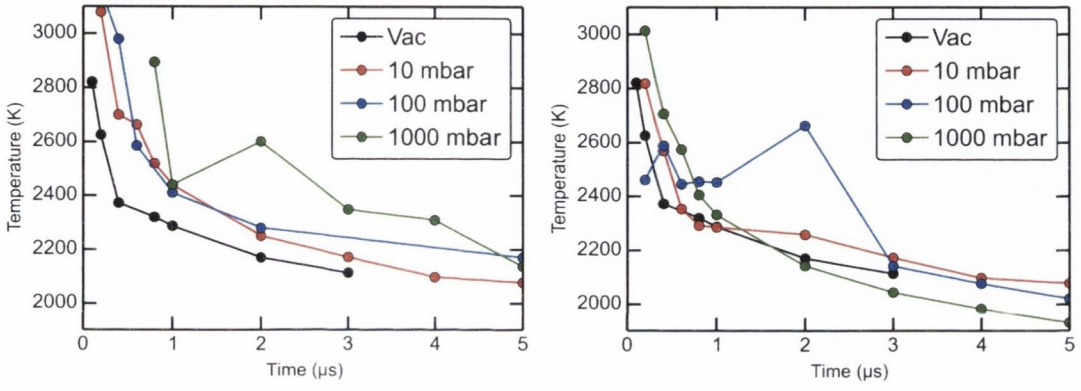

(a) Argon **(b)** Helium

Figure 7.9: Temporal variation of the gold nanoparticle plume temperature in (a) argon and (b) helium.

Figure 7.10 shows the single wavelength optical absorption measurements recorded in vacuum and various pressures of argon at 3 mm from the target. An increase in the peak absorption is observed at higher pressures due to the confinement of the material not only slowing the plume expansion, but also narrowing the plume aspect ratio and results in the formation of multiple peaks. Figure 7.10 highlights an advantage of absorption measurements as we are able to study the plume milliseconds after the laser pulse. At late times the plume would be too cool to result in detectable optical emission.

Figures 7.11 and 7.12 show the expansion of the aluminium plumes into helium and argon at 10, 100 and 1000 mbar. In vacuum, the atomic plume is not visible due to the relative intensity of each plume component and the times the images were recorded. At 10 mbar, the atomic plume is confined and clearly visible. The expansion of the aluminium atomic plume is confined more than for the gold atomic plume at the same pressure. It is clear from these images and those of gold that the plume behaviour in high pressure background gas is quite complex and warrants further investigation.

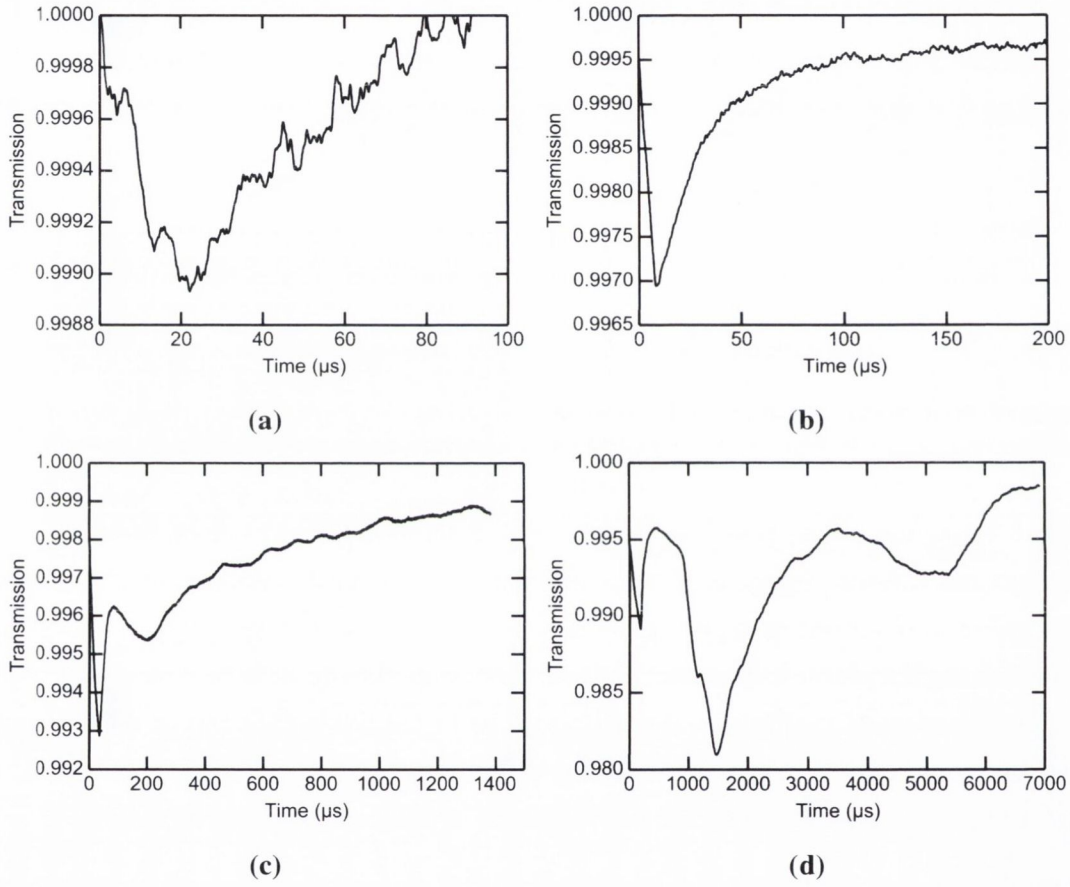

Figure 7.10: Optical absorption measurements of the gold NP plume, recorded at 3 mm in (a) vacuum, and in argon with a pressure of (b) 10 mbar , (c) 100 mbar, (d) 1000 mbar.

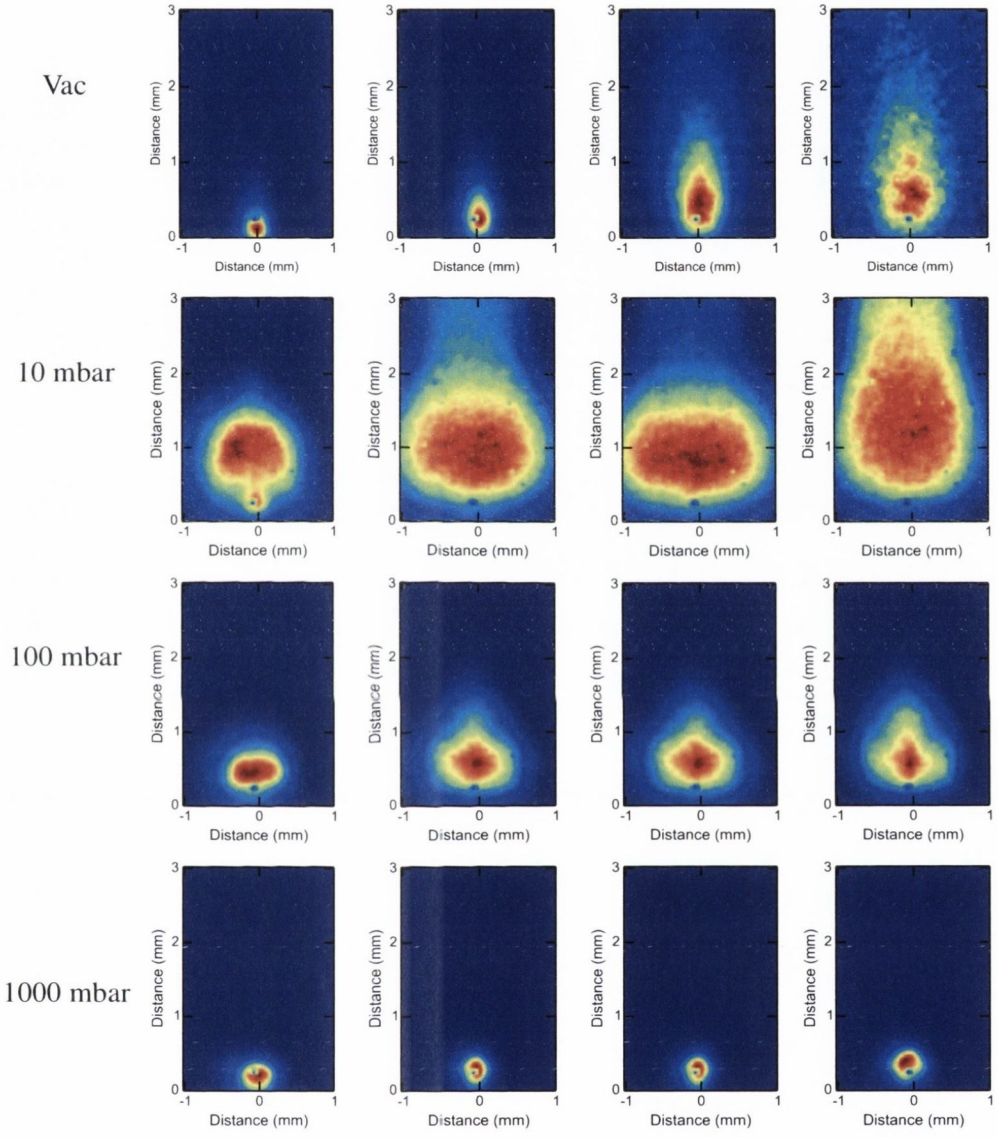

Figure 7.11: Time resolved iCCD images showing the evolution of the aluminium plume expansion in vacuum and 10, 100 and 1000 mbar of argon.

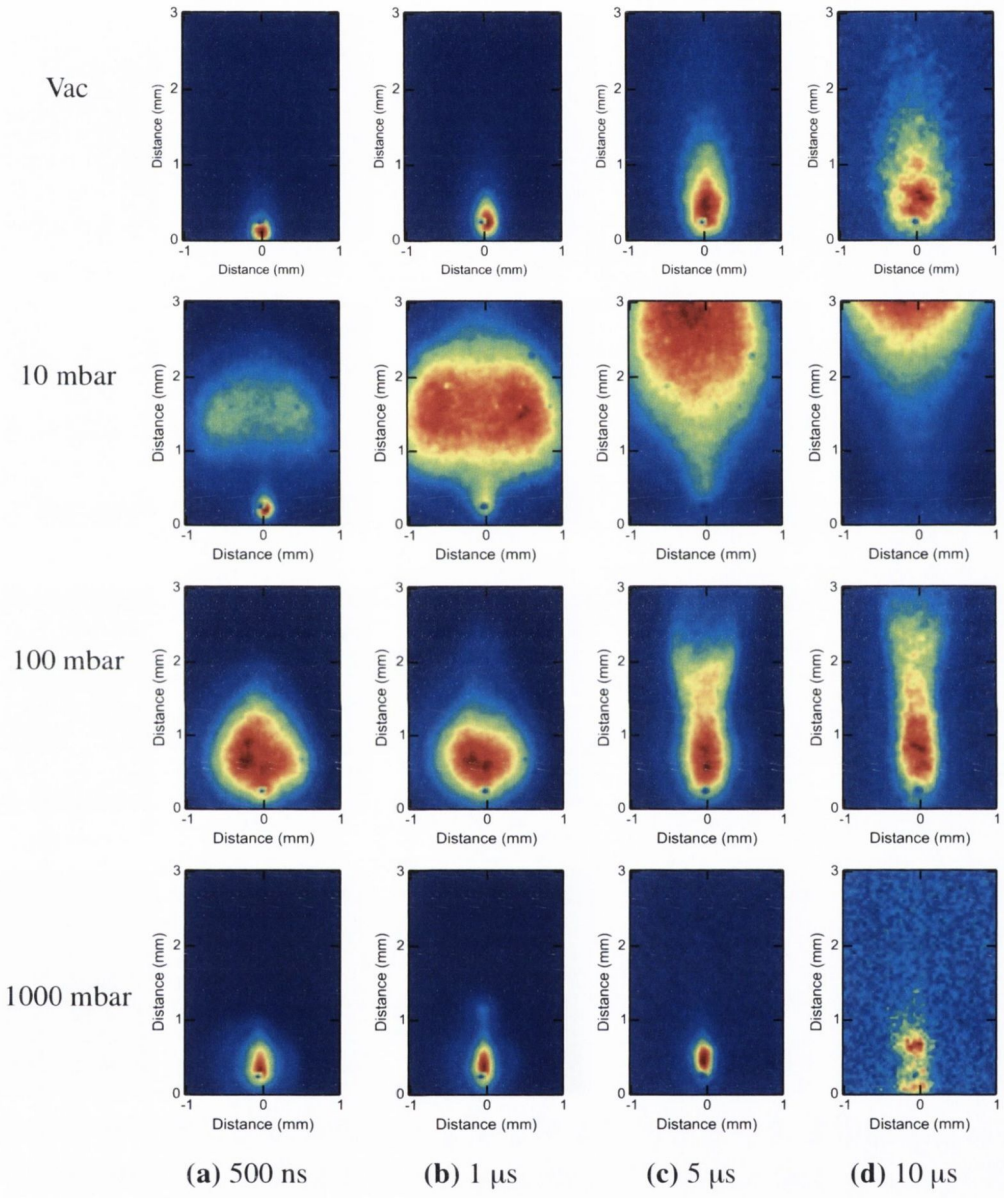

Figure 7.12: Time resolved iCCD images showing the evolution of the aluminium plume expansion in vacuum and 10, 100 and 1000 mbar of Helium.

7.1 Conclusions

In previous chapters, we characterised the femtosecond laser ablated materials in vacuum and expanded on the application and understanding of current diagnostic methods to study each plume component in detail. This chapter expands on this study to look at the effect of background gas confinement on the plume.

At low pressures, the background gas exhibits stronger confinement on the plasma plume than the nanoparticle plume component. In a similar gas environment, the aluminium plasma plume undergoes greater confinement than the gold plasma plume. This is due to gold having a much larger atomic mass. With increasing background gas pressure, further confinement occurs and it becomes harder to distinguish the two plume components using iCCD imaging. For gold in 1000 mbar of argon, using time- and space- resolved spectroscopy, the atomic line emission is observed to overlap the nanoparticle plume emission. Two distinct components emerge at later times (>1 μs), the origin of which is not currently well understood. The fast component may be due to re-condensed plasma but this has not been proven and is of interest for further analysis.

With plume confinement, the plumes remain relatively dense at later times, however cooling occurs at a similar rate as vacuum. In this case, it is advantageous to study the plume using absorption measurements. As mentioned previously, absorption measurements do not rely on the material having a high temperature which is a requirement for emission measurements. Multiple peaks were also observed in single wavelength absorption measurements and resolved on time-scales on the order of milliseconds.

Chapter 8

Conclusions and future work

8.1 Conclusions

This work has focused primarily on study the ablation plume dynamics of femtosecond laser ablated metals. The main experimental setup was designed to include a wide range of measurement techniques to characterise each aspect of the plumes. Femtosecond laser ablation of metals is of interest due to its distinctive ablation process and numerous applications. The study of femtosecond ablation in vacuum divided into three sections; 1. target irradiation, material removal and deposition, 2. the fast, atomic plume and 3. the slower, nanoparticle plume component.

The target irradiation was characterised by measuring the distribution of laser fluence across the beam spot by using a CCD camera. This is the ideal method of characterising the focused beam spot. While limited by the cameras finite pixel size, unlike knife-edge measurements, this method does make assumptions on the beam shape to calculate the spot dimensions. For ablation of gold with a 550 µJ, 130 fs laser pulse, 2.4×10^{-11} kg atoms were ablated per pulse.

The fast atomic plume has been successfully characterised using a range of characterisation methods; Langmuir ion probe, iCCD imaging, space- and time- resolved spectroscopy. From optical measurements, the relative intensity between the atomic and nanoparticle plume varies strongly with material. However the difference in the plume emission intensity is not reflected in the differences in the number of ions in the plasma plume determined by rotational Langmuir ion probe measurements.

Analysis of the nanoparticle plume was conducted with two main aims; to further the understanding of the optical emission and absorption of the nanoparticle plume and to determine the amount of material in the plume using absolutely calibrated spectroscopy. This was achieved by fitting the nanoparticle plume continuum emission by accounting for the spectral emissivity of the nanoparticles. Previously, metallic nanoparticle emissivities were assumed to be proportional to $1/\lambda$. This holds true if the optical constants

can be approximated as wavelength independent over the emission region. As a result of fitting the spectral emission, the plume temperature and mass were determined. The gold nanoparticle plume was composed of approximately 85% of the ablated material. A number of significant differences were noticed in our study of different metals. The silver nanoparticle plume was observed as being less emissive. We found that for silver, the nanoparticle plume was contained only 50% of the ablated material. The lower emission of the silver nanoparticle plume was also due to a combination of its lower plume temperature and nanoparticle emissivity.

Lastly, the main diagnostic methods were applied to study the plume dynamics in various background gases and pressures. It is clear that choice of the type of gas and pressure influences the plume expansion. The atomic plume, while initially has a much higher velocity than the nanoparticle plume, undergoes greater deceleration and can be overtaken by the nanoparticle plume in space. With increasing gas pressure the plume expansion changes shape and becomes more forward directed. At atmospheric pressure, two distinct plume components are observed, each having continuum spectral emission characteristic of hot nanoparticle emission. This is most likely due to condensation of the confined atomic plume to form nanoparticles but requires further investigation.

8.1.1 Future work

In this work, some experimental observations warrant further study to clarify their origin. It would be of interest to conduct spectral absorption measurements using a high intensity broadband light source (eg. pulsed xenon flash lamp or supercontinuum laser). Unlike emission measurements, the wavelength dependence of the plume optical absorption is only weakly dependent on temperature and hence, is only dependent on the amount of material and the optical properties of the nanoparticles. In this work, we studied the nanoparticle plume absorption at a single wavelength (532 nm) at a set position. This provides us with a temperature independent absolute measurement of the amount of material at a specific distance from the target. It would be of interest to carry out time- and space- resolved absorption spectroscopy, and spatial imaging of the plume absorption using the setup shown in fig. 8.1. By comparing emission and absorption measurements we would gain a better understanding on the optical properties, the variation of emission with temperature and how accurate this method is at modelling the nanoparticle plume optical properties. Measuring the spatial distribution of the material in absorption will also help clarify the discrepancy between the number of atoms ablated and the number of atoms in the plume estimated using the single wavelength absorption probe.

Angular resolved deposition measurements, for the most part, agreed well with the number of atoms ablated. However, silver gives the total number of atoms deposited greater than the number of atoms ablated. This is most likely due to nanoparticle extinction effects which would overestimate the amount of material deposited. While a large number of shots is used to form thick depositions to form a continuous film, the film quality has not been verified. It is of interest to study this by characterising thick nanoparticle depositions using atomic force microscopy.

In chapter 7, we studied the effect of a background gas environment on plume expansion. Previously, for nanosecond laser ablation, the ablation plume has being shown to react with the background gas to form composite materials. For example, Krishnan et al ablated a titanium target into nitrogen to form nanostructured titanium films [109]. However, in contrast to nanosecond laser ablation the nanoparticles produced by femtosecond ablation form within the target itself. Therefore, femtosecond laser ablation in a reactive gas it may be a viable method to produce core shell nanoparticles [110].

It would of be of interest to study femtosecond ablation of metal alloys or compound materials. To date, this area has been relatively unexplored. Compound materials can exhibit unique electronic and/or optical properties and femtosecond laser ablation presents as a viable method for producing nanoparticles of exotic materials.

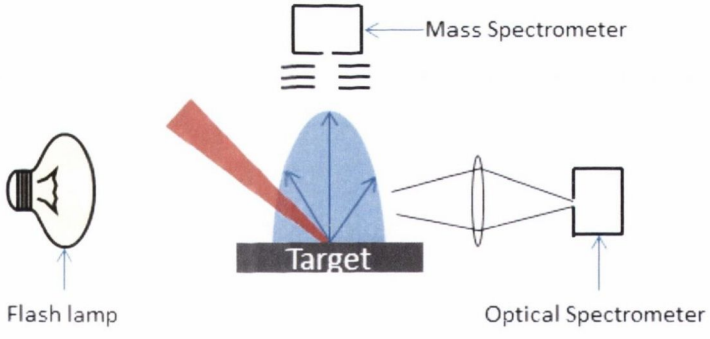

(a) Spectrally resolved optical absorption setup.

Figure 8.1: Simplified setups for optical absorption measurements.

Appendix A

Appendix

A.1 Early stage optical emission in nanosecond laser ablation

In nanosecond laser ablation, it has been observed that during the laser pulse the optical emission in the visible is a continuum [111]. After the pulse broad spectral lines emerge from the continuum and these lines narrow as the plasma expands, similar to the femtosecond produced atomic plume. It has been suggested, but not confirmed that the continuum is due to radiative recombination and bremsstrahlung emission. A broad continuum is also observed in early stage emission of femtosecond laser produced plasmas. However, there is also a component to the continuum caused by the nanoparticle plume which complicates the analysis. This section describes an experiment and analysis to clarify the origin of the continuum emission in the early stage of nanosecond laser ablation.

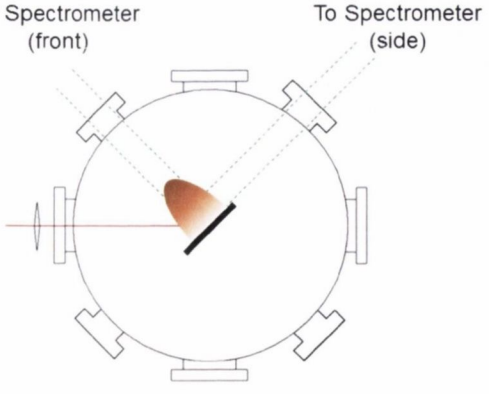

Figure A.1: Schematic diagram showing the orientation of the two spectrometer positions with respect to the plasma plume.

A simplified diagram of the experimental setup is shown in fig. A.1. An 8 ns 1.064 μm Nd:YAG laser was used to ablate a zinc target in vacuum. The angle of incidence of the laser beam was 45° and the spot size of 2.8 mm giving an average fluence of 4.1 J cm^{-2}. The target was continuously rotated to avoid drilling a hole in the target. Space- and time-resolved spectral emission normal and parallel to the target surface was measured using the setup described in section 3.2. The spectra were recorded with a gated Andor DH520 ICCD giving a minimum gate width of 8 ns and a spectral resolution of 0.8 nm.

The ablation depth per pulse was measured by firing 300 laser shots at the same position on the target and measuring the crater depth with a profilometer. From this, the average depth per pulse was found to be 22 nm, thus the number of atoms ablated per pulse was 4×10^{15}.

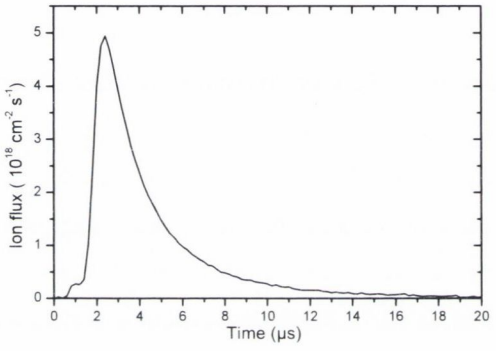

Figure A.2: Ion flux at 10.5 cm from the target surface along the target normal.

The angular distribution of the plasma flux at 10.5 cm from the target was measured using a 18 mm^2 planar Langmuir probe biased to −25 V to reject plasma electrons.

Figure A.2 shows the ion flux signal recorded by a Langmuir ion probe along the target normal. The ion velocity given by the time-of-flight at maximum ion flux (2.4 μs) is 4.4×10^6 cm s^{-1}. By rotating the probe about the ablation spot the total number of ions in the ablation plasma was determined to be 8×10^{14}.

Figure A.3 shows the spatio-temporal evolution of the plasma at 0 and 100 ns after the laser pulse. Figures A.3a and A.3b shows the emission observed parallel to the target surface, as the plasma expands away from the target surface we can see that two spatially distinct regions form: (1) a slower neutral component and (ii) a faster ionic part, which were observed to be approximately equal in length. Therefore we can treat the plasma as essentially two separate regions that we model separately using the PrismSPECT spectral modelling code. Emission observed perpendicular to the target surface axis, shown in Figs. A.3c and A.3d shows a region of nearly uniform emission.

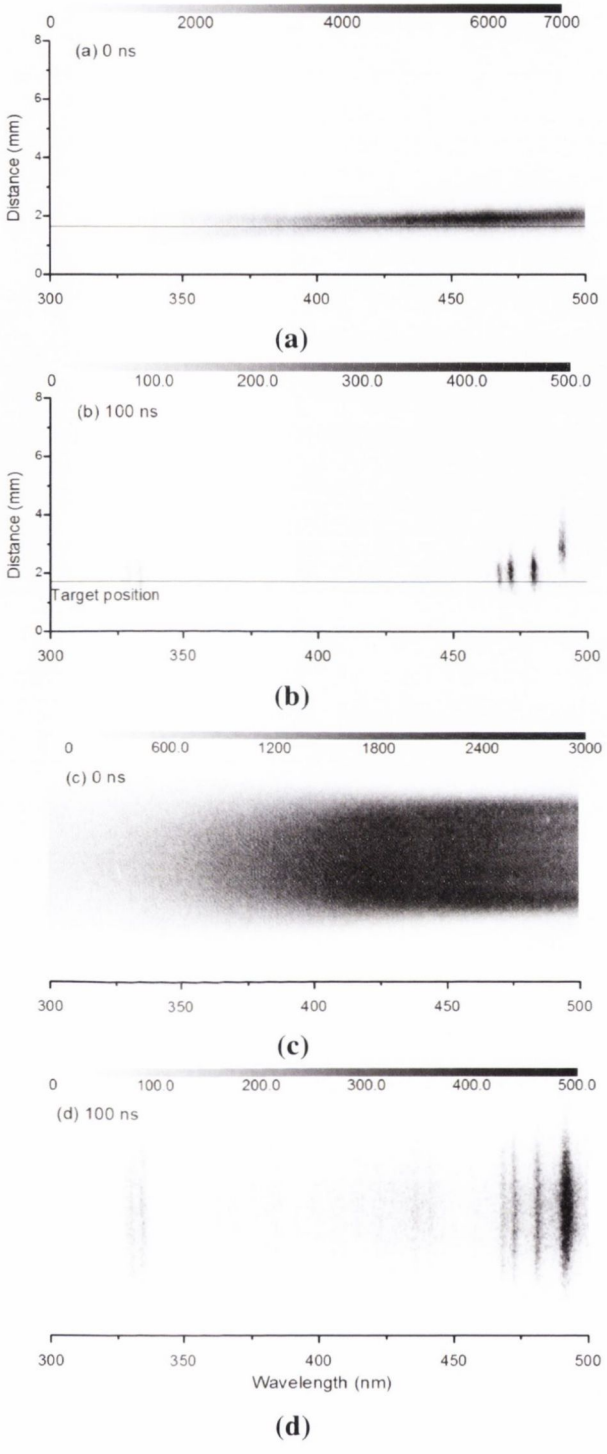

Figure A.3: Space resolved optical emission observed parallel (a) 0 ns, (b) 100 ns and perpendicular at (c) 0 ns, (d) 100 ns to the target surface.

Figure A.4 shows the temporal evolution of the spectral emission along the target normal from the zinc laser produced plasma. The first panel A.4a, shows the spectrum in the interval 0-8 ns, where 0 ns refers to the onset of the plasma optical emission. The spectrum is a continuum without any visible spectral lines. It is similar to that observed

by Sherrill et al. in the ablation of silver [111]. Figures A.4b, A.4c and A.4d show the spectral emission at 50, 100 and 200 ns, respectively. Quite broad lines emerge from the continuum at 50 ns, and the spectral width of these lines steadily decreases with time. Figure A.4 also shows PrismSPECT fits to the experimental spectra treating the neutral and singly ionised regions independently.

In using the emission spectra to diagnose the plasma parameters there are three aspects of the spectra which are sensitive to the plasma conditions. Firstly, the relative intensities of optically thin lines derived from upper levels which are in LTE can be used to estimate the electron temperature, kT_e. Secondly, it may be possible to use Stark broadening of optically thin lines to determine the electron density. Thirdly, the absolute intensity of the overall spectrum is related to the plasma density, temperature and dimensions. Thus, it is clear that accurate assessment of optical opacity is critical to reliable application of plasma diagnosis by spectroscopy. By using the PrismSPECT spectral synthesis code, the conditions and dimensions in the model plasma can be varied to optimise the fit to the measured spectrum.

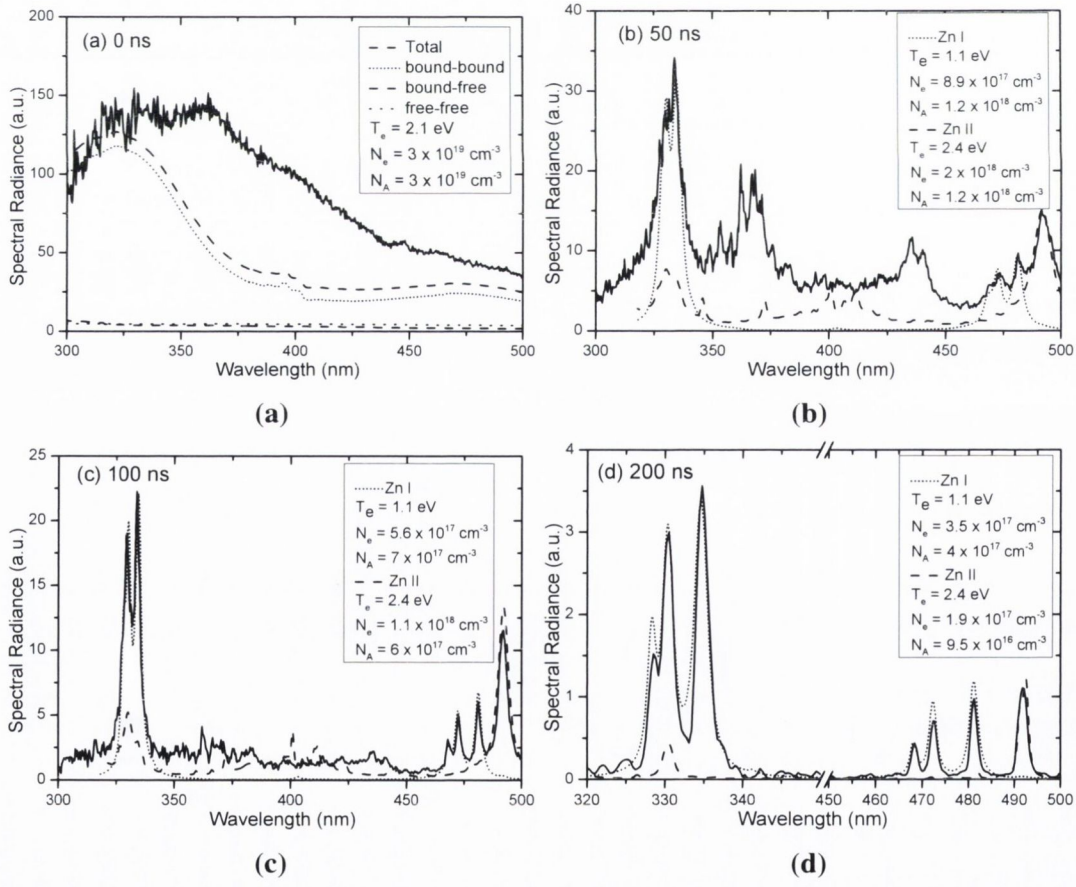

Figure A.4: Optical emission of zinc plasma recorded at (a) 0 ns, (b) 50 ns, (c) 100 ns, (d) 200 ns. Spectra also shows PrismSPECT fitting.

Figure A.4 shows the temporal evolution of the plasma as observed along the target normal from 0 - 200 ns (Figs. A.4a-A.4d) after the laser pulse. In figure A.4d, 200 ns after the laser pulse we observe well separated spectral lines. The main radiative transitions in the spectral region of interest were taken from PrismSPECT and are summarised in Table A.1 and shown on the energy level diagram in fig. A.5. The triplet of lines at 328.2 nm, 330.3 nm and 334.5 nm are mainly due to Zn I 4s4d $3D_{1,2,3}$ - 4s4p $^3P_{2,1,0}$. There is a second triplet at 468 nm, 472.15 nm and 480.99 nm due to Zn I 4s5s $^3S_1$ - 4s4p $^3P_{2,1,0}$. There is also a doublet at 491.3 nm and 492.5 nm due to Zn II 3d4f $^2F_{5/2}$ 3d4d $^2D_{5/2,3/2}$. All these lines are significantly broadened beyond the lifetime or Doppler values. Using PrismSPECT the spectrum was fitted with two plasmas. The neutral component, Zn I was fitted with atom/ion density $N_A = 4\times10^{17}$ cm^{-3}, kT_e = 1.1 eV and a plasma thickness of l = 1.7 mm. The ionic component, Zn II was fitted with $N_A = 9.5\times10^{16}$ cm^{-3}, kT_e = 2.4 eV and l = 1.8 mm. Fitting the spectrum at 100 ns (Fig. A.4c) yields for Zn I $N_A = 7\times10^{17}$ cm^{-3}, kT_e = 1.1 eV, and for Zn II $N_A = 6\times10^{17}$ cm^{-3} and kT_e= 2.4 eV. At 50 ns Zn I was fitted with atom/ion density $N_A = 1.2\times10^{18}$ cm^{-3}, kT_e = 1.1 eV and Zn II was fitted with $N_A = 1.2\times10^{18}$ cm^{-3}, kT_e = 2.4 eV. The electron densities for each plasma layer at each time were also calculated and shown on their respective plots in figure A.4.

Table A.1: Main experimentally observed Zn I and Zn II lines

Wavelength (nm) nm	g_1:g_2	A_{21}	E_2(eV)	Transition
328.2	3:1	1.363×10^8	7.7823	Zn I 4s4d: $^3D_1 \rightarrow$ 4s4p: $^3P_0$
330.3	5:3	1.808×10^8	7.7827	Zn I 4s4d: $^3D_2 \rightarrow$ 4s4p: $^3P_1$
334.5	7:5	2.32×10^8	7.7833	Zn I 4s4d: $^3D_3 \rightarrow$ 4s4p: $^3P_2$
468	3:1	1.94×10^7	6.65	Zn I 4s5s: $^3S_1 \rightarrow$ 4s4p: $^3P_0$
472.15	3:3	5.6×10^7	6.65	Zn I 4s5s: $^3S_1 \rightarrow$ 4s4p: $^3P_1$
480.99	3:5	8.9×10^7	6.65	Zn I 4s5s: $^3S_1 \rightarrow$ 4s4p: $^3P_2$
491.3	6:4	1.9×10^8	14.54	Zn II 3d4f: $^2F_{5/2} \rightarrow$ 3d4d: $^2D_{3/2}$
492.5	6:6	1.36×10^7	14.54	Zn II 3d4f: $^2F_{5/2} \rightarrow$ 3d4d: $^2D_{5/2}$

The continuum spectrum emitted during the laser pulse Fig. A.4a was also fitted using PrismSPECT. At this stage there is no indication that the plasma has separated into distinct regions, so it is more appropriate to model it as a single layer. The fit shown was obtained using an atom/ion particle density of $N_A = 3\times10^{19}$ cm^{-3} and kT_e= 2.1 eV and a plasma thickness of 27 μm, which corresponds to density×thickness product of 1.7×10^{17} atom cm^{-2}. The calculated spectrum is also continuous with barely observable line emission. However, the model does show that the continuum emission is predomi-

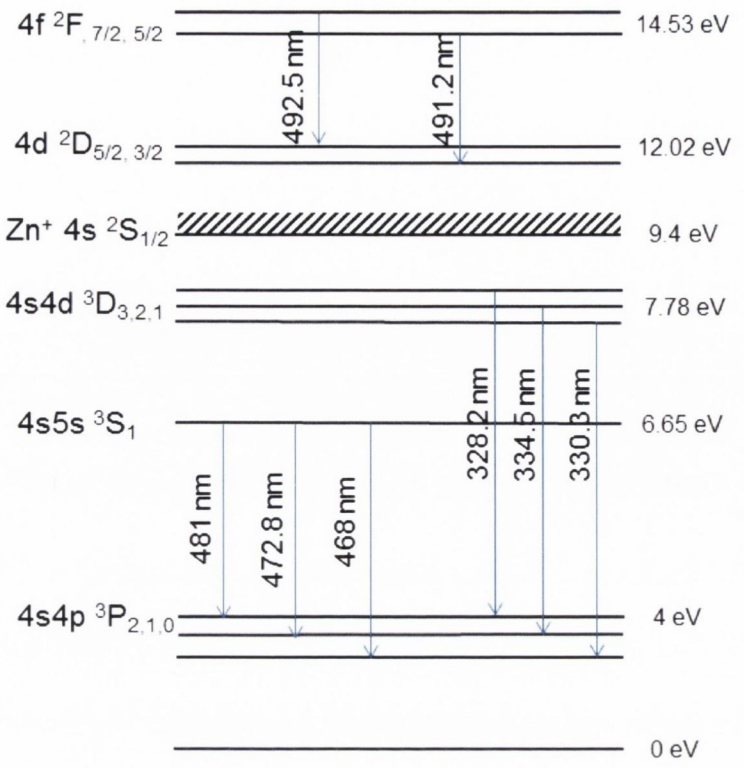

Figure A.5: Simplified energy level diagram for Zn showing the most important radiatively linked levels. The atomic transitions are detailed in table A.1.

nately due to strongly broadened bound-bound transitions in Zn I and Zn II. At this early time the plasma expansion is still 1-dimensional, so the areal density indicated by the absolute intensity of the spectral emission can be compared with the ablation depth. The ablation depth of 22 nm corresponds to a density×thickness product of 1.4×10^{17} atom cm^{-2}, which is in good agreement with the value estimated form the absolute intensity of the emission spectrum during the laser pulse.

PrismSPECT can also be used to calculate the absorption coefficient in a plasma. Figure A.6 shows the absorption coefficient for the plasma conditions found during the laser pulse (0 ns), namely, $N_A = 3\times10^{19}$ cm^{-3} and $kT_e = 2.1$ eV. The code can display how the net absorption is partitioned between the different absorption mechanisms. It can be seen that the absorption is mainly due to bound-bound absorption in Zn I and Zn II. As was observed in emission, these bound-bound transitions are strongly Stark-broadened. Below ≈500 nm free-free and bound-free transitions make only a small contribution to the absorption. Even at the laser wavelength bound-bound transitions account for ~1/3 of the total absorption.

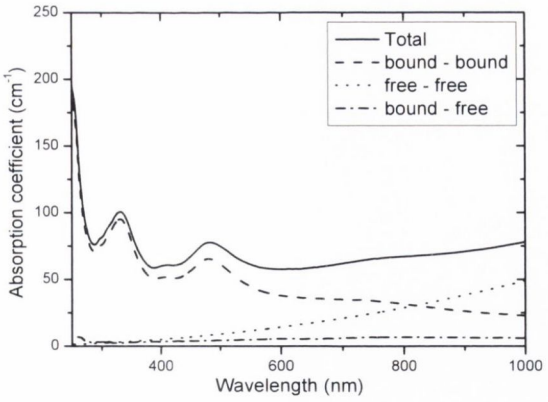

Figure A.6: Calculated optical absorption coefficient in the early stage plasma at $N_A = 3 \times 10^{19}$ cm^{-3} and $kT_e = 2.1$ eV.

A.1.1 Conclusions

Optical emission spectroscopy was used to measure the plasma conditions in the early stages of nanosecond laser ablation of Zn. During the laser pulse, the spectral emission in the visible/UV is a continuum and identifiable line emission emerge after about 50 ns when the plasma expanded to some extent. The collisional-radiative spectral synthesis code PrismSPECT was used to fit the measured spectra and so determine the temporal evolution of the plasma conditions. From this analysis it can be concluded that the continuum emission seen during the laser pulse is mainly due to strongly Stark-broadened bound-bound transitions in Zn I and Zn II. Similarly, it can be concluded that the optical absorption in this early phase of plasma development is due to bound-bound transitions. This observation provides a new insight into the nature of laser absorption in low power pulsed laser ablation of solids.

A.2 Material optical properties

Plotted below are the refractive index and bulk emissivity of each material. The bulk emissivity, $\epsilon_{bulk}(\lambda)$ is calculated by

$$\epsilon_{bulk}(\lambda) = 1 - R(\lambda) = 1 - \frac{(n-1)^2 + k^2}{(n+1)^2 + k^2} \tag{A.1}$$

where $R(\lambda)$, n, k are the material reflectivity, real, and imaginary parts of the refractive index.

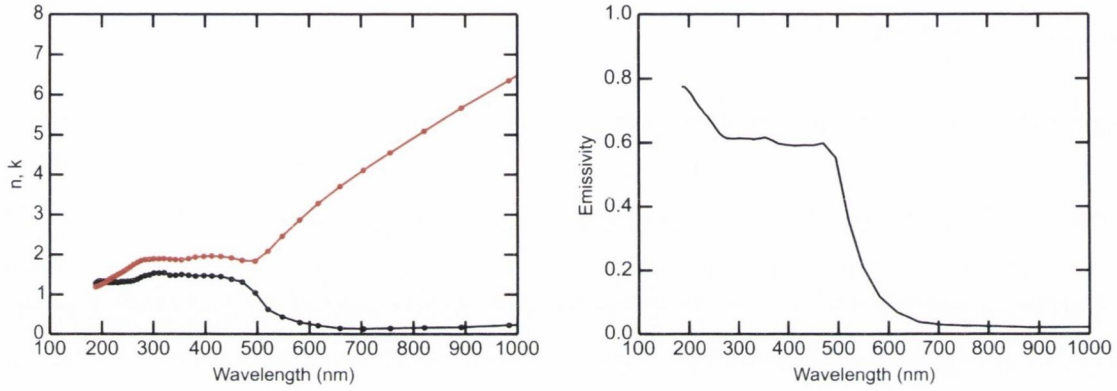

(a) Refractive index **(b)** Emissivity

Figure A.7: (a) The real, n and imaginary, k components of the refractive index of gold and (b) emissivity of gold from a bulk surface.

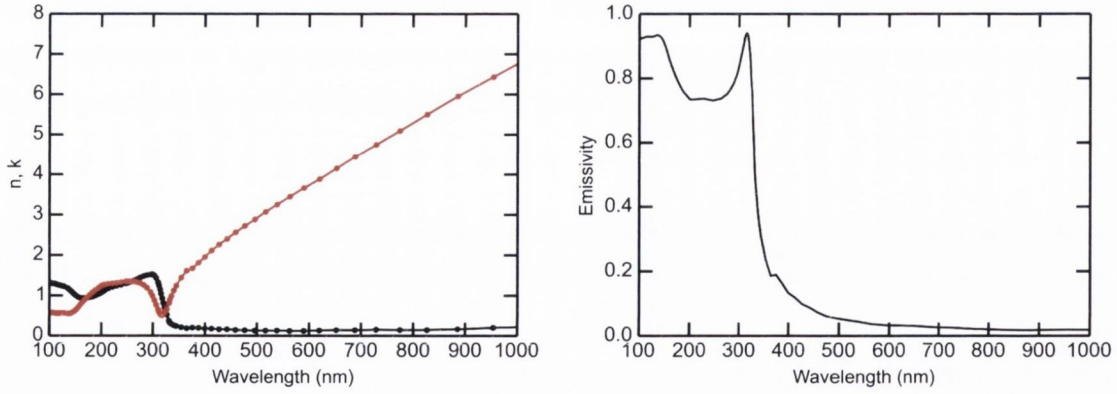

(a) Refractive index **(b)** Emissivity

Figure A.8: (a) The real, n, and imaginary, k, components of the refractive index of silver and (b) emissivity of silver from a bulk surface.

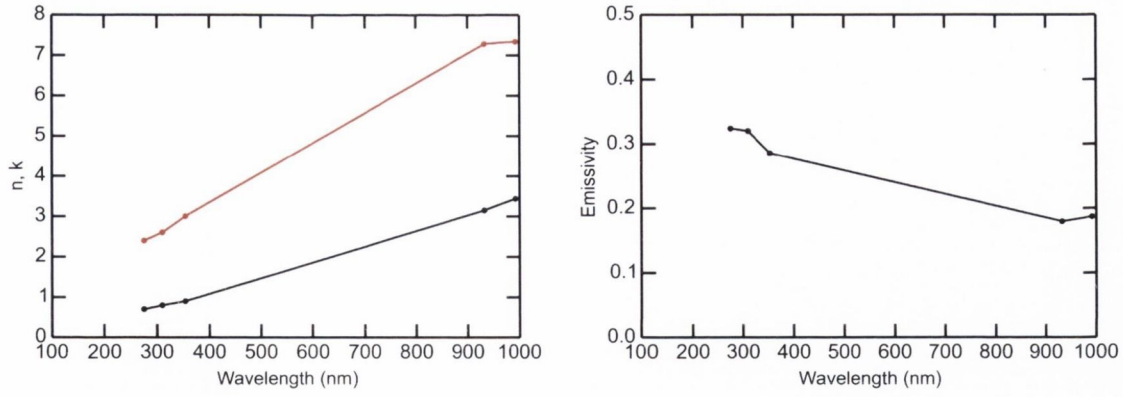

(a) Refractive index **(b)** Emissivity

Figure A.9: (a) The real, n and imaginary, k components of the refractive index of tin and (b) emissivity of tin from a bulk surface.

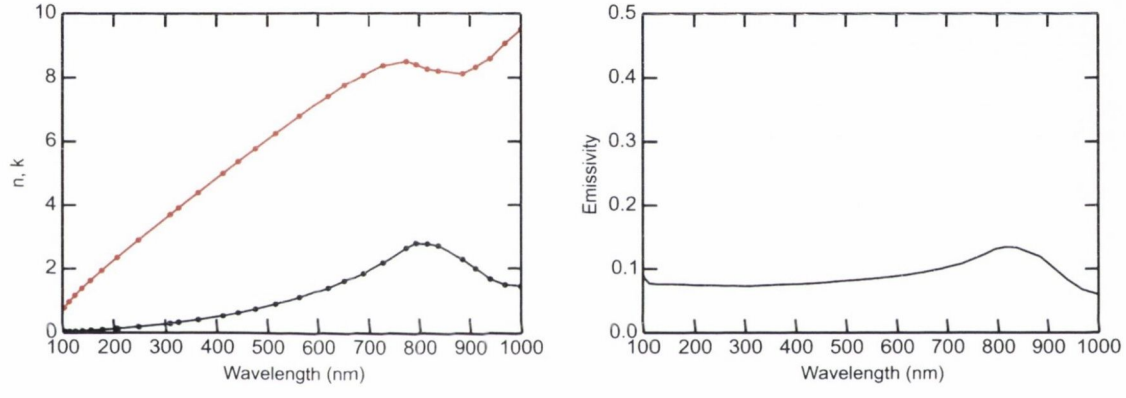

(a) Refractive index **(b)** Emissivity

Figure A.10: (a) The real, n and imaginary, k components of the refractive index of aluminium and (b) emissivity of aluminium from a bulk surface.

A.3 Computational model of atomic plume expansion in femtosecond laser ablation

```
"""import modules"""
import numpy as np
import matplotlib.pyplot as plt
from scipy.integrate import odeint
import scipy.constants as constants


"""input variables"""
m = 28.88 # Molar mass of background gas
M = 1e-11 # Plume total mass (kg)
pg = 300 # Background gas pressure (Pa)
time = np.linspace(0,1.5e-6, 100) #Time step and range (s)
yinit = np.array([0,1.6e4]) #Initial values radius, velocity



def gas_density(m, pg):
    return pg*m/(constants.R*293.15*1000)

rho = gas_density(m, pg)

def deriv(y, t):
    radius = y[0]
    vel = y[1]

    accel =
    -(2*np.pi*pg*radius**2 + 2*rho*np.pi*radius**2 *vel**2)
    / (M + 2./3*rho*np.pi*radius**3)

    radius = radius + vel
    vel = vel + accel
    return [radius, vel]
```

```
y = odeint(deriv,yinit,time)

radius, vel = [], []

for arry in y:
    vel.append(arry[1])
    radius.append(arry[0])
```

Bibliography

[1] T. H. Maiman, "Stimulated Optical Radiation in Ruby," *Nature*, vol. 187, pp. 493–494, Aug. 1960.

[2] F. Breech and L. Cross *Applied Spectroscopy*, vol. 16, p. 59, 1962.

[3] A. De Giacomo, M. Dell'Aglio, O. De Pascale, and M. Capitelli, "From single pulse to double pulse ns-Laser Induced Breakdown Spectroscopy under water: Elemental analysis of aqueous solutions and submerged solid samples," Aug. 2007.

[4] P. G. Etchegoin, E. C. Le Ru, and M. Meyer, "An analytic model for the optical properties of gold," *Journal of Chemical Physics*, vol. 125, p. 164705, Oct. 2006.

[5] A. Pinchuk, G. V. Plessen, and U. Kreibig, "Influence of interband electronic transitions on the optical absorption in metallic nanoparticles," *Journal of Physics D: Applied Physics*, vol. 37, pp. 3133–3139, Nov. 2004.

[6] M. Vitiello, S. Amoruso, C. Altucci, C. de Lisio, and X. Wang, "The emission of atoms and nanoparticles during femtosecond laser ablation of gold," *Applied Surface Science*, vol. 248, pp. 163–166, July 2005.

[7] S. Amoruso, R. Bruzzese, M. Vitiello, N. N. Nedialkov, and P. A. Atanasov, "Experimental and theoretical investigations of femtosecond laser ablation of aluminum in vacuum," *Journal of Applied Physics*, vol. 98, no. 4, p. 044907, 2005.

[8] S. Amoruso, R. Bruzzese, N. Spinelli, R. Velotta, M. Vitiello, X. Wang, G. Ausanio, V. Iannotti, and L. Lanotte, "Generation of silicon nanoparticles via femtosecond laser ablation in vacuum," *Applied Physics Letters*, vol. 84, no. 22, p. 4502, 2004.

[9] P. Balling and J. Schou, "Femtosecond-laser ablation dynamics of dielectrics: basics and applications for thin films.," *Reports on progress in physics. Physical Society (Great Britain)*, vol. 76, p. 036502, Mar. 2013.

[10] C. Smyth, I. Mirza, J. G. Lunney, and E. McCabe, "Surface-enhanced Raman spectroscopy (SERS) using Ag nanoparticle films produced by pulsed laser deposition," *Applied Surface Science*, vol. 264, pp. 31–35, Jan. 2013.

[11] A. I. Kuznetsov, A. B. Evlyukhin, M. R. Gonçalves, C. Reinhardt, A. Koroleva, M. L. Arnedillo, R. Kiyan, O. Marti, and B. N. Chichkov, "Laser fabrication of large-scale nanoparticle arrays for sensing applications.," *ACS nano*, vol. 5, pp. 4843–9, June 2011.

[12] P. Hayden, A. Cummings, N. Murphy, G. O'Sullivan, P. Sheridan, J. White, and P. Dunne, "13.5 nm extreme ultraviolet emission from tin based laser produced plasma sources," *Journal of Applied Physics*, vol. 99, 2006.

[13] D. Perez and L. Lewis, "Ablation of Solids under Femtosecond Laser Pulses," *Physical Review Letters*, vol. 89, p. 255504, Dec. 2002.

[14] D. Perez and L. Lewis, "Molecular-dynamics study of ablation of solids under femtosecond laser pulses," *Physical Review B*, vol. 67, pp. 1–15, May 2003.

[15] M. Povarnitsyn, T. Itina, M. Sentis, K. Khishchenko, and P. Levashov, "Material decomposition mechanisms in femtosecond laser interactions with metals," *Physical Review B*, vol. 75, p. 235414, June 2007.

[16] L. Zhigilei, "Dynamics of the plume formation and parameters of the ejected clusters in short-pulse laser ablation," *Applied Physics A: Materials Science & Processing*, vol. 76, pp. 339–350, Mar. 2003.

[17] D. Ivanov and L. Zhigilei, "Combined atomistic-continuum modeling of short-pulse laser melting and disintegration of metal films," *Physical Review B*, vol. 68, p. 064114, Aug. 2003.

[18] S. Amoruso, R. Bruzzese, X. Wang, N. N. Nedialkov, and P. a. Atanasov, "Femtosecond laser ablation of nickel in vacuum," *Journal of Physics D: Applied Physics*, vol. 40, pp. 331–340, Jan. 2007.

[19] K. Oguri, Y. Okano, T. Nishikawa, and H. Nakano, "Dynamics of femtosecond laser ablation studied with time-resolved x-ray absorption fine structure imaging," *Physical Review B*, vol. 79, p. 144106, Apr. 2009.

[20] S. I. Anisimov, D. Bauerle, and B. S. Lukyanchuk, "Gas dynamics and film profiles in pulsed-laser deposition of materials," *Physical Review B*, vol. 48, pp. 12076–12081, Oct. 1993.

[21] S. Anisimov, B. Luk'yanchuk, and A. Luches, "An analytical model for three-dimensional laser plume expansion into vacuum in hydrodynamic regime," *Applied Surface Science*, vol. 96-98, pp. 24–32, Apr. 1996.

[22] J. Demsar, R. D. Averitt, K. H. Ahn, M. J. Graf, S. a. Trugman, V. V. Kabanov, J. L. Sarrao, and a. J. Taylor, "Quasiparticle Relaxation Dynamics in Heavy Fermion Compounds," *Physical Review Letters*, vol. 91, p. 027401, July 2003.

[23] R. Groeneveld, R. Sprik, and A. Lagendijk, "Femtosecond spectroscopy of electron-electron and electron-phonon energy relaxation in Ag and Au.," *Physical Review B*, vol. 51, pp. 11433–11445, May 1995.

[24] S. Nolte, C. Momma, H. Jacobs, A. Tünnermann, B. N. Chichkov, B. Wellegehausen, and H. Welling, "Ablation of metals by ultrashort laser pulses," 1997.

[25] B. N. Chichkov, C. Momma, S. Nolte, F. von Alvensleben, and A. Tünnermann, "Femtosecond, picosecond and nanosecond laser ablation of solids," Aug. 1996.

[26] K. Furusawa, K. Takahashi, H. Kumagai, K. Midorikawa, and M. Obara, "Ablation characteristics of Au, Ag, and Cu metals using a femtosecond Ti:sapphire laser," *Applied Physics A: Materials Science & Processing*, vol. 69, pp. S359–S366, Dec. 1999.

[27] C. Wu and L. V. Zhigilei, "Microscopic mechanisms of laser spallation and ablation of metal targets from large-scale molecular dynamics simulations," *Applied Physics A: Materials Science & Processing*, vol. 114, pp. 11–32, Dec. 2013.

[28] D. Marla, U. V. Bhandarkar, and S. S. Joshi, "Critical assessment of the issues in the modeling of ablation and plasma expansion processes in the pulsed laser deposition of metals," *Journal of Applied Physics*, vol. 109, no. 2, p. 021101, 2011.

[29] Z. Chen and A. Bogaerts, "Laser ablation of Cu and plume expansion into 1 atm ambient gas," *Journal of Applied Physics*, vol. 97, no. 6, p. 063305, 2005.

[30] F. Rezaei and S. H. Tavassoli, "Numerical and experimental investigation of laser induced plasma spectrum of aluminum in the presence of a noble gas," *Spectrochimica Acta Part B: Atomic Spectroscopy*, vol. 78, pp. 29–36, Dec. 2012.

[31] K. Song and X. Xu, "Mechanisms of absorption in pulsed excimer laser-induced plasma," *Applied Physics A: Materials Science & Processing*, vol. 65, pp. 477–485, Oct. 1997.

[32] V. N. Tokarev and A. F. H. Kaplan, "An analytical modeling of time dependent pulsed laser melting," *Journal of Applied Physics*, vol. 86, no. 5, p. 2836, 1999.

[33] A. V. Bulgakov and N. M. Bulgakova, "Thermal model of pulsed laser ablation under the conditions of formation and heating of a radiation-absorbing plasma," *Quantum Electronics*, vol. 29, no. 5, p. 433, 1999.

[34] V. A. Batanov, F. V. Bunkin, A. M. Prokhorov, and V. B. Fedorov, "Evaporation of Metallic Targets Caused by Intense Optical Radiation," vol. 36, no. 2, pp. 311–322, 1973.

[35] J. G. Lunney and R. Jordan, "Pulsed laser ablation of metals," *Applied Surface Science*, vol. 127-129, pp. 941–946, May 1998.

[36] L. Li, D. Zhang, Z. Li, L. Guan, X. Tan, R. Fang, D. Hu, and G. Liu, "The investigation of optical characteristics of metal target in high power laser ablation," *Physica B: Condensed Matter*, vol. 383, pp. 194–201, Sept. 2006.

[37] R. Fang, D. Zhang, Z. Li, F. Yang, L. Li, X. Tan, and M. Sun, "Improved thermal model and its application in UV high-power pulsed laser ablation of metal target," *Solid State Communications*, vol. 145, pp. 556–560, Mar. 2008.

[38] V. N. Tokarev, J. G. Lunney, W. Marine, and M. Sentis, "Analytical thermal model of ultraviolet laser ablation with single-photon absorption in the plume," *Journal of Applied Physics*, vol. 78, no. 2, p. 1241, 1995.

[39] S. Amoruso, "Modeling of UV pulsed-laser ablation of metallic targets," *Applied Physics A: Materials Science & Processing*, vol. 69, pp. 323–332, Sept. 1999.

[40] R. K. Singh and J. Narayan, "Pulsed-laser evaporation technique for deposition of thin films: Physics and theoretical model," *Physical Review B*, vol. 41, pp. 8843–8859, May 1990.

[41] M. R. Predtechensky, A. P. Mayorov, and M. R. Predteceensky, "Expansion of laser plasma in oxygen at laser deposition of HTSC films:theoretical model," *Applied Superconductivity*, vol. 1, no. 1012, pp. 2011–2017, 1993.

[42] N. Arnold, J. Gruber, and J. Heitz, "Spherical expansion of the vapor plume into ambient gas: an analytical model," *Applied Physics A: Materials Science & Processing*, vol. 93, pp. 87–93, 1999.

[43] S.-B. Wen, X. Mao, R. Greif, and R. E. Russo, "Expansion of the laser ablation vapor plume into a background gas. I. Analysis," *Journal of Applied Physics*, vol. 101, no. 2, p. 023114, 2007.

[44] S. Amoruso, J. Schou, and J. G. Lunney, "Influence of the atomic mass of the background gas on laser ablation plume propagation," *Applied Physics A: Materials Science & Processing*, vol. 92, pp. 907–911, May 2008.

[45] A. Bogaerts, Z. Chen, R. Gijbels, and A. Vertes, "Laser ablation for analytical sampling: what can we learn from modeling?," *Spectrochimica Acta Part B: Atomic Spectroscopy*, vol. 58, pp. 1867–1893, Nov. 2003.

[46] B. Doggett and J. G. Lunney, "Expansion dynamics of laser produced plasma," *Journal of Applied Physics*, vol. 109, no. 9, p. 093304, 2011.

[47] T. Donnelly, J. G. Lunney, S. Amoruso, R. Bruzzese, X. Wang, and X. Ni, "Dynamics of the plumes produced by ultrafast laser ablation of metals," *Journal of Applied Physics*, vol. 108, no. 4, p. 043309, 2010.

[48] T. Donnelly, J. G. Lunney, S. Amoruso, R. Bruzzese, X. Wang, and X. Ni, "Angular distributions of plume components in ultrafast laser ablation of metal targets," *Applied Physics A: Materials Science & Processing*, vol. 100, pp. 569–574, June 2010.

[49] A. Thorne, *Spectrophysics*. Chapman and Hall, 1974.

[50] G. Bekefi, *Principles of laser plasmas*. Wiley, 1976.

[51] "http://nlte.nist.gov/FLY/."

[52] "http://www.prism-cs.com/Software/PrismSpect/PrismSPECT.htm."

[53] G. Mie, "Beiträge zur Optik trüber Medien, speziell kolloidaler Metallösungen," *Annalen der Physik*, vol. 330, no. 3, pp. 377–445, 1908.

[54] W. H. De Jong and P. J. a. Borm, "Drug delivery and nanoparticles: Applications and hazards," Jan. 2008.

[55] W. Shen, X. Zhang, Q. Huang, Q. Xu, and W. Song, "Preparation of solid silver nanoparticles for inkjet printed flexible electronics with high conductivity.," *Nanoscale*, vol. 6, pp. 1622–8, Jan. 2014.

[56] L. L. Vatta, R. D. Sanderson, and K. R. Koch, "Magnetic nanoparticles : Properties and potential applications," *Pure and Applied Chemistry*, vol. 78, no. 9, pp. 1793–1801, 2006.

[57] Y. Oshikane, T. Kataoka, M. Okuda, S. Hara, H. Inoue, and M. Nakano, "Observation of nanostructure by scanning near-field optical microscope with small sphere probe," *Science and Technology of Advanced Materials*, vol. 8, pp. 181–185, Apr. 2007.

[58] S. Amoruso, R. Bruzzese, N. Spinelli, R. Velotta, M. Vitiello, and X. Wang, "Emission of nanoparticles during ultrashort laser irradiation of silicon targets," *Europhysics Letters (EPL)*, vol. 67, pp. 404–410, Aug. 2004.

[59] S. S. Harilal, N. Farid, a. Hassanein, and V. M. Kozhevin, "Dynamics of femtosecond laser produced tungsten nanoparticle plumes," *Journal of Applied Physics*, vol. 114, no. 20, p. 203302, 2013.

[60] C. E. Klots, "Quasiequilibrium rate constants for thermionic emission from small particles," *Chemical Physics Letters*, vol. 186, pp. 73–76, Nov. 1991.

[61] C. Granqvist, L. Kish, and W. Marlow, *Gas Phase Nanoparticle Synthesis*. Springer, 2004.

[62] L. Landström and P. Heszler, "Analysis of blackbody-like radiation from laser-heated gas-phase tungsten nanoparticles.," *The Journal of Physical Chemistry B*, vol. 108, pp. 6216–6221, May 2004.

[63] B. M. Smirnov and H. Weidele, "Radiative emission of hot metallic clusters," *Journal of Experimental and Theoretical Physics Letters*, vol. 69, pp. 490–495, Mar. 1999.

[64] B. M. Smirnov, *Cluster Processes in Gases and Plasmas*. WILEY-VCH Verlag, 2010.

[65] W. Qi and M. Wang, "Size and shape dependent melting temperature of metallic nanoparticles," *Materials Chemistry and Physics*, vol. 88, pp. 280–284, Dec. 2004.

[66] L. Landström, K. Elihn, M. Boman, C. Granqvist, and P. Heszler, "Analysis of thermal radiation from laser-heated nanoparticles formed by laser-induced decomposition of ferrocene," *Applied Physics A: Materials Science & Processing*, vol. 81, pp. 827–833, June 2005.

[67] S. Amoruso, R. Bruzzese, N. Spinelli, and R. Velotta, "Characterization of laser-ablation plasmas," *Journal of Physics B: Atomic, Molecular and Optical Physics*, vol. 32, pp. R131–R172, July 1999.

[68] R. Jordan, D. Cole, and J. Lunney, "Pulsed laser ablation of copper," *Applied surface science*, vol. 86, pp. 24–28, 1995.

[69] B. Doggett and J. G. Lunney, "Langmuir probe characterization of laser ablation plasmas," *Journal of Applied Physics*, vol. 105, no. 3, p. 033306, 2009.

[70] I. Langmuir and H. M. Mott-Smith, "Langmuir probe," *General Electric Review*, vol. 26, p. 731, 1923.

[71] D. W. Koopman, "Langmuir Probe and Microwave Measurements of the Properties of Streaming Plasmas Generated by Focused Laser Pulses," *Physics of Fluids*, vol. 14, no. 8, p. 1707, 1971.

[72] P. L. G. Ventzek, R. M. Gilgenbach, D. M. Heffelfinger, and J. A. Sell, "Laser-beam deflection measurements and modeling of pulsed laser ablation rate and near-surface plume densities in vacuum," *Journal of Applied Physics*, vol. 70, no. 2, p. 587, 1991.

[73] J. A. Sell, D. M. Heffelfinger, P. Ventzek, and R. M. Gilgenbach, "Laser beam deflection as a probe of laser ablation of materials," *Applied Physics Letters*, vol. 55, no. 23, p. 2435, 1989.

[74] S. J. E. Brockington, R. D. Horton, D. Q. Hwang, R. W. Evans, S. J. Howard, and Y. C. F. Thio, "Plasma density gradient measurement using laser deflection," *Review of Scientific Instruments*, vol. 76, no. 6, p. 063503, 2005.

[75] I. Mirza, G. O'Connell, J. J. Wang, and J. G. Lunney, "Comparison of nanosecond and femtosecond pulsed laser deposition of silver nanoparticle films.," *Nanotechnology*, vol. 25, p. 265301, June 2014.

[76] B. Toftmann, B. Doggett, C. Budtz-Jorgensen, J. Schou, J. G. Lunney, and C. Budtz-j, "Femtosecond ultraviolet laser ablation of silver and comparison with nanosecond ablation," *Journal of Applied Physics*, vol. 113, no. 8, p. 083304, 2013.

[77] G. OConnell, I. Tobin, and J. G. Lunney, "Early stage optical emission in nanosecond laser ablation," *Applied Physics A: Materials Science & Processing*, vol. 110, pp. 731–734, Sept. 2012.

[78] J. C. EHRHARDT and S. P. DAVIS, "Precision Wavelengths and Energy Levels in Gold," 1971.

[79] U. Safronova and W. Johnson, "Excitation energies, oscillator strengths, and lifetimes of levels along the gold isoelectronic sequence," *Physical Review A*, vol. 69, p. 052511, May 2004.

[80] T. Donnelly and J. G. Lunney, "Confined laser ablation for single-shot nanoparticle deposition of silver," *Applied Surface Science*, vol. 282, pp. 133–137, Oct. 2013.

[81] S. Djeniže, A. Srećković, and S. Bukvić, "The first measured Ag I, Ag II and Ag III Stark broadening parameters," *Spectrochimica Acta Part B: Atomic Spectroscopy*, vol. 60, pp. 1552–1555, Dec. 2005.

[82] O. Albert, S. Roger, Y. Glinec, J. Loulergue, J. Etchepare, C. Boulmer-Leborgne, J. Perrière, and E. Millon, "Time-resolved spectroscopy measurements of a titanium plasma induced by nanosecond and femtosecond lasers," *Applied Physics A: Materials Science & Processing*, vol. 76, pp. 319–323, Mar. 2003.

[83] A. De Giacomo, M. Dell'Aglio, A. Santagata, and R. Teghil, "Early stage emission spectroscopy study of metallic titanium plasma induced in air by femtosecond- and nanosecond-laser pulses," in *Spectrochimica Acta - Part B Atomic Spectroscopy*, vol. 60, pp. 935–947, 2005.

[84] H. Schittenhelm, G. Callies, P. Berger, and H. Hügel, "Investigations of extinction coefficients during excimer laser ablation and their interpretation in terms of Rayleigh scattering," *Journal of Physics D: Applied Physics*, vol. 29, pp. 1564–1575, June 1996.

[85] H. Search, C. Journals, A. Contact, M. Iopscience, I. P. Address, H. Schittenhelm, G. Callies, A. Straub, P. Berger, and H. Hügel, "Measurements of wavelength-dependent transmission in excimer laser-induced plasma plumes and their interpretation," *Journal of Physics D: Applied Physics*, vol. 31, pp. 418–427, Feb. 1998.

[86] J. Ren, X. Yin, S. S. Orlov, and L. Hesselink, "Realtime study of plume ejection dynamics in silicon laser ablation under 5 ns pulses," *Applied Physics Letters*, vol. 88, no. 6, p. 061111, 2006.

[87] S. H. Jeong, R. Greif, and R. E. Russo, "Shock wave and material vapour plume propagation during excimer laser ablation of aluminium samples," *Journal of Physics D: Applied Physics*, vol. 32, pp. 2578–2585, Oct. 1999.

[88] M. A. Shannon, B. Rubinsky, and R. E. Russo, "Detecting laser-induced phase change at the surface of solids via latent heat of melting with a photothermal deflection technique," *Journal of Applied Physics*, vol. 75, no. 3, p. 1473, 1994.

[89] G. OConnell, T. Donnelly, and J. G. Lunney, "Nanoparticle plume dynamics in femtosecond laser ablation of gold," *Applied Physics A: Materials Science & Processing*, vol. 117, pp. 289–293, Mar. 2014.

[90] E. D. Palik, *Handbook of Optical Constants of Solids*. Elsevier, June 1998.

[91] M. Otter, "Optische Konstanten massiver Metalle," *Zeitschrift fur Physik*, vol. 161, no. 5, pp. 163–178, 1961.

[92] A. D. Rakić, "Algorithm for the determination of intrinsic optical constants of metal films: application to aluminum.," *Applied optics*, vol. 34, pp. 4755–67, Aug. 1995.

[93] A. Bogaerts, Z. Chen, and D. Bleiner, "Laser ablation of copper in different background gases: comparative study by numerical modeling and experiments," *Journal of Analytical Atomic Spectrometry*, vol. 21, no. 4, p. 384, 2006.

[94] S.-B. Wen, X. Mao, R. Greif, and R. E. Russo, "Laser ablation induced vapor plume expansion into a background gas. II. Experimental analysis," *Journal of Applied Physics*, vol. 101, no. 2, p. 023115, 2007.

[95] F. Garrelie, C. Champeaux, and A. Catherinot, "Expansion dynamics of the plasma plume created by laser ablation in a background gas," *Applied Physics A: Materials Science & Processing*, vol. 69, pp. S55–S58, Dec. 1999.

[96] S. Amoruso, R. Bruzzese, X. Wang, and J. Xia, "Propagation of a femtosecond pulsed laser ablation plume into a background atmosphere," *Applied Physics Letters*, vol. 92, no. 4, p. 041503, 2008.

[97] S. Yalcin, Y. Tsui, and R. Fedosejevs, "Images of femtosecond laser plasma plume expansion into background air," *IEEE Transactions on Plasma Science*, vol. 33, pp. 482–483, Apr. 2005.

[98] J. C. Crowhurst, A. F. Goncharov, B. Sadigh, C. L. Evans, P. G. Morrall, J. L. Ferreira, and a. J. Nelson, "Synthesis and characterization of the nitrides of platinum and iridium.," *Science (New York, N.Y.)*, vol. 311, pp. 1275–8, Mar. 2006.

[99] C. Afonso, J. Gonzalo, R. Serna, J. De Sande, C. Ricolleau, C. Grigis, M. Gandais, D. Hole, and P. Townsend, "Vacuum versus gas environment for the synthesis of nanocomposite films by pulsed-laser deposition," *Applied Physics A: Materials Science & Processing*, vol. 69, no. 7, pp. 201–207, 1999.

[100] R. Gaudiuso, M. Dell'Aglio, O. De Pascale, G. S. Senesi, and A. De Giacomo, "Laser induced breakdown spectroscopy for elemental analysis in environmental, cultural heritage and space applications: a review of methods and results.," *Sensors (Basel, Switzerland)*, vol. 10, pp. 7434–68, Jan. 2010.

[101] M. Dong, X. Mao, J. J. Gonzalez, J. Lu, and R. E. Russo, "Time-resolved LIBS of atomic and molecular carbon from coal in air, argon and helium," *Journal of Analytical Atomic Spectrometry*, vol. 27, no. 12, p. 2066, 2012.

[102] J. J. Gonzalez, A. Fernandez, D. Oropeza, X. Mao, and R. E. Russo, "Femtosecond laser ablation: Experimental study of the repetition rate influence on inductively coupled plasma mass spectrometry performance," *Spectrochimica Acta Part B: Atomic Spectroscopy*, vol. 63, pp. 277–286, Feb. 2008.

[103] J. J. Gonzalez, C. Liu, S.-B. Wen, X. Mao, and R. E. Russo, "Metal particles produced by laser ablation for ICP-MS measurements.," *Talanta*, vol. 73, pp. 567–576, Sept. 2007.

[104] B. Fernández, F. Claverie, C. Pécheyran, and O. F. Donard, "Direct analysis of solid samples by fs-LA-ICP-MS," *TrAC Trends in Analytical Chemistry*, vol. 26, pp. 951–966, Nov. 2007.

[105] J. K. Antony, N. J. Vasa, V. L. N. S. Raja, and a. S. Laxmiprasad, "Laser induced breakdown spectroscopy analysis of lunar simulants under high vacuum conditions," *TENCON 2010 - 2010 IEEE Region 10 Conference*, pp. 449–453, Nov. 2010.

[106] "http://www.appliedspectra.com/products/aurora-LIBS-spectrometer.html."

[107] W. Wessel, a. Brueckner-Foit, J. Mildner, L. Englert, L. Haag, a. Horn, M. Wollenhaupt, and T. Baumert, "Use of femtosecond laser-induced breakdown spectroscopy (fs-LIBS) for micro-crack analysis on the surface," *Engineering Fracture Mechanics*, vol. 77, pp. 1874–1883, July 2010.

[108] N. Farid, S. S. Harilal, H. Ding, and a. Hassanein, "Dynamics of ultrafast laser plasma expansion in the presence of an ambient," *Applied Physics Letters*, vol. 103, no. 19, p. 191112, 2013.

[109] R. Krishnan, R. Ramaseshan, T. Mathews, R. Nithya, S. Dash, a. K. Tyagi, and B. Raj, "Synthesis of nanostructured titanium nitride films by PLD through reactive processing," *Surface Engineering*, vol. 25, pp. 218–222, Apr. 2009.

[110] A. Vaseashta and I. N. Mihailescu, *Functionalized Nanoscale Materials, Devices and Systems*. 2008.

[111] M. Sherrill, R. Mancini, J. Bailey, a. Filuk, B. Clark, P. Lake, and J. Abdallah, "Spectroscopic modeling and characterization of a collisionally confined laser-ablated plasma plume," *Physical Review E*, vol. 76, pp. 1–16, Nov. 2007.

Summary

Femtosecond laser ablation of metals and dielectrics is currently very topical due to its new and distinctive ablation process and the growing number of applications. The ablation process is rather complex and results in the formation of two distinct plumes, a fast, atomic component, and a slow component comprised mainly of nanoparticles. This thesis describes the results of an investigation into the femtosecond laser ablation of some metals. The experiments were performed for gold, silver, aluminium and tin to compare the differences in their ablation behaviour.

We studied the atomic plume spectral and spatial emission and found that it is a low temperature plasma with a supersonic velocity. To characterise the nanoparticle plume we performed *in situ*, time-dependent optical emission and absorption measurements. We aimed to extend current analysis methods by taking into account the wavelength dependence of the nanoparticle optical properties. From our results, we inferred the temperature and the amount of material in the nanoparticle plume. We found the nanoparticle plume temperatures varied from about 1700-3000 K depending on material and the time the measurement was taken with respect to the laser pulse. In this range, the nanoparticles were found to cool primarily by evaporation. From our study we noticed significant differences in the plume characteristics of each material. Finally, we studied the behaviour of each plume component in a background gas environment of argon and helium up to atmospheric pressure.

Keywords: Femtosecond laser ablation, optical emission spectroscopy, plume confinement in background gas, Langmuir ion probe, gold, silver, aluminium, tin.